KTH Electrical Engineering

On Design and Analysis of a Novel Transverse Flux Generator for Direct-driven Wind Application

DMITRY SVECHKARENKO

Doctoral Thesis
Stockholm, Sweden 2010

Elektriska Maskiner och Effektelektronik
Skolan för Elektro- och Systemteknik, KTH
Teknikringen 33, SE-100 44 Stockholm
SWEDEN

TRITA-EE 2010:046
ISSN 1653-5146
ISBN 978-91-7415-798-7

Akademisk avhandling som med tillstånd av Kungl Tekniska högskolan framläggs till offentlig granskning för avläggande av teknologie doktorsexamen måndag den 29 november 2010 klockan 10.00 i F3, Lindstedsvägen 26, Kungl Tekniska högskolan, Valhallavägen 79, Stockholm.

Tryck: Universitetsservice US AB

Abstract

This thesis deals with the analysis of a permanent magnet synchronous generator suited for direct-driven wind turbines in megawatt class. The higher specific torque and power density of a transverse flux permanent magnet machine in comparison to conventional radial-flux machines make it a promising solution for direct-driven wind turbine generators. The novel transverse flux generator investigated in this work would allow a better utilization of the available nacelle space due to its more compact construction.

The major part of the thesis deals with the finite element analysis and analytical calculations of transverse flux generators. The computations are performed for single units of the basic transverse flux topology (BTFM) and the one utilizing iron bridges (IBTFM). As the selection of the pole length in a transverse flux machine affects the pole-to-pole flux leakage and thus its performance, the topologies have been analyzed with respect to the varying dimensions in the direction of movement. The topologies utilizing IBTFM have been found to be superior to the BTFM with respect to the flux linkage (by 110%) and utilization of the magnets (by 84%). The machines with longest magnets gave the largest flux linkage, while machines with short magnets should be preferred for better magnet utilization. The four sets of dimensions have been selected for a dynamic finite element analysis.

The power factor is evaluated for the topologies with the varying dimensions in the peripheral plane in static finite element analysis. The performance of the topologies with the best power factor in the studied range (0.62 in the BTFM and 0.57 in the IBTFM), as well as the topologies that give the highest power factor to magnet volume ratio, is compared with the dynamic simulations.

The electromagnetic and cogging forces of the transverse-flux generator are estimated. The IBTFM is superior to the BTFM with respect to the force production, where the three-phase electromagnetic force is twice as large as in the BTFM. The force ripples of the three-phase electromagnetic force are found to be insignificant in both topologies.

An analytical procedure based on the results from the finite element simulations is applied for evaluation of the transverse flux generators with different shapes and topologies. The effectiveness of each topology is investigated based on the estimation of the torque production in a certain nacelle volume. A toroidal generator with the iron-bridge topology is the most compact alternative for a wind turbine as it has the highest torque-per-volume ratio.

Furthermore, the analytical model, including evaluation of the synchronous inductance, is developed and compared with the results obtained in the three-dimensional finite element analysis. The model provides a good agreement for the studied set of dimensions.

Keywords: Transverse flux machines, permanent magnet machines, finite element analysis, direct-driven generator, offshore wind turbine, renewable energy.

Acknowledgments

This doctoral thesis concludes the work that I have carried out at the Department of Electrical Machines and Power Electronics, Royal Institute of Technology.

I owe my sincere gratitude and appreciation to my supervisor Professor Chandur Sadarangani for his continuous support and encouragement, and for reading the various drafts of this thesis. I also would like to express my warmest gratitude to my other supervisor Associate Professor Juliette Soulard for her guidance, enthusiasm and for making valuable suggestions.

Financial support of the project from the Vindforsk Research Program and the Swedish Center of Excellence in Electric Power Engineering EKC2 is gratefully acknowledged.

I am deeply indebted to my colleague Alija Cosic for providing much needed data and for all the stimulating discussions on topics of transverse flux machines.

My special thanks to Nathaniel Taylor for helping me in all possible ways, proofreading this thesis and many exciting discussions. In this regard, I would also like to thank Valery Knyazkin for his friendship and always open attitude.

Many thanks to my colleagues at the department without whom my work would have been more difficult and not as exciting. Special thanks to Mats Leksell for all the encouraging discussions on various topics, Hans-Peter Nee for reviewing this thesis and for the opportunity to enjoy the Renaissance concerts, Henrik Grop for sharing the office and humbly answering my questions related to the complexities of the Swedish language, Alexander Stening for his always positive attitude and willingness to help, Tomas Modeer for being my roommate in different times and for all the concerts we have attended, Kashif Khan for all the friendly conversations we had, and to Rathna Chitroju for just being himself. Eva Pettersson is deeply acknowledged for her kindness and great help with financial issues. Peter Lönn is thanked for his help regarding computer questions.

I would like to extend my gratitude to all my former colleagues at the department and particularly Peter Thelin, Freddy Magnussen, Hailian Xie, Robert Chin, Florence Meier and Waqas M. Arshad.

I am most grateful to all my friends here in Sweden and elsewhere for making my life complete and supporting me in different ways throughout my studies. My dear friends Emma and Celie Geira will always be remembered for their great friendship and all the exciting moments we have shared. François Besnard is deeply acknowledged for all our illuminating conversations about the meaning of life. Valentinas Dubickas and Aurelija Dubicke, Aliaksandr Bulhak and Narine Mkrtchyan for the friendship and our various trips and activities. Many thanks to Valeriu Savcenco, Eugen Moldovan and Carolina Ciumas for all the exciting discussions during our cozy gatherings. Sharon Lim and Jens Boldt are thanked for all the great memories we share. My sincere appreciations to Maria Åkesson and Anne Klemsdal for the lovely dinners and their continuous support.

Last, but not least, I would like to express my deepest and most sincere gratitude to my beloved parents and my brother Oleg whose endless love and everlasting support made all this possible.

Dmitry Svechkarenko

Stockholm, Sweden
October, 2010

Contents

Chapter 1

Introduction

Design of any electromechanical energy converter, often referred to as simply an electrical machine, is a complex and time-consuming task that requires an extensive knowledge of different scientific disciplines. Electromagnetism, thermodynamics, mechanics and acoustics are only some examples of the fields that are brought together inside an electrical machine. The complexity of analysis is increased even further, as the physical processes taking place inside the machines are interrelated. Thus, the assumptions considered in the electromagnetic design would inevitably affect the outcome of, for example, the thermal computations.

A good example of these multidisciplinary correlations would be a selection of the airgap diameter D of an electrical machine. The torque produced in the rotating machines is proportional to the square of the airgap diameter, which makes machines with the larger D favorable. However, if a compact machine with a small outer diameter and a high power density is to be designed, the cooling surface of the machine would get smaller while the loss density, on the other hand, will increase. To account for the increased heat flow and therefore prevent the machine from a possible overheating, the cooling system must be designed carefully. In other words, the temperature and the pressure drop, or even the type of the coolant used to extract the heat, could be affected by constraints adopted in the electromagnetic design. Therefore, the design of an electrical machine should be done very cautiously and with realistic assumptions.

In addition, as in any commercial product, the economic analysis of electrical machines is of a great importance. Not only does the cost of the active materials, e.g. iron, steel, magnets, insulation, contribute to the final price of an electrical machine, but also the complexity of the manufacturing processes and installation, price of the supporting structure and the control unit, as well as the number of pieces produced and delivered. This analysis is mainly related to the field of the

industrial economics and therefore is out of the scope of the work described in this thesis. Instead, the emphasis is placed on the electromagnetic design and analysis of an electrical machine with the thermal and mechanical limitations included as constraints in the calculations.

The physical and mathematical description of the processes involved in the energy conversion in conventional electrical machines can be found in a great variety of literature dealing with this broad area. The analysis becomes somewhat more complicated if the design concerns an electrical machine whose structure or components can be described as unconventional or novel. In this case, the information is generally quite limited, if available at all, resulting in extra time and effort to be spent on the problem description and its consequent solution.

At this point, one can ask a legitimate question: Why do we actually need to design something new and unusual, if we have an existing technology whose benefits are widely recognized and reliability is proved throughout the years? Well, the forces behind this development of novel electrical machines are the same as for any other development: we would like to improve existing products and create new ones that are cheaper, serve longer, have lower environmental impact and are more beneficial to society.

1.1 Objectives

An attempt to develop such *a new product* is made in this doctoral thesis, which deals with the design and analysis of a novel direct-driven permanent magnet transverse flux synchronous generator in the multi-megawatt class suited for the offshore wind turbine applications. In this work, we will try to understand the driving forces behind the development of wind energy worldwide; we will give the reasons to the increased interest in the gearless wind energy systems among wind turbine manufacturers and researchers; we will argue about different configurations employed by the wind generators and discuss the pros and cons of the transverse-flux configuration adopted in the generator that is the focus of this work.

The major part of the thesis deals with the finite element analysis and analytical calculations of transverse flux generators. The computations are performed for single units of the basic transverse flux topology (BTFM) and the one utilizing iron bridges (IBTFM). The results of the finite element analysis are thereafter adopted for the entire generator. The performance is analyzed with respect to varying output powers.

1.2 Main Contributions of the Thesis

In this thesis, it is shown that the generators with the transverse flux topology utilizing iron bridges and toroidal shape are superior to the other studied options. The generators of that type offer a reduced outer diameter for a given output power and thus have a larger torque-per-volume ratio. The reduced outer diameter contributes to a smaller inactive portion of the total weight.

Three-dimensional static and dynamic finite element simulations of the generators with the various transverse flux topologies are performed. The influence of dimensions of the magnetic circuit on the pole-to-pole flux leakage, flux linkage, force production and power factor is studied. This analysis can help the designers of transverse flux machines to select the appropriate set of dimensions when opting for the desired performance.

The power factor of the studied generators is estimated with the help of static and dynamic finite element method (FEM) calculations and analytical expressions. The developed methods show good agreement between each other and thus could be used depending on the availability of data or when selecting the shortest calculation time.

A semi-analytical approach to estimate the electromagnetic force in the transverse flux machines is proposed and compared with the dynamic 3D FEM simulations. This method shows a good agreement with the FEM analysis and thus can be used to reduce calculation time, as the need for the rather time consuming dynamic FEM simulations is eliminated.

The analytical models for the BTFM and IBTFM at no load and with the armature current are developed. The models can be used to estimate the dimensions of the magnetic circuit or be applied in an optimization procedure.

1.3 Thesis Outline

The thesis is organized in the following order:

Chapter 2 discusses the environmental, economic and political driving forces of renewable energy sources. Particular emphasis is placed on wind power. The use of renewables is analyzed with respect to the existing energy technologies.

Chapter 3 introduces the principles of energy conversion in a wind energy system. It gives an overview of the most common wind energy systems and their electrical and mechanical components. Various types of generators available commercially and those reported in literature are described.

Chapter 4 provides a general overview of various permanent magnet synchronous machines. The emphasis is placed on the transverse flux topology and

its principles of operation. Various configurations of transverse flux topologies are reviewed and their properties are outlined.

Chapter 5 deals with three-dimensional static and dynamic finite element analyses of a transverse flux permanent magnet generator at no-load condition. The dimensions of the magnetic circuit are analytically computed and then inserted into a FEM-software. The generators employing two transverse flux topologies: the basic topology and the one utilizing an iron bridge are evaluated.

Chapter 6 comprises calculations of the power factor and the electromagnetic force of a transverse flux generator with the use of three-dimensional finite element analysis. The power factor is calculated by three different methods and the results are compared. The alternative way to estimate the electromagnetic force based on the static simulations is described.

Chapter 7 applies the results of the studies conducted in the two previous chapters to estimate the outer dimensions and performance of transverse flux generators with toroidal and cylindrical shapes. The generators are analyzed with respect to the electromagnetic torque production in a given nacelle volume. Variation of the outer diameter and some other key values are investigated for the various output powers.

Chapter 8 presents an improved analytical model that could be used to analyze generator performance. The results of this study are compared with the results of the finite element calculations from the previous chapters.

Chapter 9 concludes this thesis by summarizing the presented work. Some guidelines for future work are outlined.

1.4 List of Publications

Some parts of this thesis have previously been published in the following papers:

1. **D. Svechkarenko**. *On Analytical Modeling and Design of a Novel Transverse Flux Generator for Offshore Wind Turbines*, Licentiate thesis, Royal Institute of Technology, Stockholm, Sweden, June 2007.

2. **D. Svechkarenko**, J. Soulard, C. Sadarangani, Performance Evaluation of a Novel Transverse Flux Generator with 3D Finite Element Analysis, *International Conference on Electrical Machines and Systems*, Tokyo, Japan, 15-18 November, 2009.

3. **D. Svechkarenko**, J. Soulard, C. Sadarangani, Parametric Study of a Transverse Flux Wind Generator at No-load using Three-dimensional Finite Element Analysis, *International Conference on Electrical Machines and Systems*, Tokyo, Japan, 15-18 November, 2009.

4. **D. Svechkarenko**, A. Cosic, J. Soulard, C. Sadarangani, Transverse Flux Machines for Sustainable Development – Road Transportation and Power Generation, *7th International Conference on Power Electronics and Drive Systems*, Bangkok, Thailand, 27-30 November, 2007.

5. **D. Svechkarenko**, J. Soulard, C. Sadarangani, Analysis of a Novel Transverse Flux Generator in Direct-driven Wind Turbines, *International Conference on Electrical Machines*, Chania, Greece, 2-5 September, 2006.

6. A. Cosic, C. Sadarangani, **D. Svechkarenko**, A Prototype Design of Novel Transverse Flux Machine for the Free Piston Energy Converter, *5th Nordic Workshop on Power and Industrial Electronics*, Lund, Sweden, 12-14 June, 2006.

7. **D. Svechkarenko**, J. Soulard, C. Sadarangani, A Novel Transverse Flux Generator in Direct-driven Wind Turbines, *5th Nordic Workshop on Power and Industrial Electronics*, Lund, Sweden, 12-14 June, 2006.

Chapter 2

Prerequisites for the Development of Renewable Energy

The share of wind power in the world electricity mix has been continuously growing during the last decades. Apart from the technological advances, there are number of other factors that contribute to this progress. The environmental concerns about the wide use of fossil fuels and nuclear power, as well as the unsolved issues of energy security has led to the increased public awareness. As a result, a number of political decisions have been made that have promoted development of renewable energy sources through different mechanisms, thus making a rather costly and still developing technology more economically feasible. The environmental, economic and political driving forces of the renewable energy sources are discussed in this chapter, with an emphasis on wind power. The use of renewables is analyzed with respect to the existing technologies.

2.1 Overview of Wind Power Worldwide

Although wind energy has been used for thousands of years for crushing grain and pumping water, its application as a means of electricity generation is rather new and still developing. Wind turbine technology has undergone a quite spectacular development during the past decades. The increase in size and output power of a typical wind turbine over the last 20 years is depicted in Fig. 2.1 [1]. A typical size of a recently installed turbine is 3–5 MW. Some wind turbines exceeding 5 MW are being tested nowadays and should reasonably be expected on the market in the foreseeable future. At the same time, the cost of electricity produced by wind has dropped considerably since wind power re-emerged in the 1980s.

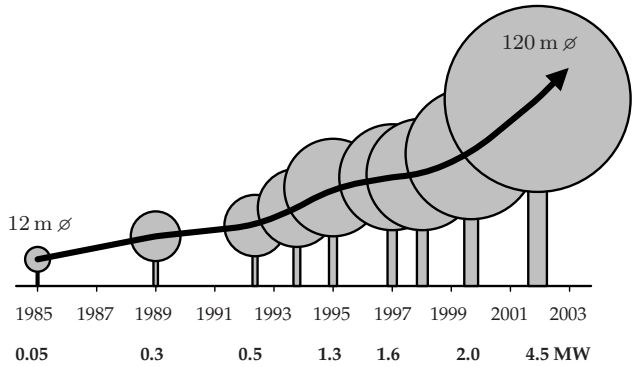

Figure 2.1: Growth of wind turbine size during the last 20 years [1].

In spite of the relatively low recent price of fossil fuels, wind is one of the most economically feasible methods of electricity generation available.

Wind power is one of the fastest growing renewable energy sources over the past two decades with an approximate increase of 30% per annum. Fig. 2.2 shows the total wind capacity installed worldwide between 2001 and 2009 with the last bar representing the predicted value for 2010 [2]. This growth accounts for both the amount and the size of new turbines installed. As 38.3 GW was added in 2009, the total worldwide wind capacity has reached 159.2 GW. As much as 340 TWh of

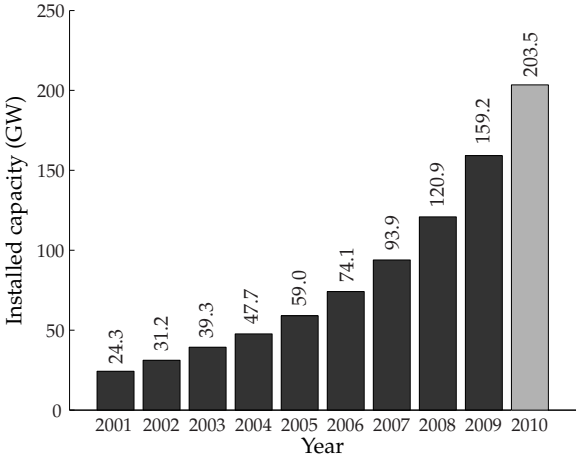

Figure 2.2: World total installed wind-power capacity (in GW) [2].

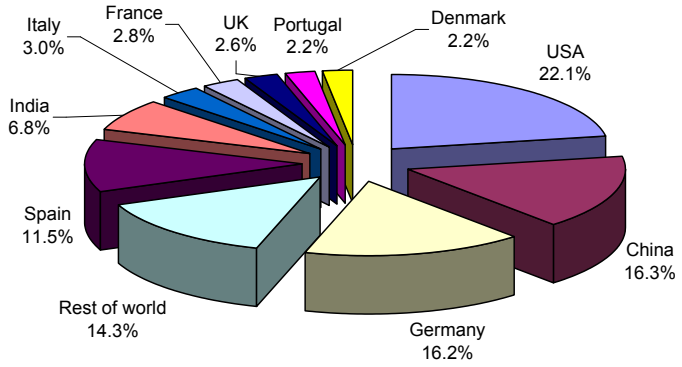

Figure 2.3: Country share of installed wind power capacity for year 2009 [2].

the world electricity mix has been generated by the wind turbines worldwide in 2009.

The United States is the world's leading country with 35.2 GW or 22.1% of wind power capacity installed, see Fig. 2.3; during the last two years, it has doubled its capacity and taken the first place from the former leader Germany.

Recent advances in China and India have allowed these countries to hit top five in the ranking list with the second and the fifth places respectively. China has continued its impressive development and by the end of the year 2009 its total capacity exceeded that of Germany.

Germany is the leading country in Europe, where 25.8 GW or 16.2% of wind power capacity is installed. Three of the world's largest wind turbines (Enercon 4.5MW, Multibrid 5MW, and REpower 5MW) are also located in Germany. About 9% of the country's electricity supply comes from wind.

There are number of driving forces that have ensured this spectacular development of renewable sources in general and wind power in particular. Besides the advances in technology, the main contributors are the environmental and security concerns, as well as the economic stimulation.

2.2 Environmental Concern

According to the estimate reported by the Intergovernmental Panel on Climate Change (IPCC), the global average temperature rose by approximately $0.6 \pm 0.2°\mathrm{C}$ (with 95% confidence interval) in the 20th century. The increased public concern resulted in a large number of studies conducted to investigate the possible impact of global warming on mankind and the environment in general and to propose various options for adaptation and mitigation.

Following the scientific consensus on global warming summarized by IPCC, it was generally agreed that the observed warming is likely to have been caused by the increased concentration of so-called greenhouse gases in the Earth's atmosphere. A large amount of gas is discharged in the atmosphere as a result of human activity by burning of traditional fossil fuels, such as coal, oil, and natural gas.

As a result of increased public awareness, the Kyoto protocol was signed by the overwhelming majority of the world's nations (over 160 countries). The amount of emission produced by each signatory is specified. According to the protocol, the industrialized countries are supposed to reduce their collective emission of greenhouse gases by an average of 5% as compared to 1990. For example, the European Union countries aim for 20% reduction of carbon dioxide and five other greenhouse gases by year 2020 [3]. Russia, China, and India are able to retain their current discharge level. Some countries were actually permitted to increase their emissions, such as Iceland by 10%.

The largest share of anthropogenic greenhouse gases is emitted into atmosphere due to power generation, some industry processes, and road transportation. The main producers of CO_2 within the electric power generation sector are the power plants whose operation is based on burning of fossil energy carriers. Coal is the most widely used energy source of electricity generation, supplying about 41% of the world's annual electricity output. At the moment, the coal-burning power plants are one of the largest sources of man-made carbon dioxide emissions. Although economically feasible, they are the least efficient in terms of CO_2 discharge per unit of electricity generated.

Replacement of fuel-burning power plants with the environmentally friendly alternatives implies that each kilowatt-hour that is produced by renewables will replace one kilowatt-hour produced otherwise. Generally speaking, the renewable sources, among which wind power starts to play an increasingly important role, can potentially replace fossil fuel-burning power plants. There are two possible ways of this replacement: direct and indirect [4]. A direct approach is when the generation of electricity in the fossil fuel-burning power plant is reduced as a result of the increased generation by renewables. In case of wind power, the generation can be increased during the windy hours, while coal-burning power plants are operated when it is not the case. An indirect approach is to operate wind turbines while storing water in the water reservoirs of hydro power plants. The stored water can then be used to generate electricity by hydro instead of burning fossil fuels.

Another way to decrease concentration of the anthropogenic greenhouse gases in the atmosphere is to expand the share of nuclear power, as this discharges no CO_2 during electricity generation. This scenario is, however, less desirable, partly due to the problem of storage of the radioactive waste.

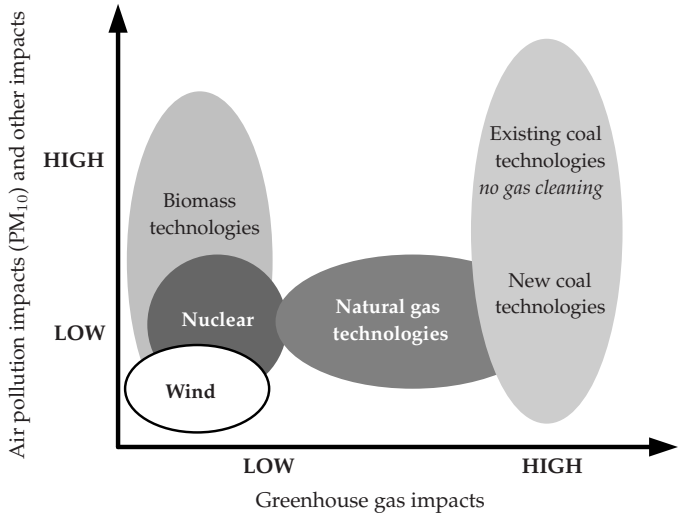

Figure 2.4: Air pollution and greenhouse gas impacts of different technologies [6].

Construction of new hydro power plants can arguably contribute to greenhouse gas mitigation. As recent studies suggest, the water reservoirs significantly contribute to greenhouse gas emission, primarily due to CO_2 and CH_4 from decaying flora [5]. The construction of dams and creation of water reservoirs has also the cumulative impact on the world's rivers causing a severely increased age of river runoff and decreased temperature of downstream flows [5].

In recent years, various studies have made an attempt to determine the damage cost of electricity generated by different power plants, e.g. [6, 7]. It was found, that impact varies considerably depending on fuel choice, technology and location. In [7], this comparison has been made for coal, gas, nuclear and wind electricity. The summary of this study is depicted in Fig. 2.4. As study showed, wind energy is the most environmentally friendly alternative compared to the others. It is favorable from both air pollution and greenhouse gases mitigation points of view.

Apart from the air pollution and the effect on the global warming, there are number of other environmental issues that should be taken into account while making a comparison between impacts of different energy sources for electricity generation. Noise and visual intrusion are one of the most disputable issues among opponents and proponents of wind energy. Both impacts can however be considerably reduced through a thorough planning of the installation sites and consultations with the local authorities. The offshore wind farms, in this regard, can be considered as more advantageous alternatives. Although a few studies

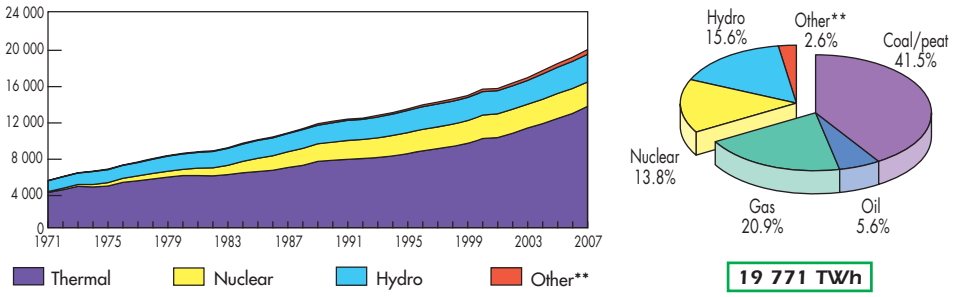

(a) Evolution of electricity generation

(b) Fuel shares

Figure 2.5: (a) Evolution from 1971 to 2007 of electricity generation by fuel (TWh) and (b) fuel shares of electricity generation as for 2007 [8]. *Excluding pump storage, **Other includes geothermal, solar, wind, combustible renewables and waste, and heat.

suggest the opposite, the impact of wind turbines on wildlife is generally considered to be negligible when quantified and thus is not an obstacle to the further development of the wind energy.

2.3 Security of Energy Supply

Another important driving force for the development of the renewables is the issue of energy security. Taking the year 2007 as an example, fossil fuels supplied as much as two thirds of the world's electricity output, see Fig. 2.5; of which coal supplies 41.5%, natural gas 20.9% and oil 5.6% [8].

Crude oil has the smallest share among fossil energy carriers and thus its impact on the security of energy supply is rather limited. About one quarter of the annual oil-fired electricity is produced in the oil-rich Middle East.

On the other hand, coal has the largest share, which has been continuously increasing, mainly due to the low price of extraction and the availability from the politically stable regions. Even though coal is a fossil fuel, its reserves are expected to last much longer than those of oil or natural gas.

Although having a low investment cost, gas turbines run on expensive fuel with an unpredictable cost. The further expansion of gas in electricity generation might threaten energy security of a country dependent on imported gas.

Among non-fossil energy sources, nuclear and hydro contribute to about 13.8% and 15.6% of the world's total electricity mix respectively. The further development of nuclear power is still questionable mainly due to a lack of public support.

The main concerns are storage of the radioactive waste as well as nuclear proliferation and terrorism. The further increase of hydroelectricity has also some negative aspects, such as a potential threat to a continuous water supply in different places in the world, and a mass resettlement of people caused by construction of large dams.

On the other hand, the increased share of renewable energy in electricity generation could offer an improved security of supply, mainly due to the decreased dependency on imported fuel, as electricity can be generated by, for example, wind turbines installed locally. In some places, geographically concentrated power plants and other infrastructures can jeopardize energy security as a result of natural disasters. The distributed nature of many renewable sources can thus offer a reduced risk of grid failures.

Reliance on a solitary source of electricity generation could become a threat to the national energy security. As for example hydro generation is very much dependent on weather conditions of a particular year; nuclear and thermal power plants can be shut down due to unexpected faults or shortages in fuel supply; wind power is dependent on wind conditions and solar panels on the sun, and so on. Therefore, diversity in electricity generation becomes an important issue when energy security of a country is concerned.

To promote the further development of renewables in the European Union, the directive 2001/77/EC [8] has been established. It aims at generating as much as 20% of EU energy by means of renewable energy sources by 2020, among which wind energy is expected to play an increasingly important role. As it stated in the directive [3]

> *The promotion of electricity produced from renewable energy sources is a high Community priority... for reasons of security and diversification of energy supply, of environmental protection and of social and economic cohesion.*

2.4 Economic Support

Following the increased public awareness about the wide use of diminishing fossil fuels and nuclear power and their impact on the environment, a number of political decisions on promotion of the renewable alternatives have been made. One of the main driving forces of the development of wind power nowadays is the economic support provided by the local governments, authorities and organizations. A number of different support systems exist in various countries [9]. Some of them are outlined below.

- *Feed-in tariffs.* These systems specify the certain power purchase price that must be paid by the local distribution or transmission companies to local

producers of renewable electricity. The main advantage of the feed-in tariffs is that they offer a reduced investment risk since the purchase price is usually set for a period of around seven years, thus contributing to promotion of the mid and long-term renewable technologies.

- *Green certificates* is a market-based system which obliges consumers of electricity to purchase a specified amount of electricity produced by renewable sources. A typical value of one green certificate is 1 MWh. In Sweden, the green certificates specify not an amount but a proportion of a total consumption of electricity that should come from renewable energy sources. In both cases, a producer of renewable electricity receives an additional bonus from the sold certificates.

- *Tenders.* The tendering procedure is initiated by the state, which places a series of tenders for supply of renewable electricity on a contract basis at the price resulting from tenders. The final consumers of electricity are then obliged to cover the increased price of electricity through a specific levy.

- *Tax incentives* are introduced by the governments to make investments in renewable energy sources more attractive. The tax incentives can be in the form of reductions of energy taxes or in the form of special grants.

- *A quota system* is based on setting a certain amount (quota) of installed capacity from renewable electricity that should be generated in the country within a year.

Different policies and measures at present adopted in Europe have mainly been aimed at promotion of renewable energy sources in the total electricity mix. As no specific instrument has been recommended or harmonized within the EU, each country has implemented its own instruments of economic support depending on the national goals that include environmental commitments, increased security supply, establishment of new jobs, etc.

The feed-in tariffs system is the most popular support approach used among the European countries. It has been successfully implemented in Germany, Spain and Denmark, where the proportion of installed capacity is the largest in Europe.

Quota systems combined with green certificates is the second most popular measure of support for renewable technologies, which among others countries has been implemented in Sweden. In spite of the additional investment incentives and environmental bonuses available for wind energy, the technology is still undergoing a development stage. The improvements could however be expected in the near future, as the new target to increase the capacity of the installed wind power up to 30 TWh by 2020 has been recently set in the country [10].

Other support systems seem to be less popular among the European countries, as, for example, the tender system is employed only in France, a quota based systems without certificate systems is used in Latvia, while Malta and Finland rely only on the tax incentives.

The further development of renewable energy sources can be achieved by overcoming the administrative and social barriers that make the process for permission to construct new renewable power plants too time consuming. This can be achieved through creation of 'one-stop authorization agencies' where the decision on commissioning of a new power plant can be made in one place.

2.5 Conclusions

Different driving forces that in the past few decades have contributed to the rapid development of renewable energy sources in general and wind power in particular have been addressed in this chapter. It was found that the share of renewables in the world electricity mix has mainly been increased due to the three following factors: environmental concern and issues of energy security, which prompted the governments in different countries to make decisions on economic support.

As far as the environment is concerned, renewable energy sources are preferable to the existing technologies. Fuel-burning power plants are least efficient in terms of CO_2 discharge per unit of electricity generated. Large hydro power plants also contribute to the CO_2 and CH_4 emission as a result of the decaying vegetation. Although nuclear power has the lowest emission level of greenhouse gases into the atmosphere, its further expansion is less desirable mainly due to the problem of storage of radioactive waste.

Renewable energy sources can also increase the security of energy supply, mainly due to decreased dependency on the imported fuel supply. Although coal is available from politically stable regions and the use of oil in electric power generation is limited, the use of natural gas might threaten the energy security of a country dependent on this fuel. Nuclear power has a dual effect on energy security: on the one hand, installation of new nuclear power plants can increase it; on the other hand it can be hazardous, mostly due to the issues of nuclear proliferation and terrorism. The distributed nature of renewable energy sources can offer a reduced risk of grid failures.

Economical support of renewable energy sources is one of the main driving forces to their recent developments. Different measures and policies have mainly been aimed at promotion of the renewable energy sources in the total electricity mix. The implementation of a support scheme is dependent on the national goals that included environmental and social targets and establishment of new jobs. The challenges are, however, in overcoming the administrative and social barriers, as

well as in the further development of technologies and their integration in the electric power systems. The recent advances and the development of wind turbine technology are presented in the following chapter.

Chapter 3

Wind Power Technology

This chapter introduces the principles of energy conversion in a wind energy system. The characteristics of wind turbines are distinguished. Namely, the onshore, near-shore and offshore siting of wind turbines is discussed. An overview of the most common wind energy systems and their electrical and mechanical components is presented. Various types of the commercially available generators and the generators reported in literature are described.

3.1 Introduction to Wind Power

Wind turbines with high rated power are primarily intended for the regions with high wind speeds, as the power of wind P_{wind} is proportional to the interception area of the turbine blades A_{turb} and the cube of wind velocity v_{wind}. The power in airflows can be extracted through conversion by the blades of a wind turbine into mechanical power at the shaft. The power of wind of the speed v_{wind} transferred through the interception area of the blades A_{turb} is given by

$$P_{wind} = \frac{1}{2}\,\rho_{air}\,A_{turb}\,v_{wind}^{3}, \tag{3.1}$$

where ρ_{air} is the air density.

Normally, the wind turbines are feasible to build in areas where the average wind speed exceeds $4.5\,\mathrm{m/s}$. Depending on the location, the following three types of sites are recognized:

- *Onshore*. An onshore wind turbine is typically installed in the hilly or mountainous areas at three kilometers or more inland from the shoreline. The wind characteristics in this area are very much dependent on the roughness of the terrain surface. Therefore, the siting of the onshore wind turbines

should be planned carefully as this, to a large extent, will affect the amount of energy produced.

- *Near-shore*. A wind turbine is considered to be near-shore if it is sited in the zone starting from three kilometers on land and up to ten kilometers on water. Wind in this zone has both onshore and offshore characteristics. Siting of near-shore wind turbines can be sometimes highly unfavorable as coastal sites are often picturesque and important from the environmental point of view, for example used for bird nesting.

- *Offshore*. Wind turbines of this type are sited on water at a distance of ten kilometers or more from land where wind speed is often significantly higher than onshore. This results in a potentially higher energy production. Because of stronger winds and a smoother surface, an offshore wind turbine can also be manufactured with a lower tower. The accessibility of offshore wind farms is however worse than those onshore, which can significantly increase their operation and maintenance costs.

3.2 Constant and Variable Speed Wind Turbines

Wind turbines can be operated either at fixed or variable speed. Fixed-speed wind turbines use an older and relatively simple technology with a constant-speed mechanical input. They are often intended only for a certain wind speed at which the maximum efficiency can be achieved. The rotational speed of an electrical generator can be changed in a stepwise manner by changing the pole number. For example, the synchronous speed can be changed from 1500 rpm to 1000 rpm by switching the pole number from four to six.

Because of the fluctuations of generated power, fixed-speed turbines have a less positive impact on power systems, as compared to the variable speed turbines. Turbines of the latter type have the possibility to control the frequency and the amount of produced electricity, although that would require a more complicated electrical system. Variable-speed wind turbines can also be designed for a broader wind speed range.

3.3 Geared and Gearless Wind Turbines

Depending on the type of the drivetrain and electromechanical energy converter, all wind turbines are divided into geared, which are more common, and gearless, also referred to as direct-driven. An overview of available wind energy systems is presented below.

Geared Wind Turbines

The basic wind turbine configuration with a fixed-speed mechanical input is illustrated in Fig. 3.1(a). The shaft of the electric generator (typically, a squirrel cage induction generator) is connected to the turbine shaft through a step-up gearbox. The gearbox is introduced to adjust a low-speed turbine shaft (in the range of tens of rpm) to the higher rotational speed of a conventional generator (up to several thousands of rpm) with the gear ratio of approximately 100. To compensate the reactive power consumed by the induction generator, a capacitor bank is integrated into the system. The soft-starter is used to provide a softer connection to the grid. The configuration presented in Fig 3.1(a) with a squirrel cage induction generator and an active stall control was for example employed by Bonus Energy A/S which has been later acquired by Siemens Power Systems [11].

The wind turbine configuration presented in Fig. 3.1(b) comprises a wound rotor induction generator with a soft-starter, and a capacitor bank incorporated in the system for reactive power compensation. The stator windings of the generator are connected to the grid while the rotor windings are connected to the variable resistance bank. By varying the rotor resistance, the generator rotational speed can be adjusted. The interval of these adjustments is however relatively small – typically, not more than 10% above the synchronous speed. Turbines of this type are often said to have a limited variable speed. Among others, this configuration is used by Vestas [12] in their *V90* wind turbines.

The configuration depicted in Fig. 3.1(c) uses a doubly-fed induction generator concept, where the stator winding of a wound rotor induction generator is directly connected to the grid whereas the rotor winding is connected through a frequency converter. The power converter, rated only for a part of the generator nominal output power (about 30 %), is used to regulate the production of reactive power and to smoothen the grid connection. In comparison with the concept in Fig. 3.1(b), the speed of the doubly-fed induction generator can vary within a larger range. Depending on the converter nominal power, it can vary within the interval between 40% below and 30% above the synchronous speed. This configuration is widely used by wind turbine manufacturers. It is for instance adopted in one of the largest wind turbines – the 5 MW wind turbine *5M* manufactured by REpower [13].

The wind turbines shown in Figs. 3.1(d,e) have similar electrical parts in which the generator is connected to the grid through the frequency converter. The mechanical parts are however quite different. In the topology in Fig. 3.1(d), the turbine shaft and generator shaft are coupled to each other through a step-up gearbox, in this way making it similar to the previously discussed wind turbines. This arrangement with a permanent magnet synchronous generator is used, for exam-

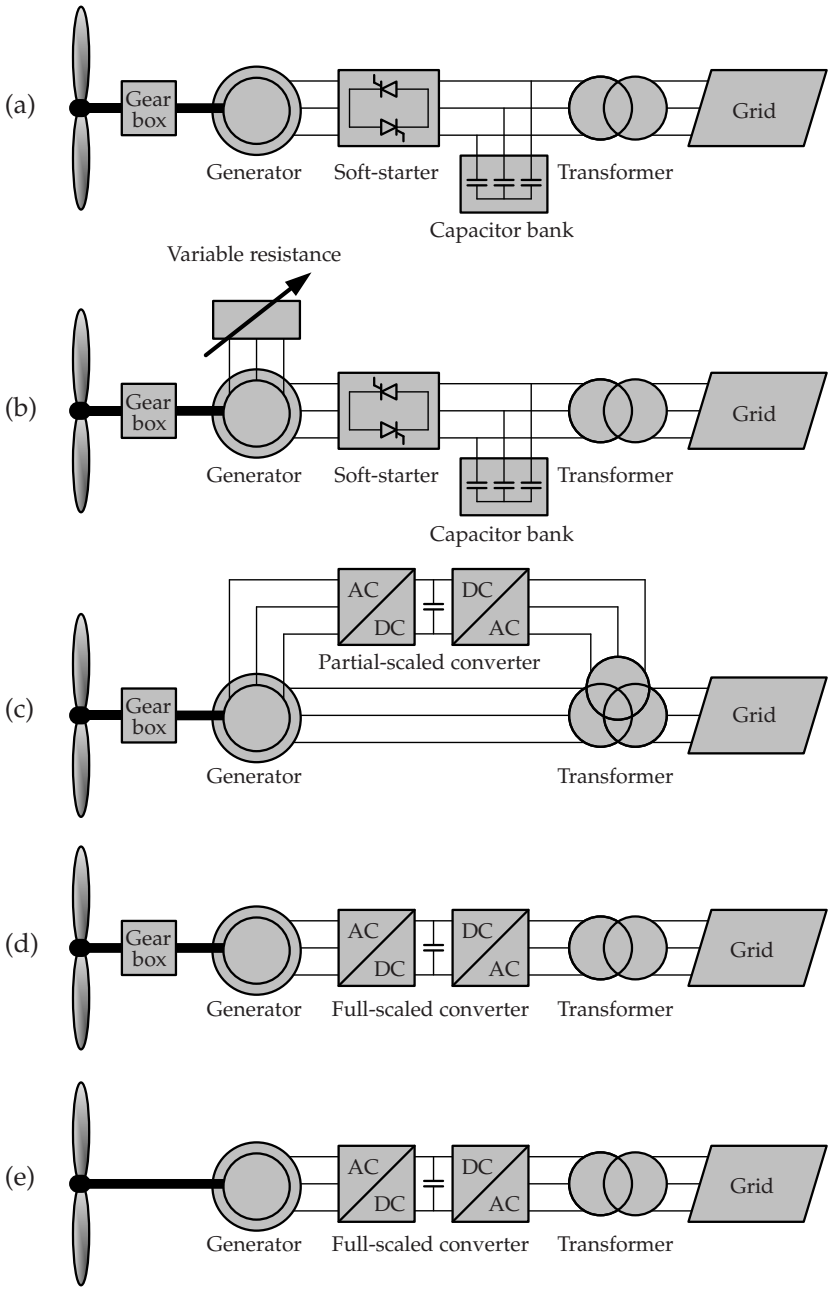

Figure 3.1: Common wind turbine configurations.

ple, in Vestas *V112* 3 MW wind turbine.

A permanent magnet synchronous generator is also employed in the 5 MW *M5000* Multibrid wind turbine [14]. However, in this concept, the gear ratio between the turbine and generator speed is only about 10, resulting in a generator with the medium torque and rotational speed. It can therefore be considered as an intermediate step between conventional high-speed/low-torque generators and the low-speed/high-torque generator applied in the gearless system in Fig. 3.1(e).

Gearless Wind Turbines

With further development of wind turbine technology and increased wind power penetration level in power systems, the issues of reliability of generating units become of greater importance. This particularly applies for stand-alone and offshore applications due to their often hard-to-reach locations. The overall reliability of a wind turbine is reduced by the use of a gearbox in wind energy systems depicted in Figs. 3.1(a-d). Although the rate of failures in the direct-driven wind turbines depicted in Fig. 3.1 (e) is higher, mainly due to the failures in the electrical system, the annual downtime is yet lowest [15]. As compared to the turbines with the variable speed control in Fig. 3.1(c,d), the gearless concept can reduce the downtime of the generating unit by three to four times, thus improving its overall availability.

In addition, the gearbox is subject to mechanical wear, vibrations, requires lubrication and more frequent maintenance at considerable cost [16]. As a result, the gearless wind energy system has drawn the attention of wind turbine manufacturers. A schematic of such system is presented in Fig. 3.1(e).

For the connection of a generator to the network, a converter scaled for the full output power is required. This introduces extra cost and additional losses; yet, the efficiency of such a system can be higher than the efficiency of the system containing a gearbox and an induction generator directly connected to the grid [17]. On the other hand, a full-scaled converter offers an opportunity of a variable speed control over a large speed range. This allows a better utilization of the available wind power and therefore has a potentially higher energy yield. The interest in gearless energy systems is likely to continue in the near future as larger power converters become available at decreasing cost.

3.4 Direct-driven Wind Generators

A direct-driven low-speed generator with a large number of poles and an outer diameter larger than conventional generator is required in the gearless wind system presented in Fig. 3.1(e). Electrically excited direct-driven synchronous and induc-

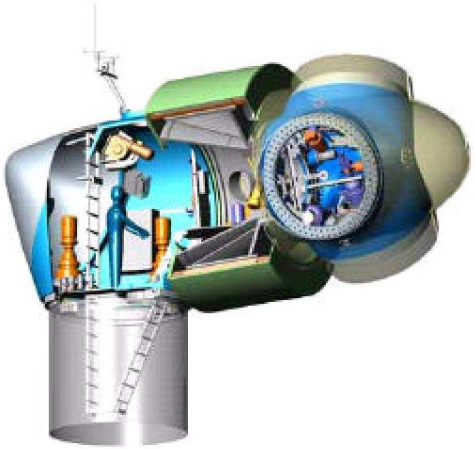

Figure 3.2: Nacelle of the gearless energy system with the permanent-magnet direct-driven generator *STX72* as described in [20].

tion generators are used by a number of wind turbine manufacturers. Wound rotor induction generators are for example used by Enercon.

In the last few decades, a reduced magnet price has made synchronous generators with permanent magnet excitation an attractive alternative. In comparison to the electrical excitation, the permanent magnet excitation favors a reduced active weight and decreased copper losses, yet the energy yield is higher [18].

This topology is for example employed by STX Windpower B.V. in its 2 MW wind turbine *STX72* (formal Zyphyros *Z72*) whose nacelle is depicted in Fig. 3.2, making it one of the largest direct-driven permanent magnet generators commercially available [19]. The generator employs a radial-flux permanent magnet configuration [20].

Besides the existing ones, some permanent magnet generators for direct-driven wind turbines are currently under development. One of them is designed and produced at VG Power in Västerås, Sweden. The main feature of this generator is that by placing the bearings in the airgap, reduced weight can be achieved [21]. The 144 kW downscaled prototype shown in Fig. 3.3 has been built and tested proving viability of the concept. A 3 MW prototype with a 9 m diameter is intended to be manufactured for installation on the Swedish island of Gotland [22].

A number of studies have been conducted investigating different topologies of permanent magnet synchronous generators suited for direct-driven low-speed wind generators [17, 23]. A possibility of utilizing a transverse flux permanent magnet topology in the gearless wind energy system was discussed by Profes-

Figure 3.3: A prototype of the direct-driven generator developed by VG Power as illustrated in [21].

sor Weh in [24] as early as in 1990. An attractive feature of the transverse flux machines is that with an increasing number of poles, the machine rating can be increased and as a result a higher value of specific torque density can be achieved [25].

A. Grauers in [17] has considered different permanent magnet synchronous generators suited for a direct-driven wind turbine generator. The author analyzed radial, axial and transverse flux generators in the range from 30 kW to 3 MWA. The study showed that transverse flux generator was superior to others due to its high efficiency, light weight and compactness.

The research started in [17] with a particular focus on the transverse flux generators was continued by J. Hystad in [26]; generators with the iron bridge structure and the double-sided topologies were analyzed in his thesis. The double-sided configuration was found to be the most economically feasible alternative, especially with the decreasing price of the power electronics. The author however stresses that an extra emphasis should be put on reducing the manufacturing cost of the magnetic parts.

A more detailed description of different configurations of permanent-magnet machines, their principles of operation and areas of application are discussed in the next chapter.

3.5 Conclusions

In this chapter, the basics of wind energy conversion have been introduced. The siting of wind turbines is of importance as far as the components of the wind turbine and their maintenance are of concern. As for example, the wind turbines sited offshore would most probably experience higher winds which would lead to a higher annual energy yield. The accessibility of these turbines is however generally reduced due to their remote location.

The basic difference between the turbines with the fixed and variable speed control has been described. Five different configurations of wind energy systems have been presented, four of which utilized a gearbox in order to adjust the slow turbine shaft to a generally higher rotational speed of the generator. Examples of manufacturers using these configurations have been given. The emphasis has been placed on the direct-driven wind turbines and the topologies that could be employed in the energy converters. Following the literature review, the transverse flux topology has been found to be a promising alternative for the direct-driven wind turbine.

Chapter 4

Transverse Flux Machines

A general overview of various permanent magnet synchronous machines is provided in this chapter. The prominent features of different configurations are highlighted and discussed: radial flux, axial flux and transverse flux. The emphasis is however placed on the transverse flux topology and its principles of operation. Various configurations of transverse flux topologies are reviewed and their properties are outlined.

4.1 Configurations of Permanent Magnet Synchronous Machines

Depending on the direction of the flux lines crossing the airgap, the following configurations of permanent-magnet machines are recognized: radial flux, axial flux and transverse flux. Their principles of operation and possible arrangements are discussed below.

Radial Flux Configuration

A radial flux configuration is the most common configuration of permanent-magnet synchronous machines (PMSM). The machines of this type are widely used in various applications, such as traction [28, 29], ship propulsion systems, wind power generation [20], robotics, and many others.

An overview of the radial flux PMSM is shown in Fig. 4.1(a). The flux lines are in the radial plane, while the current flows in the axial direction. The stator of the radial flux PMSM resembles that of a conventional AC machine, which makes it easier to manufacture due to existing and well-proven technology and availability of tools and machinery.

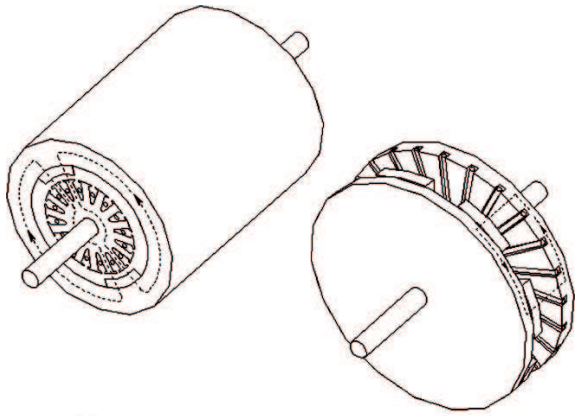

(a) (b)

Figure 4.1: An overview of permanent magnet machines with (a) the radial flux and (b) the axial flux configurations [27]

Depending on the way the permanent magnets are placed in the mover, the permanent magnet machine has several design possibilities. The most common designs used in the conventional radial flux machine are the surface-mounted, inset, and buried. Selection of a design affects the machine performance, its weight and overall production cost.

Surface-magnet Design

In the configuration with the surface-mounted magnets (Fig. 4.2(a)), the magnets are polarized radially or sometimes along the circumference. The bandaging of such a machine is often necessary in order to protect magnets from the centrifugal forces. The reactances in the d- and q-axes are nearly the same. The construction of such a rotor is simpler than for the other rotor designs.

Inset-magnet Design

The inset-magnet rotor (Fig. 4.2(b)), has radially polarized magnets embedded in the slots on the rotor surface. The synchronous reactance is larger in the q-axis than in the d-axis. The emf induced by the magnets is generally lower than in the surface-mounted rotor design, due to larger flux leakage [30]. The rotor in this design is likely to be lighter.

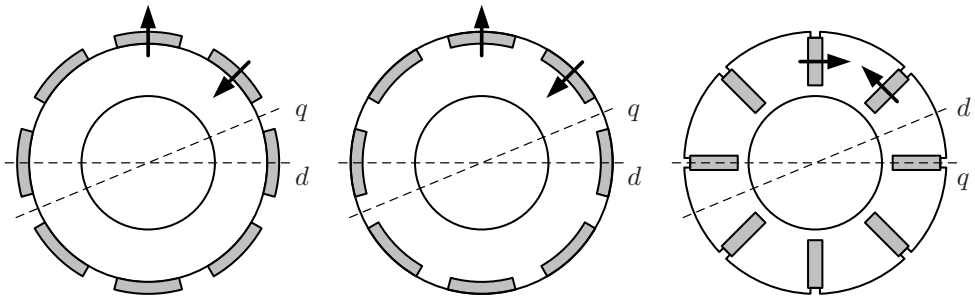

(a) (b) (c)

Figure 4.2: Rotor configurations: (a) surface-mounted magnets, (b) inset magnets, (c) buried magnets.

Buried-magnet Design

In the buried-magnet rotor (Fig. 4.2(c)) the magnets are magnetized circumferentially. The synchronous reactance in the *q*-axis is larger than in *d*-axis. The thickness of the bridge between the magnets should be carefully chosen. In this configuration a non-magnetic shaft should preferably be used. The advantage of this rotor design is that the airgap flux density can be greater that the remanent flux density of the permanent magnets.

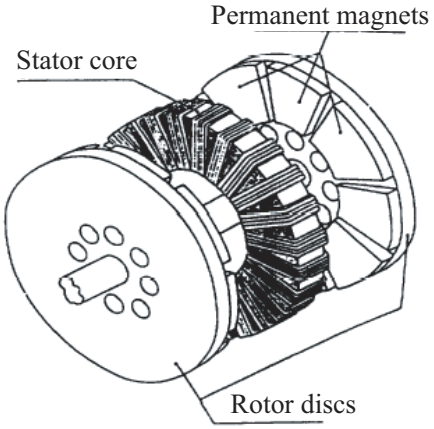

Figure 4.3: Axial flux machine 'TORUS' [31].

Axial Flux Configuration

The machine shown in Fig. 4.1(b) employs an axial flux configuration. The flux lines are crossing the airgap in the axial direction, while the windings are arranged radially. As can be seen in the figure, the machine with this topology has a larger diameter-to-active-length ratio as compared to the earlier discussed radial flux machines. The axial flux PMSM consists of two discs: the rotor disc with the permanent magnets and the stator disc with the armature winding placed in the slots. Similarly to the radial flux PMSM, the rotor can have either axially-polarized magnets placed on its surface or radially-polarized magnets embedded in its core. The machines of this type are used in traction and servo applications, distributed generation and propulsion systems [27].

A number of various axial flux configurations have been proposed. Among them the following topologies can be distinguished: single and double sided, multi-disc and 'TORUS' [32, 33]. An overview of this machine is depicted in Fig. 4.3. It consists of double-sided rotor with the permanent magnets and the stator with the toroidal winding placed amid.

The possible use of the axial flux PMSM of the type 'TORUS' for a direct-driven wind generator has been investigated by numerous researchers since it was proposed in [32]. The machine was found to be a competitive alternative due to large available torque-per-volume ratio.

Transverse Flux Configuration

The direct-driven synchronous generator analyzed in the present work employs a transverse flux topology (Fig. 4.4). Use of transverse flux machines has been investigated in different areas where the high torque density or a multi-pole machines were required [34]. These areas include wind energy [24, 23], free-piston generators for hybrid vehicles [35, 36], ship propulsion systems, etc.

Unlike in conventional radial flux machines, the flux lines in this topology lie in the perpendicular or, in other words, transversal plane to the direction of movement and that of current flow. The pros and cons of the transverse flux topology are described in the following section.

4.2 Description of Transverse Flux Topology

One of the main benefits of using a transverse flux topology is the possibility to attain a high torque density [24]. By increasing the number of poles (thus decreasing the pole length) for given dimensions and current loading, the machine rating can be increased and, consequently, higher values of specific torque density can

be achieved. Values of current loading up to $300\,\mathrm{kA/m}$ and force density up to $150\,\mathrm{kN/m^3}$ have been reported [37]. However, the pole pitch has a lower bound and therefore should be checked for mechanical rigidity when designing a transverse flux machine (TFM). Furthermore, the amount of the flux leakage produced in the direction of movement, as shown in the following chapters, is also very much related to the pole length.

Another attractive feature of a TFM is that it allows current and magnetic loading to be set almost independently. The pole length sets the magnetic loading, whereas the machine width determines the current loading. This advantageous feature of the TFM results in a more favorable construction, as the magnetic circuit and armature winding are not competing for the same space.

One of the major drawbacks of a TFM is its high flux leakage, resulting in a poor power factor. The amount of leakage flux can be reduced to a certain extent by increasing the pole width at the cost of relinquished high torque density. Therefore, the machine designer has to consider this trade-off between machine performance and utilization of active materials and find an optimal solution [38]. On the other hand, the large leakage reactance would limit the short-circuit current, in case of a failure.

Another significant disadvantage of a TFM is the complicated mechanical structure of the magnetic circuit. It consists of a large number of separate small-size components, thereby resulting in a relatively weak construction and more com-

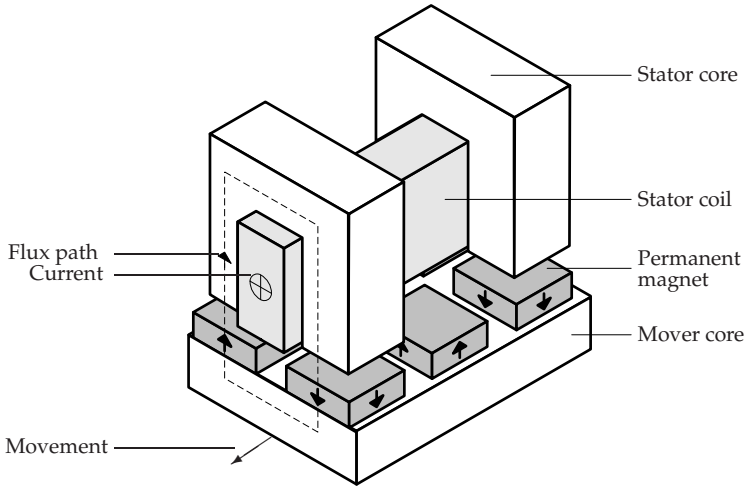

Figure 4.4: Basic single-phase transverse flux topology with permanent magnet excitation.

plex manufacturing.

4.3 Variety of Transverse Flux Topologies

Depending on the type of excitation, a transverse flux machine can either be electrically excited or magnetically excited [39]. An electrically excited machine normally has a more massive rotor and larger weight as compared to a magnetically excited one. The reduced magnet prices have made permanent magnet machines more feasible than before.

A number of various topologies of TFM are presented and described in the literature since it first drew the attention of machine researchers in the early 1970s [40] and later re-emerged in the mid-1980s [25]. Nevertheless, research in this area continues and new topologies are being introduced. An overview of the existing transverse flux topologies is summarized below.

Basic Transverse Flux Topology

The geometry depicted in Fig. 4.4 is a basic arrangement referred to as single-sided TFM [41]. It consists of a mover core with permanent magnets. The stator is made up of C-shaped iron cores of laminated steel. The winding is placed in the stator slots. The magnets polarized with alternating polarity are displaced on the rotor surface, thereby producing an alternating flux in the stator iron. The winding is global as the same coil links the fluxes produced by each pole pair. In the following text, this topology is refereed to as BTFM (basic transverse flux machine).

Generally speaking, transverse flux machines have a single-phase structure which is comprised by a number of separate units depicted in Fig. 4.4. The separate units are subsequently attached to each other in the direction of movement to produce a multi-pole machine, and in the lateral direction in order to produce a multi-phase machine. In case of a three-phase machine, the single-phase units should be displaced by 120 electrical degrees and the number of units should be multiple of three. The electromagnetic properties of a single unit are therefore inherited by the entire machine.

A cross-section of a three-phase TFM and a possible magnet arrangement are depicted in Fig. 4.5. The TFM has no common rotating field built by the three-phase winding. Instead, three independent alternating fields shifted by 120 electrical degrees exist (three single-phase machines stacked together). The shift is created by the magnets mechanically displaced on the rotor surface. The advantage of shifting the magnets rather than stator core pieces is that the stator cores can be joined together, thus reducing the number of separate parts and consequently the complexity of production.

Transverse Flux Topology with Iron Bridges

In the topology shown in Fig. 4.4, only half of the magnets are being utilized at one moment, while the others generate fluxes that can weaken the flux linked to the winding. To reduce the stray fluxes generated by unused magnets, guiding iron bridges could be placed between the stator cores as illustrated in Fig. 4.6. In this way, closed magnetic paths are provided for the fluxes originated by each magnet that is not involved in the development of the main magnetic flux. In this TFM arrangement, the output power would likely be higher [42]. However, the iron bridges increase the active weight of the machine and decrease the available space for the stator winding. The abbreviation IBTFM used in this thesis stands for the transverse flux machine with iron bridges.

The rotational TFM concept in [42] (Fig. 4.7) presents three single-phase machines of the type illustrated in Fig. 4.6. The magnets displaced on the rotor sur-

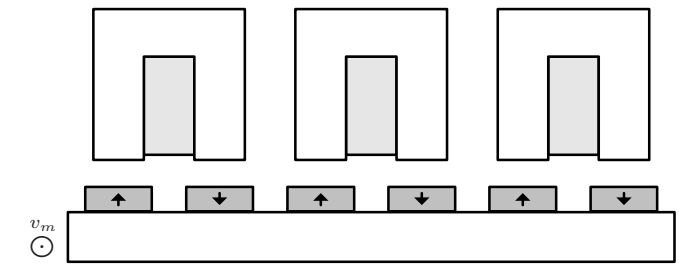

(a)

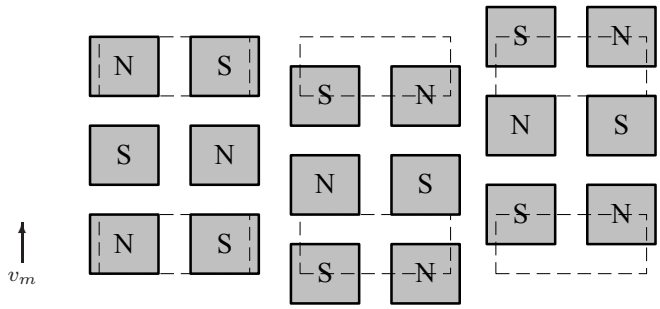

(b)

Figure 4.5: Three-phase TFM with (a) cross-section and (b) displacement of magnets, where v_m shows direction of movement.

face, while the stator core pieces are aligned. The passive iron bridges placed amid the stator stacks. An internal stator design was selected in this TFM machine, which allowed reducing the machine output diameter. The prototype was built and tested proving the viability of the adopted concept, especially in low-speed applications.

Double-sided Transverse Flux Topology

To increase the utilization of the magnets even further, the transverse flux machine can be manufactured double-sided, as shown in Fig. 4.8. This configuration consists of two sets of C-shaped cores per pole pair, with windings placed in the slots. The magnets are embedded in the rotor core. The output power of such machine can be increased even further, as each magnet contributes to the main stator flux. Considerably increased complexity and a relatively weak mechanical construction are the main disadvantages of this topology.

The topology presented in Fig. 4.8 can also be produced with only one winding with nearly the same torque production as in the double-sided TFM with two windings. It has an advantage of the reduced outer diameter and has a more simple mechanical structure [43].

The research within the area of transverse flux machines continues and new topologies and arrangements are being introduced. A review of several existing

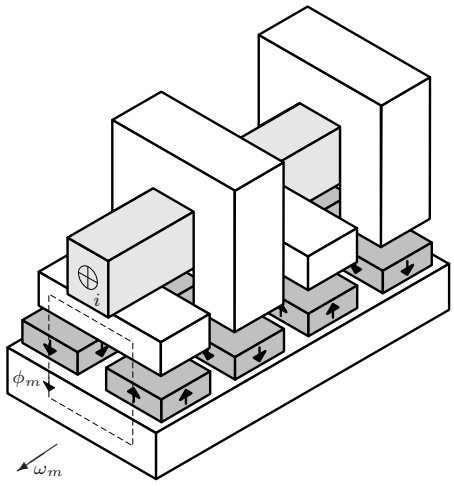

Figure 4.6: Single-sided transverse flux topology with iron bridges, where v_m is the direction of movement, ϕ_m the flux line, i is the armature current.

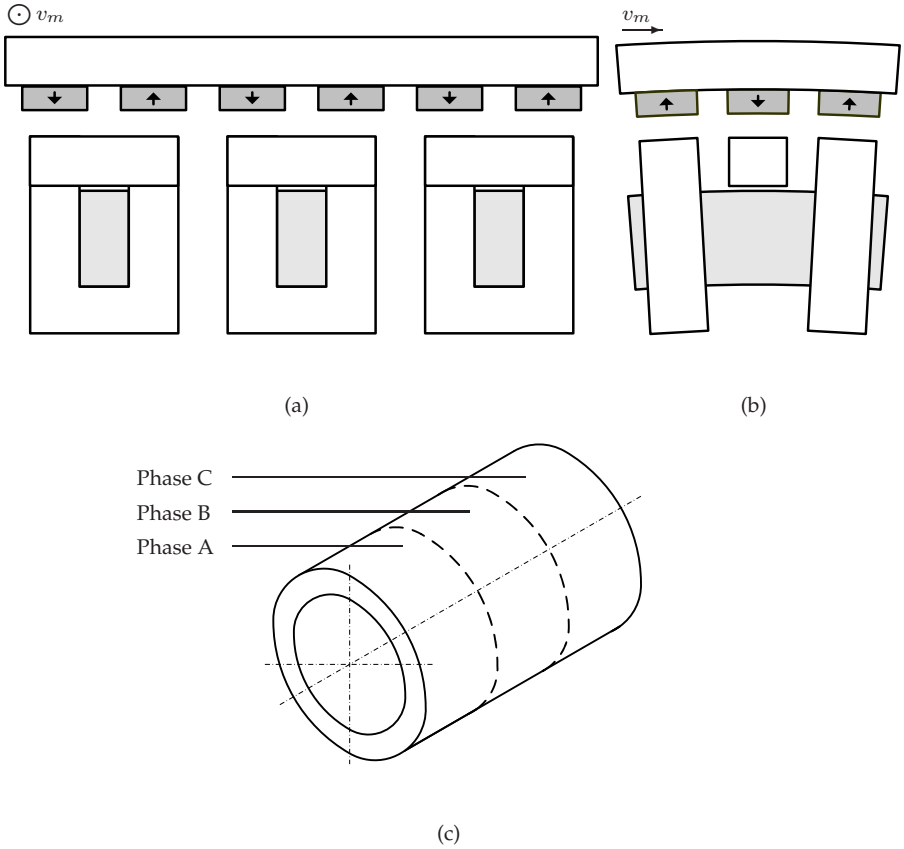

Figure 4.7: Schematic representation of transverse flux permanent magnet machine presented in [42] in (a) stack (radial) plane, (b) rotational (peripheral) plane and (c) general view of the machine.

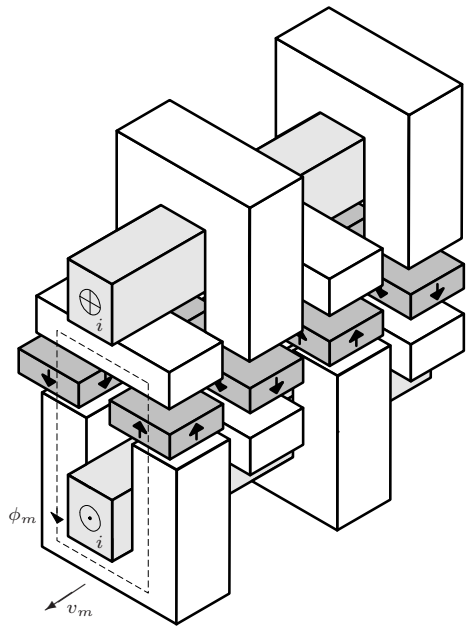

Figure 4.8: Double-sided transverse flux topology with iron bridges.

configurations is presented below.

Flux-switching Transverse-Flux Topology

One of this novel concepts is the flux switching transverse flux permanent magnet machine in Fig. 4.9, which has been described by J. Yan *et al.* in [44]. This topology inherits the properties of both transverse flux and switching reluctance machines, allowing a higher power density. The machine consists of a rotor core attached to a non-magnetic support and the stator core with the axially-polarized magnets. To produce a three-phase machine, the adjacent phases are displaced on the rotor surface by 120 electrical degrees. In [44], the computations of this machine have been performed at no-load condition showing its capability to attain a high airgap flux density.

Toothed-rotor Transverse Flux Topology

A flux-concentrating TFM topology with toothed rotor was proposed in [23]. The author claims that the analyzed topology favors the conventional permanent-magnet generator for outer diameters lower than 1 m. The machines were however com-

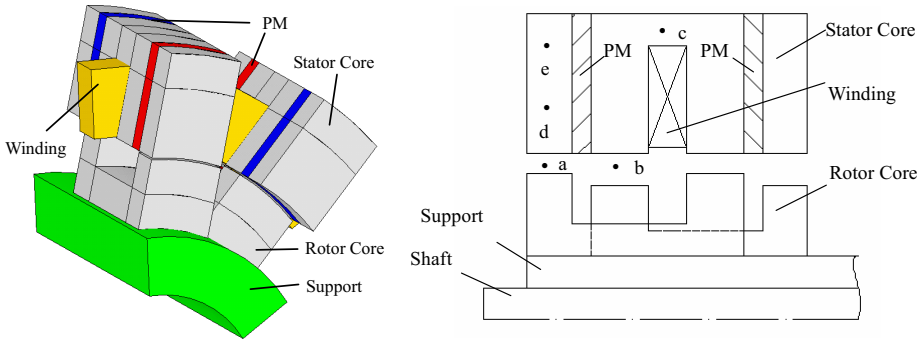

(a) General view (b) Cross section

Figure 4.9: General view (a) and a cross section (b) of the flux switching transverse flux permanent magnet generator presented in [44].

pared only with respect to the active portion of the total weight. It was therefore uncertain if this conclusion would still be valid if the inactive portion is taken into consideration.

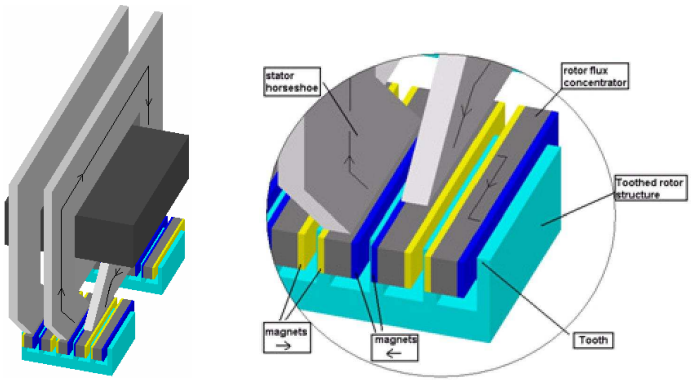

(a) General view (b) Detailed view

Figure 4.10: General (a) and detailed view (b) of the transverse flux machine with the toothed rotor described in [23].

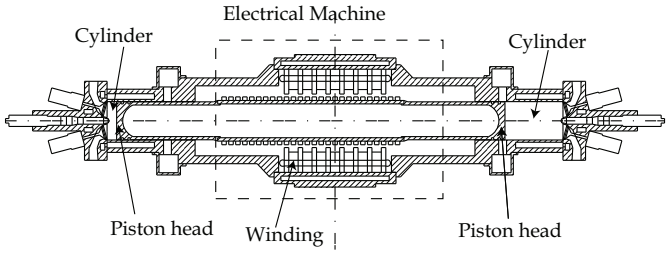

Figure 4.11: Schematic of the free piston energy converter.

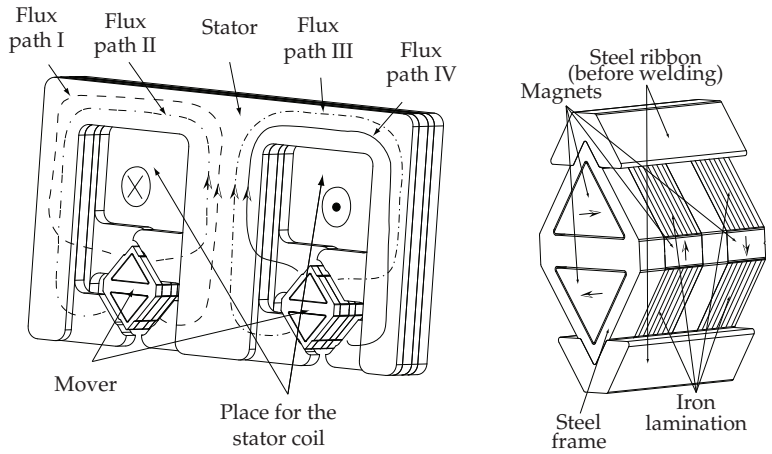

Figure 4.12: 3-D view of the Low Leakage linear TFM (a) view of a one phase (b) detailed view of the mover.

Transverse Flux Topology with Flux Concentration

In [35], the use of transverse flux machine in a linear arrangement for the free-piston generator in a hybrid vehicle has been investigated. The free-piston generator shown in Fig. 4.11 can be used in the vehicle in order to increase the efficiency of the internal combustion engine by reducing the fuel consumption. The free piston generator combines a combustion engine, crankshaft, connecting rod, and rotating electrical generator into a single unit; thus, making the system more efficient and reliable with a lighter weight [45].

A three-way flux concentration topology of the mover depicted in Fig. 4.12 has been employed. This arrangement offered a substantially reduced axial flux

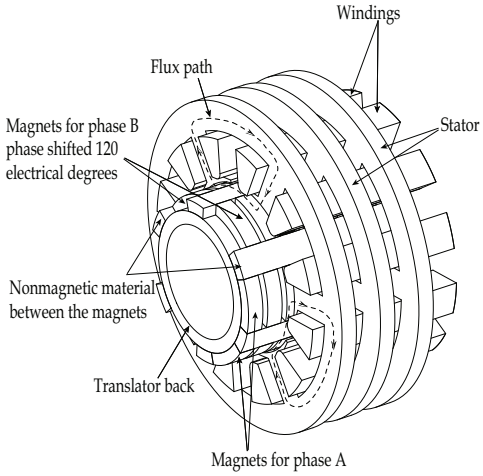

Figure 4.13: Layout of the transverse flux machine presented in [36].

leakage, but suffered from mechanical instability as a result of its complex construction.

Tubular Arrangement of TFM

The implementation of the transverse flux machines as a part of a free-piston energy converter started in [35] has been continued in [36] with the aim of improving the mechanical stability of the system. The desired mechanical stability was achieved by arranging the single-sided transverse flux units illustrated in Fig. 4.6 along a circumference, as shown in Fig. 4.13. This tubular arrangement has been patented and description can be found in [46].

4.4 Novel Transverse-Flux Arrangement

Compared to the rotational TFM topology described in [42] and depicted in Fig. 4.7, a single-phase structure (Fig. 4.14(a)) in the novel TFM is placed along the circumference rather than a straight line, thereby obtaining circular cross-section. A general view of the novel TFM arrangement is shown in Fig. 4.14(c). It employs a single-sided topology with the inner rotor and surface-mounted magnets. The generator consists of a hollow toroidal rotor with permanent magnets embraced by the laminated stacks, with the windings placed in the slots.

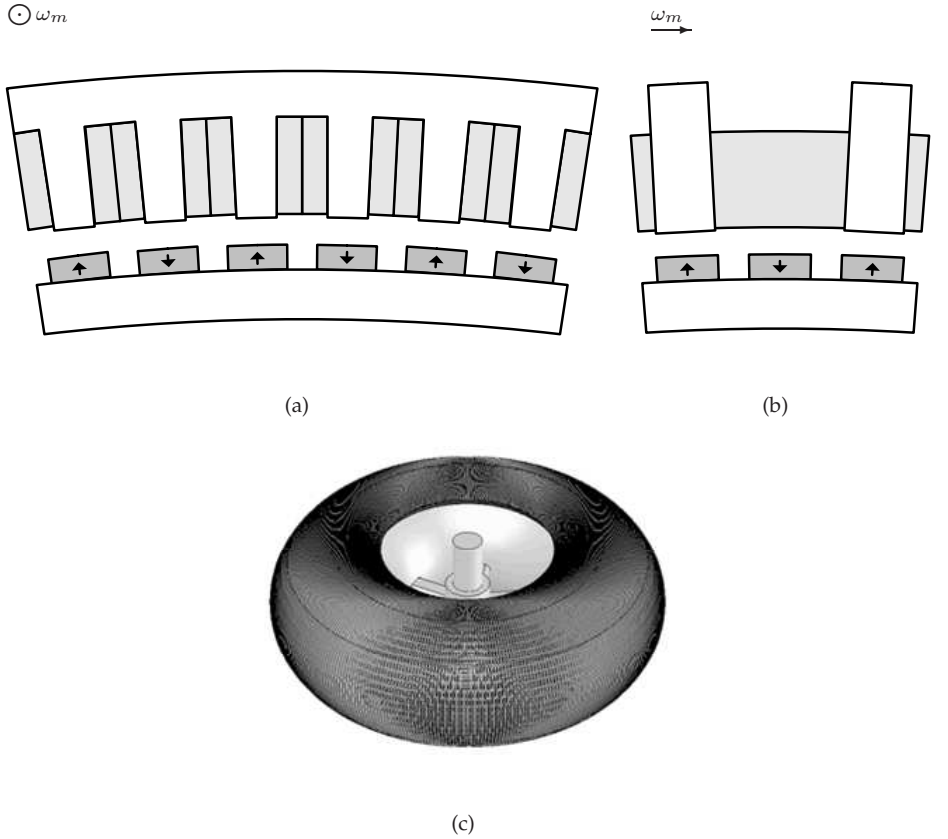

Figure 4.14: Schematic representation of the novel transverse flux permanent magnet machine in stack (radial) (a) plane, rotational (peripheral) plane (b) and general view of the generator (c).

The original idea of the analyzed generator is to use lamination sectors for the stator cores as in conventional radial flux rotational machine of a large diameter where the stator sectors are welded to each other, all along the circumference.

The high current loading allowed in a TFM could result in considerable values of armature reaction, which cause eddy current losses. To decrease this effect, the iron parts should be made of laminated material. Moreover, the transverse flux concept implies that the magnetic fluxes should be carried in the plane perpendicular to the direction of movement. Therefore, the laminated material would decrease the flux in the peripheral (rotational) direction and the fringing effect.

Arrangement of Magnets and Windings

To be able to use conventional converters for the grid connection of the generator, a three-phase system is adopted in the machine. The TFM allows using a stator winding of a simple mechanical structure, thus making it possible to facilitate high voltage insulation. This could be an attractive feature in the future since the voltage of wind generators has been continuously increasing in the past few years and voltage levels of up to $5\,\mathrm{kV}$ can reasonably be expected in the forthcoming wind generators [47]. The stator slots have a rectangular shape, as well as the conductors in the windings.

Two possible magnets and windings arrangements are shown in Figs. 4.15 and 4.16. In the case of the separated flux paths (see Fig. 4.15), the winding has a three-times single phase structure. However, in the case when the flux paths are mixed (see Fig. 4.16), the three-phase winding distribution is obtained naturally, as it is done in the radial flux machines with concentrated windings. These two possible windings will be referred to as separated and mixed windings, respectively. The separated winding structure is considered in the analyzed generator.

Dimensions of the Magnetic Circuit

The main machine radius R_m and the tube radius R_s are shown in Fig. 4.17. The cut required for the mechanical assembling of the rotor on the shaft is defined by $2\,\xi$.

The number of stator teeth per stack Q_s should be a multiple of the number of phases and a multiple of two in order to ensure the closed paths for the flux generated by the magnets of opposite polarity. Due to the introduced cut, the lateral slots (closest to the axis of rotation) contain only one winding.

The toroidal structure of the geometry results in a relatively complex analysis. It is therefore important to identify each design parameter with respect to its location. For this purpose, the subscripts 's' and 'r' were introduced in the notations, which stand for the stack (radial) plane and rotational (peripheral) plane, respectively.

The main dimensions of the generator in the stack and rotational planes are presented in Fig. 4.18. For simplicity, this figure depicts the machine in a linear representation.

4.5 Conclusions

In this chapter, an overview of permanent-magnet synchronous generators with the different ways of the force production has been presented. The pros and cons

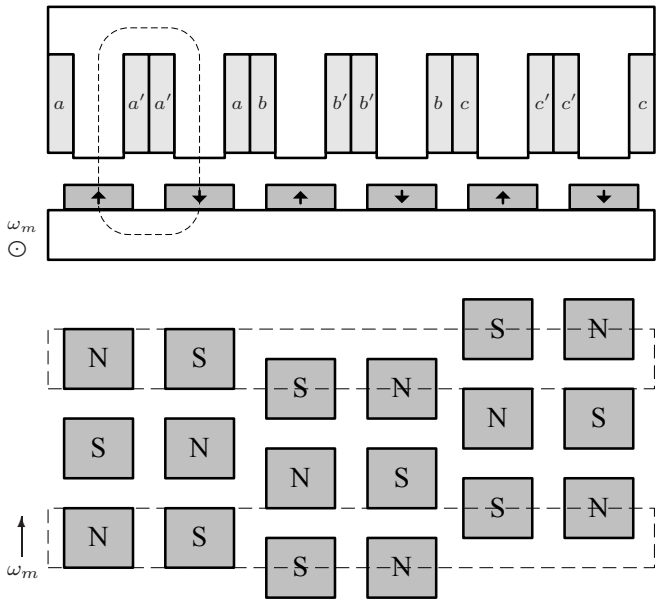

Figure 4.15: Arrangement of winding in the case of separated flux paths.

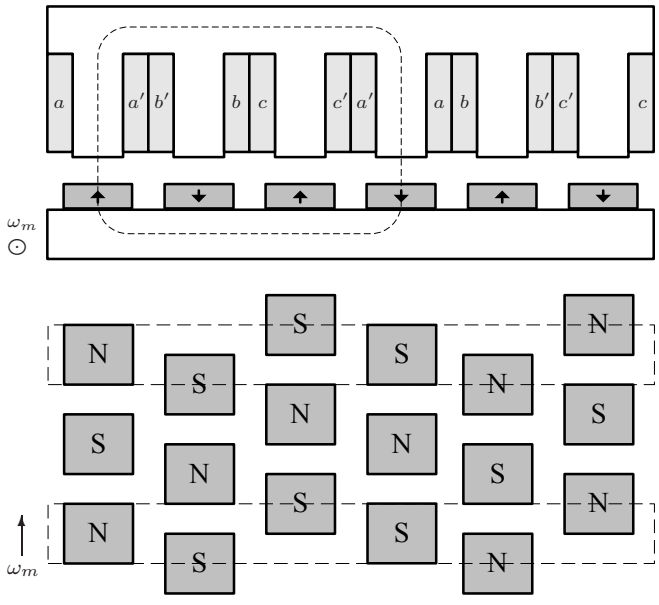

Figure 4.16: Arrangement of windings in the case of mixed flux paths.

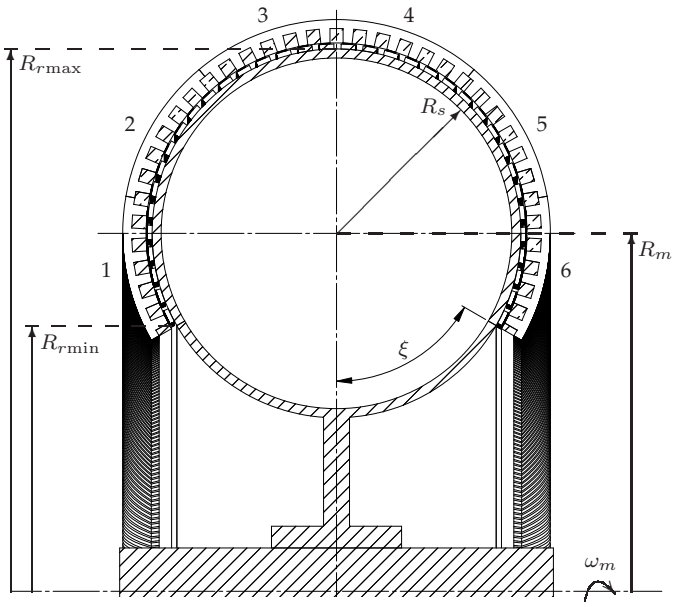

Figure 4.17: Cross-section of the novel TFM generator in the stack plane with the main dimensions.

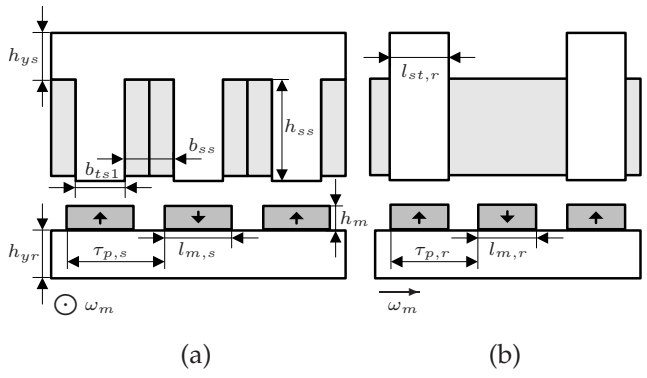

Figure 4.18: Schematic representation of the generator in the stack (radial) (a) and rotational (peripheral) (b) planes.

of each topology have been discussed. The emphasis was however placed on the transverse flux configurations and the principle of its operation. Various transverse flux topologies have been outlined and their possible applications have been discussed as well. The novel concept of arranging transverse flux units has been presented. A more detailed analysis of the novel concept can be found in the following chapters.

Chapter 5

3DFEM Analysis at No-load

This chapter deals with three-dimensional static and dynamic finite element analyses of a transverse flux permanent magnet generator suited for offshore wind turbines, at no-load. At first, dimensions of the magnetic circuit are analytically computed and then inserted into a FEM-software. Generators employing two TFM topologies are evaluated: the basic topology (BTFM) and that utilizing the iron bridge (IBTFM). The calculations are reduced to a geometry containing one pole pair with a C-shaped stator core and a slot. The flux linked to the winding obtained in the FEM simulations is compared with the flux calculated analytically in [48]. The pole-to-pole flux leakage in the topologies with the various pole length combinations is estimated. The results from the measurements of the linear prototype with the basic transverse flux topology are compared with the FEM simulations.

5.1 Model Description

A transverse flux topology has basically a single-phase structure. Therefore several single-phase units could be stacked together in such a way that a desirable multiphase machine is produced. The performance of one unit determines the performance of the entire generator, making one pole-pair model sufficient for finite element analysis.

Two transverse flux topologies – the basic topology (BTFM) and that utilizing iron bridges (IBTFM) – are considered in the wind generator described in this chapter. Their prominent features are presented in Fig. 5.1. A number of other TFM arrangements exist. Their descriptions can be found in Chapter 4 and various literature dealing with TFM, as for example in [41].

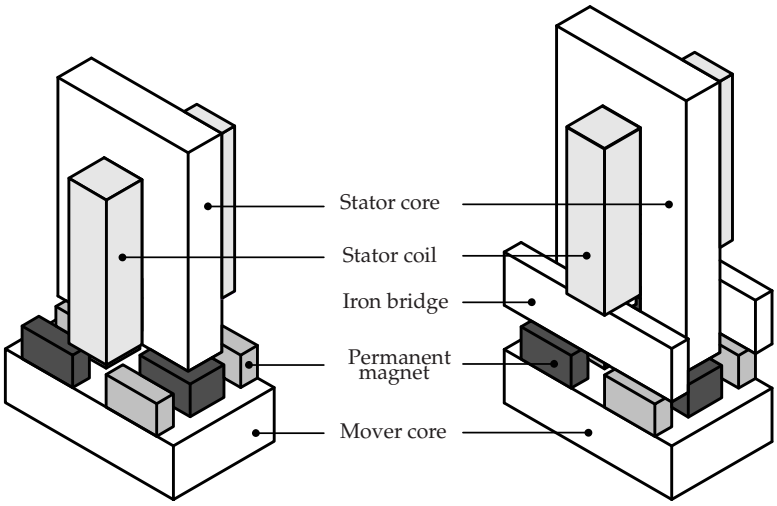

(a) Basic topology (BTFM)

(b) Topology with the iron bridges (IBTFM)

Figure 5.1: Analyzed single-phase transverse flux topologies with permanent magnet excitation.

TFM with the Basic Topology

The simulated model in Fig. 5.1(a) consists of two poles: one full and two half-poles. Different views of the model can be found in Appendix A. The model comprises a mover core with permanent magnets, the stator consisting of a C-shaped iron core and a coil placed in the stator slot. The magnets with alternating polarities are placed on the mover surface. The positive and negative polarities of the magnets are shown in light and dark gray respectively in Fig. 5.1.

To analyze the influence that the adjacent magnets have on the flux linked to the winding, the model with only two full magnets is considered for comparison. The four half-magnets are thus replaced with air. This topology could be used to quantify the magnetic flux drop due to the flux leakage in the direction of movement (a pole-to-pole leakage). In the text below, this topology is also referred to as homopolar.

TFM with the Iron Bridges

In the topology shown in Fig. 5.1(a), only half of the magnets are utilized at one instant while the others generate fluxes that partially weaken the flux linked to the winding. To reduce the stray fluxes generated by the unused magnets, guiding iron bridges could be placed between the stator cores as illustrated in Fig. 5.1(b) (Fig. A.2 in Appendix A). In such a way, closed magnetic paths are provided for the fluxes originated by each magnet that is not involved in the development of the main magnetic flux. As previously, for comparison, a model with only two working magnets is considered for this topology.

To provide the space for the iron bridges, the tooth height must be consequently increased by the height of the iron bridge (plus some extra space, which in the analysis is assumed to be 1 mm).

5.2 Analytical Calculation of Dimensions

To be able to study the generator with the use of the three-dimensional finite element method (3D FEM), the dimensions of the magnetic circuit are at first estimated analytically as described in [48]. Assuming certain input (generator rating, rotor speed, etc.) and deciding on the desired performance, the dimensions can be calculated. The assumptions outlined below are made while estimating the dimensions:

- $\widehat{B}_{iron}$ at no load is limited to $1.2\,\mathrm{T}$. The same maximum flux density is allocated in the stator teeth, stator and rotor yokes, i.e. $\widehat{B}_{iron} = \widehat{B}_{ts} = \widehat{B}_{ys} = \widehat{B}_{yr}$.
- A maximum airgap flux density created by the magnets $\widehat{B}_g = 0.8\,\mathrm{T}$ is assumed based on the magnetic properties of iron and the magnet material, as well as from prior experience.

The initial dimensions of the basic geometry corresponded to Fig. 4.18 are tabulated in Table 5.1. The dimensions with no particular topology specified are valid for both topologies.

5.3 Static Modeling in FEM

The goal of the static FEM analysis at no-load condition is to analyze the flux leakage for the given geometry, as well as to study the influence of the axial pole length on the flux linkage.

Table 5.1: Dimensions of the initial geometry in (mm).

Property	Value
Stack (radial) plane:	
Slot height in the BTFM h_{ss}	42.5
Slot height in the IBTFM h_{ssi}	57.3
Slot thickness b_{ss}	11.2
Tooth thickness b_{ts}	13.8
Stator yoke height h_{ys}	13.8
Rotor yoke height h_{yr}	13.8
Pole length $\tau_{p,s}$	25.0
Magnet length $l_{m,s}$	15.0
Magnet height h_m	8.4
Airgap thickness g	3.0
Iron bridge height in IBTFM h_{ib}	13.8
Movement (peripheral) plane:	
Pole length $\tau_{p,r}$	15.0
Magnet thickness $l_{m,r}$	10.0
Stack thickness $l_{st,r}$	10.0
Iron bridge thickness in IBTFM $l_{ib,r}$	10.0

General Considerations

The following considerations are made while modeling TFM in 3D FEM software FLUX3D:

- A single-phase model is assumed; thus, no mutual effect of the other phases is included.
- D-axis simulations, i.e. the position at which the stack is aligned with the permanent magnets, are conducted (as shown in Fig. 5.2).
- As the periodic boundary conditions are applied, an identical mesh is required at the boundaries in the direction of movement (periodic boundary

conditions in Fig. 5.2). This can be attained through propagation of the boundary surfaces and associated linked mesh.

- A better control over the mesh in the airgap is achieved by dividing it into two layers: the upper layer – attached to the stator surface, and the lower one – appended to the mover. The divided airgap is also required in the dynamic 3D FEM analysis.
- An air volume surrounding the analyzed geometry is assumed. The Dirichlet boundary conditions with the normal magnetic field are manually specified on the external surfaces (Fig. 5.2).
- A non-meshed coil with one turn is used. It carries no current as no-load simulations are conducted. The coil length should be selected large enough to ensure that the end effect has negligible influence on the flux linkage. In Fig. 5.2, only a part of a non-meshed coil is shown.
- Data for magnetic steel M600-50A is employed in the iron parts and data for NdFeB with $B_{rpm} = 1.1\,\mathrm{T}$ and $\mu_{rpm} = 1.05$ is used for the permanent magnet material.

Analysis of the Initial Geometry

The models have been built in the 3D FEM software according to the guidelines summarized above, and the dimensions have been selected as outlined in Table 5.1. The flux linked with the winding (or the flux linkage as the winding has only one turn) $\Phi_{winding}$ obtained for the four different topologies is listed in Table 5.2. The flux obtained by integrating the flux density over the tooth base area Φ_{tooth} is also tabulated.

The airgap flux leakage can be estimated by comparing the flux entering the tooth base in TFM models with two and four working magnets. In the BTFM, 20% of the flux produced by the magnets leaks in the airgap to the neighboring magnets, i.e. a magnitude $79.4\,\mathrm{Wb}$ is reduced to $62.7\,\mathrm{Wb}$. Thanks to the iron bridges used in the IBTFM topology, the airgap flux leakage can be decreased to 12% of the magnetic flux (magnitude $79.7\,\mathrm{Wb}$ is reduced to $70.0\,\mathrm{Wb}$).

The airgap flux leakage can also be studied by analyzing the flux density in the airgap. The x, y, z components as well as the modulus of the magnetic flux density in the middle of the airgap are plotted in Fig. 5.3. The stack plane (SP), or radial plane, of the geometry corresponds to the x-direction in Fig. A.1 Appendix A, while the movement plane (RP), or peripheral plane, aligns with the y-direction.

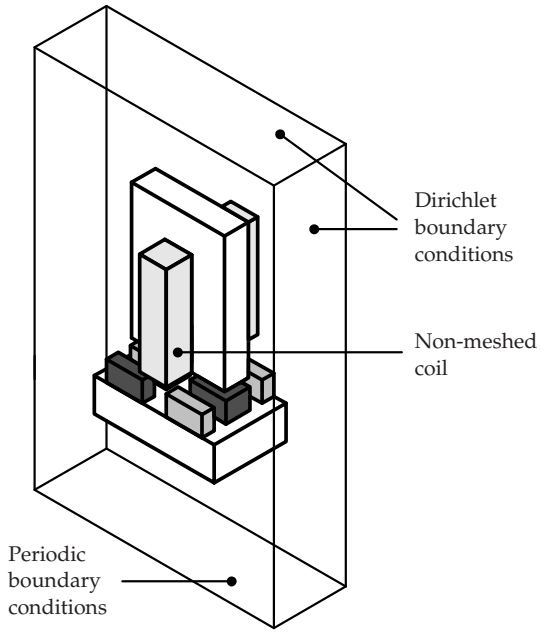

Figure 5.2: Model used in the FEM software.

Table 5.2: Fluxes in different parts of the studied models in $\mu\mathrm{Wb}$

Model	$\Phi_{winding}$	Φ_{tooth}
BTFM with four working magnets	36.6	62.7
BTFM with two working magnets	98.9	79.4
IBTFM with four working magnets	74.6	70.0
IBTFM with two working magnets	97.8	79.7

The maximum values of the flux densities in the different directions are tabulated in Table 5.3.

The useful flux produced by the magnets is in the z-direction. The maximum flux density in the airgap obtained in FEM for the given geometry is $\widehat{B}_g \approx 0.6\,\mathrm{T}$ (Table 5.3, Fig. 5.3(c)). The machine was however analytically designed for $\widehat{B}_g = 0.8\,\mathrm{T}$.

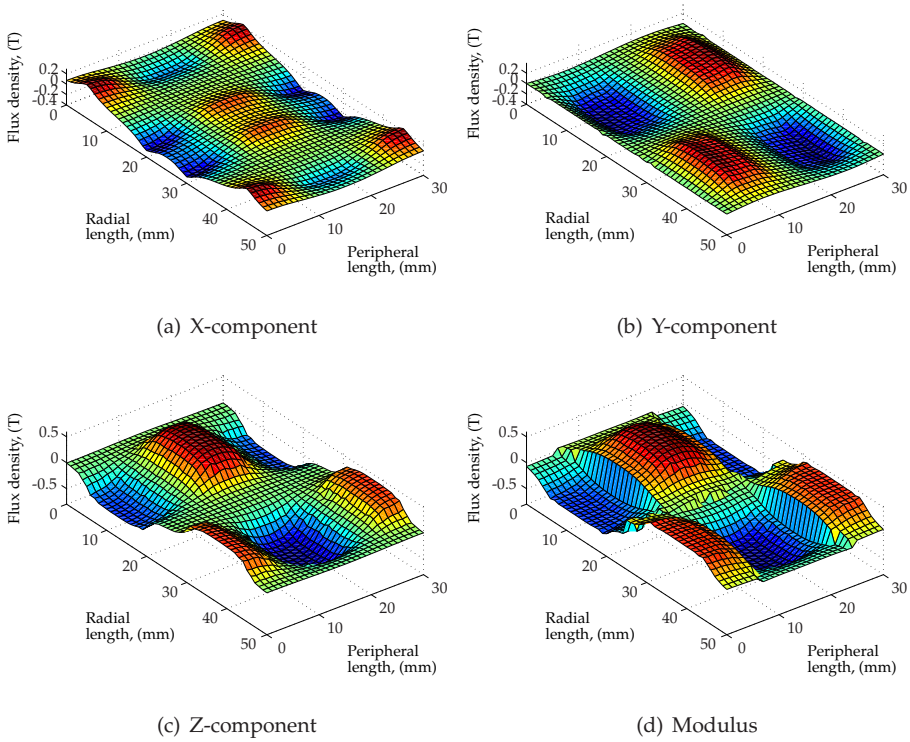

(a) X-component

(b) Y-component

(c) Z-component

(d) Modulus

Figure 5.3: Flux density in the middle of the airgap for the TFM with the basic topology.

Table 5.3: Maximum flux density in the middle of the airgap in (T)

Model	$\widehat{B}_x$	$\widehat{B}_y$	$\widehat{B}_z$	$\widehat{B}_g$
BTFM with 4 working magnets	0.25	0.33	0.59	0.59
BTFM with 2 working magnets	0.14	0.13	0.64	0.64
IBTFM with 4 working magnets	0.16	0.20	0.61	0.61
IBTFM with 2 working magnets	0.15	0.13	0.64	0.64

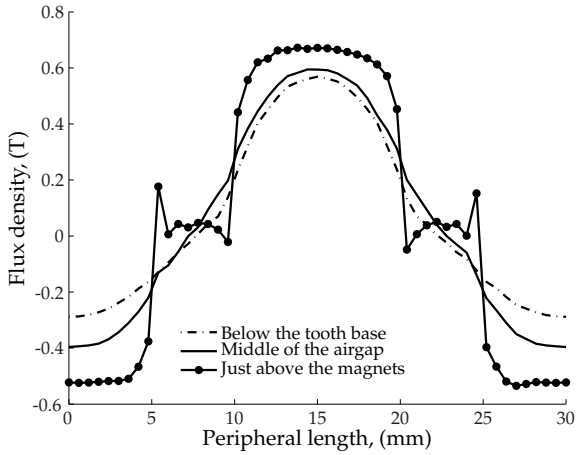

Figure 5.4: Variation of the flux density B_z in the airgap just above the magnets, in the middle of the airgap, and just below the tooth base.

The difference in the analytical and FEM results can be explained by numerous reasons. One reason for this is that the leakage flux from the adjacent magnets in the direction of movement (y-direction) was omitted in the analytical calculations. Fig. 5.3(b) shows the distribution of B_y in the middle of the airgap. As can be observed, the topology suffers from a substantial pole-to-pole flux leakage, with a maximum of 0.33 T. This is confirmed by comparing the results with the values obtained in the homopolar topology, where B_y attains only 0.13 T.

Another source of discrepancy is the variation of the maximum flux density in the airgap $\widehat{B}_g$ which varies depending on the distance from the magnet. The $\widehat{B}_z$ distribution for the three locations: just above the magnets, in the middle of the airgap, and below the tooth base is depicted in Fig. 5.4. The peak values of the z-component attain 0.69, 0.59 and 0.57 T, for the three locations respectively.

The flux that is actually linked with the winding is reduced even further in the BTFM topology. In the model with four working magnets the flux linkage is approximately 40% lower than the flux entering the tooth base. However, the flux linkage in the IBTFM is higher. To explain this, the variation of the flux along the tooth is studied. The fluxes are calculated by integrating the flux density over the slices as shown in Fig. 5.5(a).

The flux variation along the tooth for the four different models is shown in Fig. 5.5(b). Due to the absence of the adjacent magnets in the one-pole or two-magnets models (models marked '2pm' in the figure), the flux linkage increases gradually for the first 10 mm as a result of fringing and retains its value thereafter.

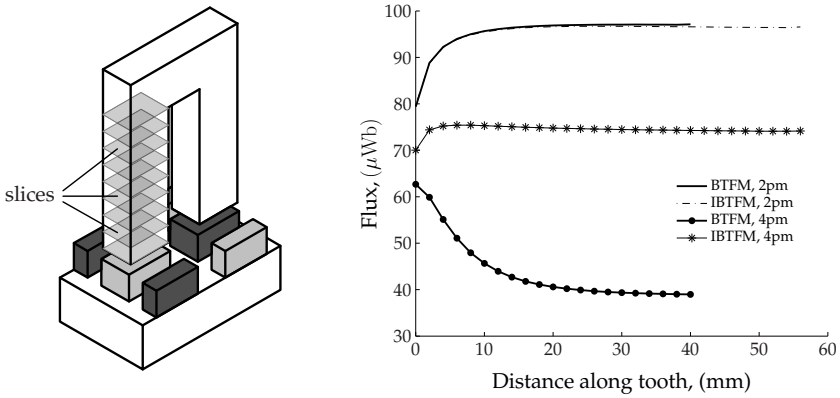

(a) FEM model (b) Flux evolution

Figure 5.5: Model used in FEM for calculation of the flux in the tooth (a) and flux evolution along the tooth length (b).

The flux linkage in these topologies is thus around 25% higher as compared to the flux at the tooth base.

In the BTFM with two poles ('BTFM, 4pm'), the adjacent magnets generate stray fluxes that weaken the useful magnetic flux, causing a drop of around 40% (as mentioned earlier) as illustrated by Fig. 5.6(a) and Fig. 5.6(b). The iron bridges in the IBTFM with two poles ('IBTFM, 4pm') short-circuit the adjacent magnets, increasing the flux linkage for this topology (see Fig. 5.6(c)). This implies that smaller magnets can be used in IBTFM as compared to BTFM to produce the same amount of flux, which makes the IBTFM a more favorable topology as far as the utilization of the magnet material is concerned.

To validate the last statement, the calculations performed for one set of dimensions (see Table 5.1) are extended to varying dimensions in the movement plane for both topologies.

Parametric Study of BTFM

The flux linkage $\Phi_{winding}$, flux linkage per magnet volume ($\Phi_{winding}/V_{pm}$) and the pole-to-pole flux leakage are calculated for the following dimensions:

Pole pitch $\tau_{p,r} = [8, 15]\,\mathrm{mm}$.

Magnet thickness $l_{m,r} = [5, (\tau_{p,r} - 2)]\,\mathrm{mm}$.

Stack thickness $l_{st,r} = [5, (\tau_{p,r} - 2)]\,\mathrm{mm}$.

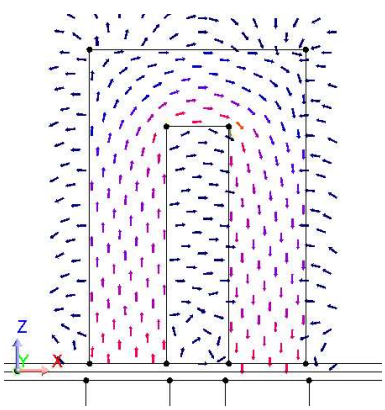

(a) BTFM with 4 working magnets

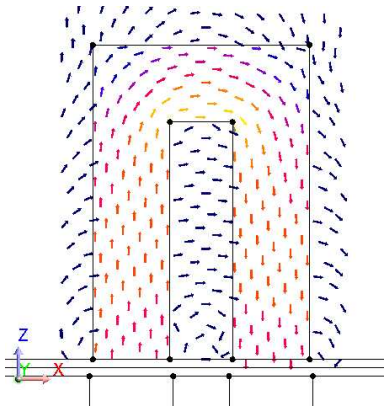

(b) BTFM with 2 working magnets

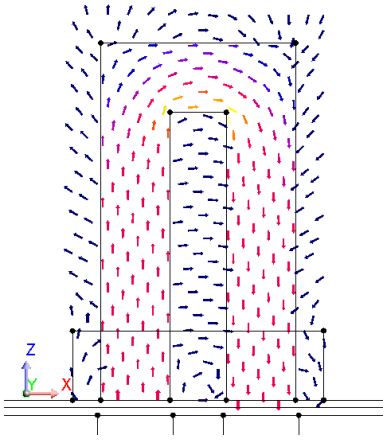

(c) IBTFM with 4 working magnets

Figure 5.6: Flux density in the cross section of the stator stack for (a) BTFM with four working magnets, (b) BTFM with two working magnets, and (c) IBTFM with four working magnets. The arrows in figures show the space distribution of the flux density: the yellow color corresponds to the highest values of the flux density and dark-blue to the lowest values.

The pole-to-pole flux leakage is obtained by comparing the flux linked with the winding $\Phi_{winding}$ in the geometries with four and two working magnets per pole pair. The variation of $\Phi_{winding}$ with the stack and magnet thicknesses in the direction of movement for various pole lengths $\tau_{p,r} = [8, 15]\,\mathrm{mm}$ is depicted in Fig. 5.7(a). The lowest surface in figures correspond to $\tau_{p,r} = 8\,\mathrm{mm}$, while the upper for $\tau_{p,r} = 15\,\mathrm{mm}$.

The flux linkage increases with the magnet size, making these machines more favorable. Although this implies that the number of poles should be reduced if the same machine dimensions are assumed.

Variation of the pole-to-pole flux leakage is shown in Fig. 5.7(e). As the distance between the adjacent magnets gets larger, the flux leakage decreases. This, for example, can be seen in topologies with $l_{m,r} = l_{st,r} = 5\,\mathrm{mm}$ and varying $\tau_{p,r}$, in which the flux leakage between $\tau_{p,r} = 15\,\mathrm{mm}$ and $\tau_{p,r} = 8\,\mathrm{mm}$ is decreased almost threefold.

The maximum flux linked with the winding per volume of the magnet material should be investigated to determine the effectiveness of the magnets being used. As can be seen in Fig. 5.7(c), the usage of shorter magnets and longer poles is recommended to maximize the utilization of the magnet material.

The topology with $\tau_{p,r} = 15\,\mathrm{mm}$, $l_{m,r} = 13\,\mathrm{mm}$ and $l_{st,r} = 8\,\mathrm{mm}$ is found to have the largest flux linkage $\Phi_{winding} = 42.6\,\mu\mathrm{Wb}$ (marked with '$\times$' in Fig. 5.7(b)), and the topology with $\tau_{p,r} = 15\,\mathrm{mm}$, $l_{m,r} = 5\,\mathrm{mm}$ and $l_{st,r} = 7\,\mathrm{mm}$ utilizes permanent magnets at their best with $8.5\,\mathrm{Wb/m^3}$ as can be seen in Fig. 5.7(d). These two sets of dimensions are selected for further studies in the dynamic 3D FEM calculations.

As the electromagnetic torque is directly proportional to the flux linkage, the combinations with the larger magnets should be preferred. However, as far as the utilization of the magnet material is concerned, the combinations with the shortest magnets are of interest. To obtain a reasonable compromise between these two criteria, an optimization procedure is necessary.

Parametric Study of IBTFM

Similar as before analyses are conducted for the TFM with the iron bridges (see Fig. 5.1(b)). The dimensions in the movement plane are varied as previously and the iron bridge thickness is chosen to be equal to the magnet thickness $l_{ib,r} = l_{m,r}$. The dependency of the flux linkage with the dimensions in the direction of movement is shown in Fig. 5.8(a). As the flux produced by the adjacent magnets has less impact on the main magnetic flux, the level of the flux leakage is considerably lower and thus larger values of the flux linkage $\Phi_{winding}$ are achieved. The maxi-

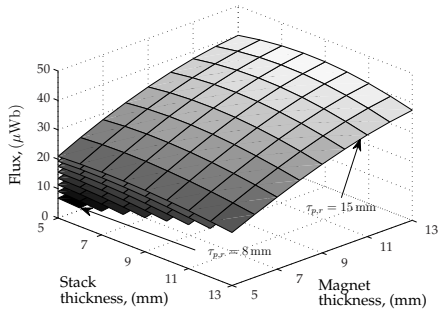

(a) Flux linkage due to magnets acting alone for $\tau_{p,r} = [8, 15]\,\mathrm{mm}$

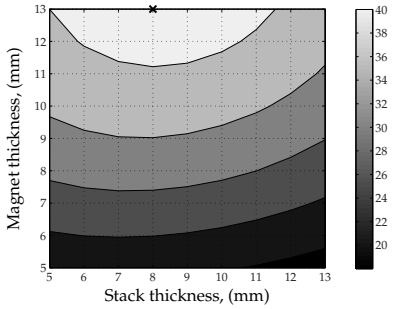

(b) Flux linkage due to magnet acting alone for $\tau_{p,r} = 15\,\mathrm{mm}$

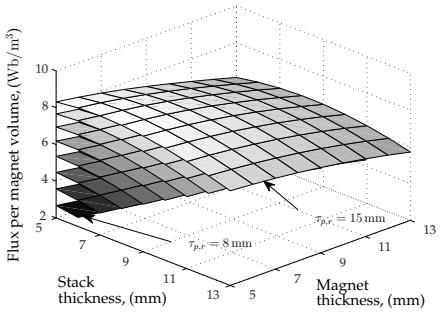

(c) Flux linkage due to magnets acting alone per magnet volume for $\tau_{p,r} = [8, 15]\,\mathrm{mm}$

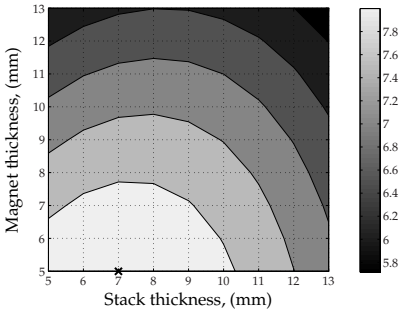

(d) Flux linkage due to magnets acting alone per magnet volume for $\tau_{p,r} = 15\,\mathrm{mm}$

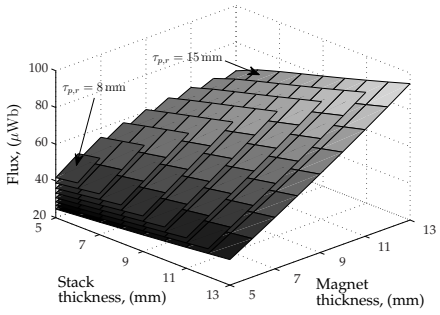

(e) Flux leakage at no-load

Figure 5.7: Results of static 3DFEM simulations of the BTFM at no-load.

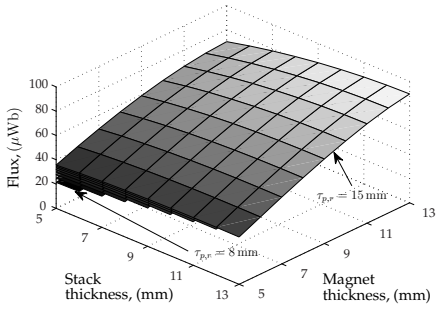

(a) Flux linkage due to magnets acting alone for $\tau_{p,r} = [8, 15]$ mm

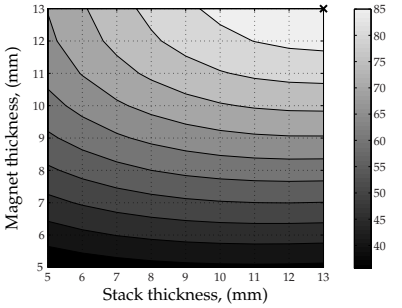

(b) Flux linkage due to magnet acting alone for $\tau_{p,r} = 15$ mm

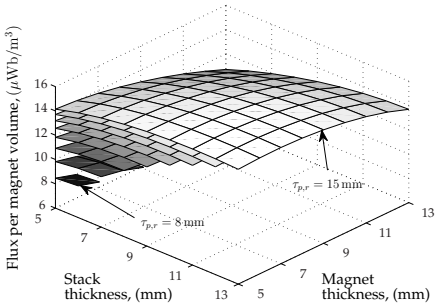

(c) Flux linkage due to magnets acting alone per magnet volume for $\tau_{p,r} = [8, 15]$ mm

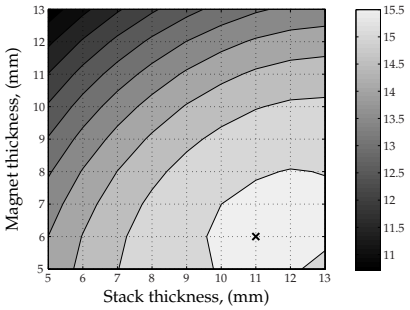

(d) Flux linkage due to magnets acting alone per magnet volume for $\tau_{p,r} = 15$ mm

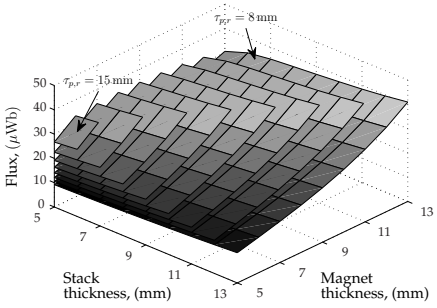

(e) Flux leakage at no-load

Figure 5.8: Results of static 3DFEM simulations of the IBTFM at no-load.

mum value of $\Phi_{winding} = 89.6\,\mu\mathrm{Wb}$ is attained for $\tau_{p,r} = 15\,\mathrm{mm}$, $l_{m,r} = 13\,\mathrm{mm}$ and $l_{st,r} = 13\,\mathrm{mm}$ as shown by the marker in Fig. 5.8(b).

The utilization of the magnet material in the IBTFM is also better than in the BTFM. The topology with $\tau_{p,r} = 15\,\mathrm{mm}$, $l_{m,r} = 6\,\mathrm{mm}$ and $l_{st,r} = 11\,\mathrm{mm}$ has the best utilization of the magnets with $15.6\,\mathrm{Wb/m^3}$ (see Fig. 5.8(d)), which in comparison to the BTFM, is larger by more than 80%.

5.4 Calculation of the Flux Linkage for Varying Airgap Length and Magnet Height

The aim of the study presented in this section is to investigate how the flux linkage at no-load is related to the airgap length in BTFM and IBTFM topologies. In the work presented in [17, 26], the transverse flux generators had a relatively small outer diameter, which allowed to keep the airgap length small (up to 3 mm). However, when designing a generator with a large rated power, the outer diameter and thus the airgap length can get larger. In order to determine this correlation, the two sets of dimensions are analyzed in this study. The machines with the pole lengths of $\tau_{p,r} = 15\,\mathrm{mm}$ and $\tau_{p,r} = 30\,\mathrm{mm}$ and the magnet/stack coverage of 2/3 of the pole length are considered. The airgap length varies in the interval $g = [2, 10]\,\mathrm{mm}$ and the magnet height in the interval $h_m = [2, 15]\,\mathrm{mm}$.

The graphs in Fig. 5.9 illustrate the variation of the flux linkage with the airgap length and magnet height. As can be seen, the flux linkage decreases considerably with the airgap length for the both selected sets of dimensions. This undesired correlation can be explained by the fact that more flux is being leaked between poles, as the attraction of the adjacent magnets becomes larger.

The analytical Eq. 5.1 would suggest that the magnet height can be adjusted in order to keep the same flux density in the stator teeth, i.e.

$$h_m = \frac{\mu_{rpm}\, g}{\frac{B_{rpm}}{\widehat{B}_g} - 1}, \tag{5.1}$$

For example, topology with a 3 mm airgap would require a magnet with the height of $h_m = 8.4\,\mathrm{mm}$ in order to produce the maximum flux density in the airgap $\widehat{B}_g = 0.8\,\mathrm{T}$. Consequently, if the airgap length is to be increased to 5 mm, the magnet height, according to the Eq 5.1, should be increased to $h_m = 14.0\,\mathrm{mm}$. If fringing is disregarded, the flux linked to the winding should be proportional to the airgap flux density $\widehat{B}_g$. However, the flux linkage for this set of dimensions, as calculated in FEM, accounts only for 45% of the analytically expected value, i.e. $36.6\,\mu\mathrm{Wb}$ is expected but only $20.1\,\mu\mathrm{Wb}$ is linked to the winding (see Table 5.4).

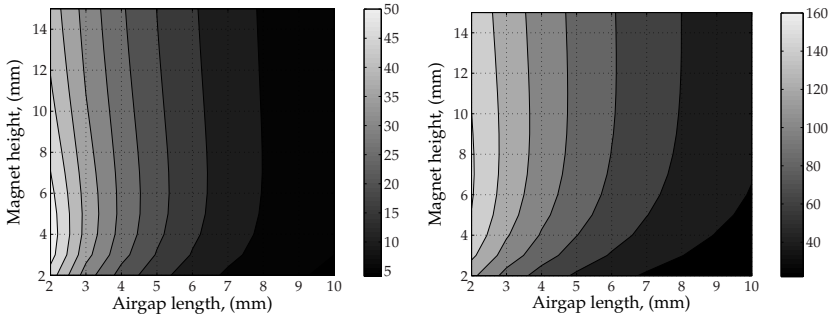

(a) (b)

Figure 5.9: Flux linkage as a function of the airgap length and magnet height for the BTFM topology for (a) $\tau_{p,r} = 15\,\mathrm{mm}$, $l_{m,r} = 10\,\mathrm{mm}$, $l_{st,r} = 10\,\mathrm{mm}$ and (b) $\tau_{p,r} = 30,\ \mathrm{mm}\, l_{m,r} = 20,\ \mathrm{mm}\, l_{st,r} = 20\,\mathrm{mm}$.

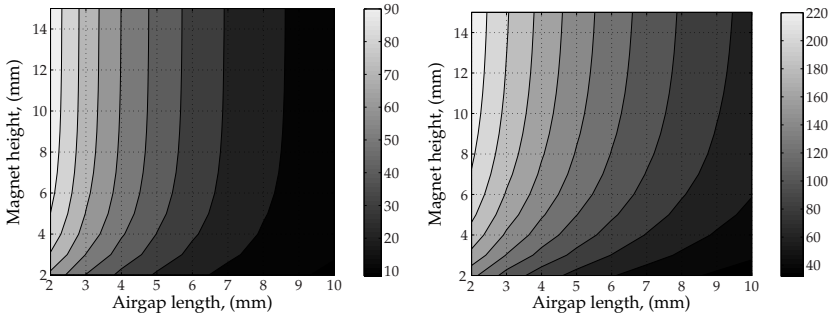

(a) (b)

Figure 5.10: Flux linkage as a function of the airgap length and magnet height for the IBTFM topology for (a) $\tau_{p,r} = 15\,\mathrm{mm}$, $l_{m,r} = 10\,\mathrm{mm}$, $l_{st,r} = 10\,\mathrm{mm}$ and (b) $\tau_{p,r} = 30,\ \mathrm{mm}\, l_{m,r} = 20,\ \mathrm{mm}\, l_{st,r} = 20\,\mathrm{mm}$.

The rate of the flux linkage somewhat improves with the increased pole length, as can be seen in Fig. 5.9(b) and summarized in Table 5.4. For the topology with a 5 mm airgap and a 14 mm magnet, the flux linked to the winding is $95.2\,\mu\mathrm{Wb}$, which is still around 29% lower than could be expected by applying Eq. 5.1.

The variation of the flux linkage in the machines employing IBTFM topology is illustrated in Fig. 5.10. The same sets of dimensions as in the BTFM topology are selected, i.e. $g/h_m = 3/8.4$ and $g/h_m = 5/14$ as shown in Table 5.4. The

Table 5.4: Influence of the airgap length and the magnet height on the flux linkage.

Model	$\tau_{p,r}\,(\mathrm{mm})$	$g\,(\mathrm{mm})$	$h_m\,(\mathrm{mm})$	$\widehat{\Phi}_m\,(\mu\mathrm{Wb})$
BTFM	15.0	3.0	8.4	36.6
	15.0	5.0	14.0	20.1
	30.0	3.0	8.4	134.1
	30.0	5.0	14.0	95.2
IBTFM	15.0	3.0	8.4	74.6
	15.0	5.0	14.0	47.0
	30.0	3.0	8.4	189.3
	30.0	5.0	14.0	149.9

comparison of the results shows that although the flux linkage is decreasing with the larger airgap length, its value is still higher than in the machines with the basic topology. For example, in the topology with $\tau_{p,r} = 15\,\mathrm{mm}$ and $g/h_m = 5/14\,\mathrm{mm}$ the pole-to-pole flux leakage accounts for 37%. With the increasing pole length, the portion of the flux linked to the winding improves even further, where as much as $150.0\,\mu\mathrm{Wb}$ or 79% of the flux expected from Eq. 5.1 can be linked to the winding.

The flux linkages calculated in this section are used to assess the electromagnetic force production in the machines with the varying airgap length in the following chapter.

5.5 Dynamic Modeling in FEM

Thus far, the transverse flux topologies were examined at one instant of time, at which the stack was aligned with the magnets. The static analysis can provide some quantitative understanding of how the generator performance is interconnected with the physical dimensions of the magnetic core. However, as far as the induced voltage and its harmonic content are concerned, the variation with time (or angular displacement) becomes of great importance; hence, the dynamic simulations are necessary.

In addition to the general considerations made while modeling TFM in the static 3DFEM, the following two are made for the dynamic studies:

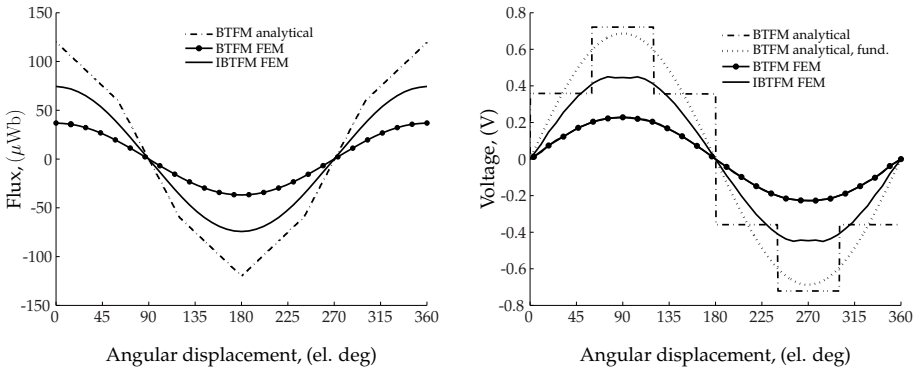

(a) Flux linkage due to magnets acting alone

(b) Induced emf

Figure 5.11: Comparison of the flux linkage due to magnets acting alone (a) and induced emf (b) as a function of the angular displacement in the analytical and FEM calculations.

- A linear motion is considered throughout the simulation. This assumption is valid for machines with large diameters, which is the case in this study.
- The simulations are performed for a full electric period with 50 steps.

Comparison with the Analytical Results

This section provides a comparison between the analytical and dynamic 3D FEM calculations at no-load condition. The variation of the flux linkage with the rotor position is illustrated in Fig. 5.11(a).

The flux linkages obtained earlier in the static FEM simulations in the d-direction are virtually the same as the magnitudes of the flux linkages calculated in the dynamic analysis[1]. The difference in the magnitudes of the two analyzed topologies was discussed earlier. However, the sinusoidal shape of the flux differs from the triangular of the analytically predicted one. The flux waveform owes its sinusoidal shape to the stray fluxes from the adjacent magnets, which smoothen the triangular waveform obtained when the pole-to-pole flux leakage is neglected.

The induced emf per pole pair obtained from the FEM simulations is illustrated in Fig. 5.11(b). Unlike the square-shaped waveform of the analytically determined emf, the FEM-calculated emfs vary sinusoidally. The analytically calculated rms value of the fundamental component is 0.49 V. Only a third of this emf, i.e. 0.16

[1] A minor discrepancy of less than 1% was encountered due to a less dense mesh used in the dynamic models. The less dense mesh was necessary to reduce the computation time.

V, is induced in the BTFM. This value is larger in the IBTFM with the iron bridge – 0.32 V, yet it accounts only for two thirds of the analytically determined value. The emf reduction follows the reduction of the flux linked with the winding (see Fig. 5.11(a)).

As can be observed in Fig. 5.11(b), the emf in the IBTFM flattens at the position when the stack is located between the magnets, i.e. around $90°$. This can be explained by analyzing the flux linkage variation in Fig. 5.11(a). As the flux linkage varies with the nearly constant slope at this position, the top of the emf curve flattens following Faraday's law:

$$e(t) = -n_s \frac{\mathrm{d}\phi_{winding}(t)}{\mathrm{d}t}, \tag{5.2}$$

where n_s is the number of conductors per slot.

Influence of Dimensions in the Direction of Movement

In the static analysis, the magnitude of the flux linked with the winding was determined with respect to the dimensions varying in the direction of movement. To extend this study in time, dynamic simulations are performed for the topologies with the largest flux linkage or the best utilization of the magnet material.

The variation of the flux linked with the winding and the induced emf for the selected sets of dimensions with angular displacement are calculated and the results are presented in Fig. 5.12. The magnitudes of the flux linkages in Fig. 5.12(a) differ from their fundamentals at most by 2% for IBTFM and around 0.5% for BTFM, while other components are insignificant (around 2.5% for the third harmonic in the IBTFM topology). This makes static FEM simulations sufficient if only the flux linkage is of concern. The flux linkage of the IBTFM with $l_{m,r} = l_{st,r} = 13\,\mathrm{mm}$, however, has a linear sector between approximately $70° - 110°$. This linear variation of the flux linkage following Eq. 5.2 results in the flattening of the induced voltage as shown in Fig. 5.12(c).

The amplitudes of the first five harmonics for the four selected topologies are shown in Fig. 5.12(d). The fundamental harmonics are clearly the dominating components here. The presence of other components is limited in the BTFM and more pronounced in the IBTFM. The amplitude of the third harmonic in the IBTFM is the largest one, at about 6-7% of the fundamental.

Although the static simulations can give a good estimation of the flux linkage magnitude, the use of Eq. 5.2 for calculation of the induced emf is insufficient and thus dynamic simulations are required to obtain the correct waveforms.

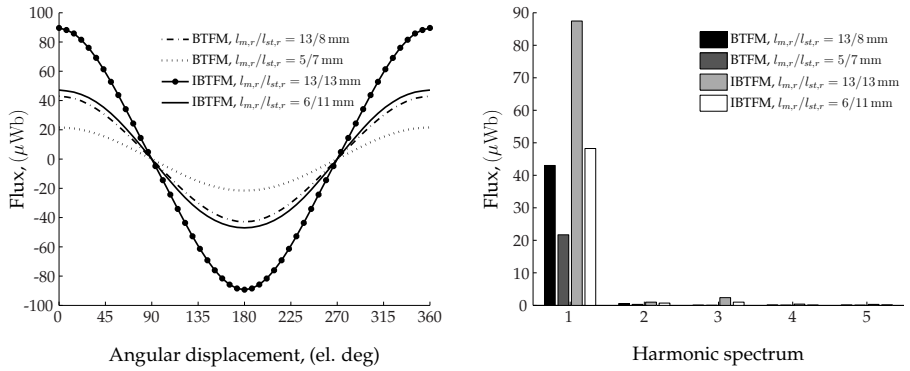

(a) Flux linkage due to magnets acting alone

(b) Harmonic content of the flux linkage

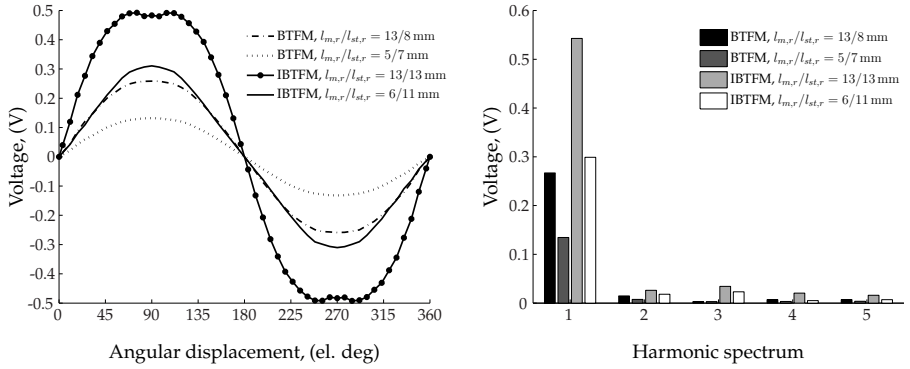

(c) Induced emf

(d) Harmonic content of the induced emf

Figure 5.12: Variation of the flux linkage and induced emf with the angular displacement and their harmonic content for the four selected sets of dimensions.

5.6 Measurements at No-load

In order to verify the results of the finite element analyses at no-load, measurements of the linear synchronous machine with the basic transverse flux topology have been performed. The machine has been manufactured at the Department of Electrical Machines and Power Electronics, Royal Institute of Technology, as a part of the doctoral thesis work presented in [36]. The description of the machine and its overview can be found in Chapter 4 of this work.

The tested machine had 16 poles and 12 stator slots with the three-phase winding placed inside. To be able to compare the finite element model with the measurements, the same set of dimensions is adopted in the model analyzed in the

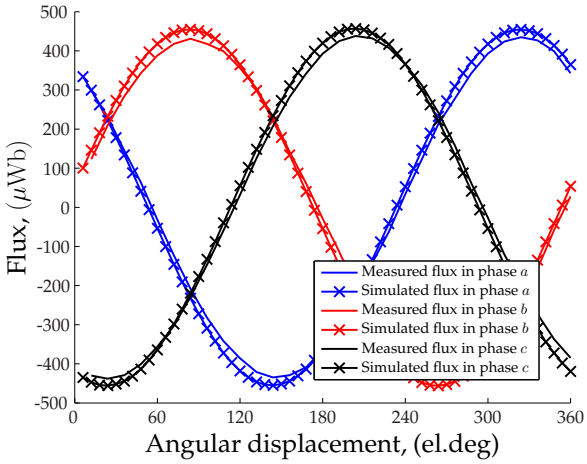

Figure 5.13: Comparison of the flux linkage obtained in the FEM simulations and by measurements.

finite element software.

The measurements at no-load condition aim to compare the flux linkage, induced emf and cogging force with the FEM simulations.

Flux Linkage

The flux linkage is one of most important figures of merit when estimating the machine performance. The force production is proportional to the flux linkage. To measure the flux linkage in the tested machine, a flux meter has been used. It consists of the coils mounted around the stator yoke. Later, the induced emf measured in the coils is integrated in order to obtain the flux linkage.

The comparison of the results is presented in Fig. 5.13. The measured flux linkage in different phases is compared with the corresponding results from the finite element simulations. As can be seen both the shape and the amplitude of the curves correspond well.

No-load Emf

The induced emf is obtained through differentiation of the flux linkage with time. As the results in the previous section had a good agreement, the induced emf obtained in FEM and through the measurements would also correspond well with each other. This comparison of emfs for one phase is depicted in Fig. 5.14.

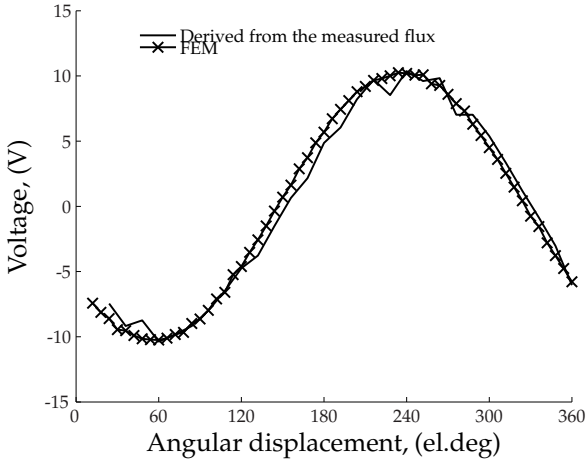

Figure 5.14: Comparison of the induced emf obtained in FEM and measured.

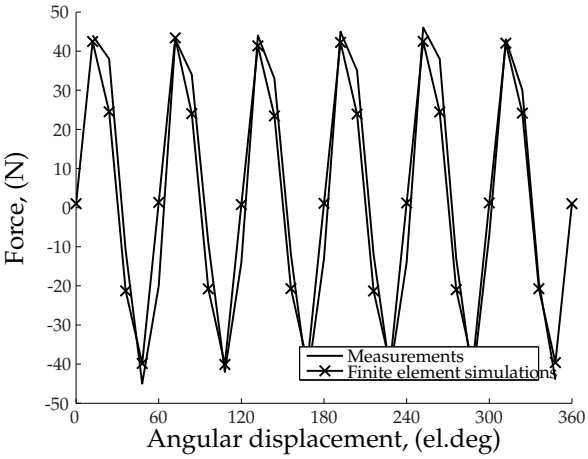

Figure 5.15: Comparison of the cogging force obtained in FEM and through measurements.

Cogging Force

The variation of the cogging force with the mover position is shown in Fig. 5.15. The simulations were performed with no armature current injected in the winding. The position of the mover varies with time, while the force is measured with the force meter Burster Compression Load Cell 2 KN that has precision of 0.5%.

The force measurements are performed for the three-phase machine. As can be

seen in Fig. 5.15, the results of the measurements agree well with those obtained in FEM.

A more detailed explanation of the measurements at no-load, as well as the measurements of the loaded machine, can be found in [36].

5.7 Conclusions

The finite element static and dynamic analyses of a direct-driven generator employing a basic transverse flux topology and that utilizing iron bridges have been presented in this chapter. At first, the topologies with the initial dimensions were studied. As the selection of the pole length in the transverse flux machines affects the pole-to-pole flux leakage and thus its performance, the topologies have been analyzed with respect to the varying dimensions in the direction of movement.

The topologies utilizing IBTFM have been found to be superior to the BTFM with respect to the flux linkage (by 110%) and magnet utilization (by 84%). The machines with the longest magnets gave the largest flux linkage, while machines with the short magnets should be preferred for better magnet utilization. Four sets of dimensions have been selected for a dynamic finite element analysis.

Unlike the triangular waveform of the analytically calculated flux linkages, the flux linkages obtained in FEM have been found to vary almost sinusoidally with time, which is due to the flux leakage between the adjacent magnets. A difference of up to 2% between the magnitude of the flux linkage from the static FEM analysis and its fundamental component from the dynamic simulations has been found, which shows the static simulations to be sufficient for an approximate analysis. The variation of emfs proved to be less sinusoidal, especially in the IBTFM, with the third harmonic prevailing.

The measurements of the linear prototype at no-load have been performed and the results were compared with the finite element simulations. The flux linkage, induced voltage and the cogging torque had a good agreement with each other.

As the transverse flux machine consists of a number of identical units, the studies that have been conducted in this chapter can be applied for generators with different shapes, such as toroidal, cylindrical, etc (see Chapter 7).

Chapter 6

3DFEM Analysis at Load

The calculation of the power factor and the electromagnetic force of a transverse flux generator with the use of three-dimensional finite element analysis is presented in this chapter. First, the analysis is performed for two different single-phase transverse flux topologies. The influence of the dimensions in the peripheral plane on the force production and power factor is estimated. The power factor is calculated by three different methods and the results are compared. An alternative way to estimate the electromagnetic force based on the static simulations is described.

6.1 Power Factor Calculation

Power factor (PF) is an important figure of merit of any electrical machine. The value of PF determines the size of power electronic components, transformers and transmitting equipment as their rating is given in volt-amperes (VA) rather than in watts (W). In this way, the cost of the entire system is largely affected by the value of the power factor. The following analysis is conducted in order to investigate the variation of power factor in the studied transverse flux topologies with varying dimensions.

To estimate the power factor of the transverse flux generator analyzed in this work, the classical electric circuit model of a synchronous generator shown in Fig. 6.1(a) is considered. The winding resistance is R_a and the armature inductance consisting of magnetization and leakage inductances is denoted by L_a; the back emf is E_f and the terminal voltage is V_t.

As the magnetization of PM machines cannot be decreased at reduced loads (unless flux weakening is applied), the induced emf E_f is constant and equal to its

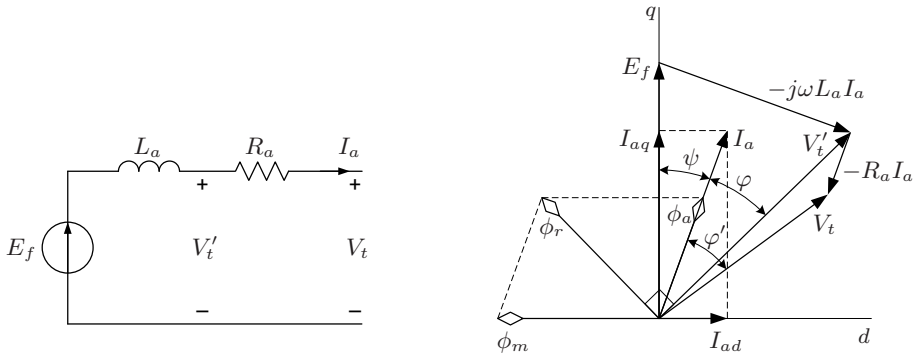

(a) Single-phase equivalent circuit (b) Phasor diagram

Figure 6.1: Single-phase transverse flux topologies with permanent magnet excitation.

no-load value. By selecting the magnitude of the armature current and the current angle as shown in Fig. 6.1(b), the terminal voltage V_t can be controlled.

Three different phasor diagrams that could be applied for the control of the generator are presented in Fig. 6.2 [17, 26]. For all three modes, the forced-commutated converter is required for the grid connection of the generator [26]. The back-to-back converter depicted in Fig. 6.3 is suggested for the wind turbine applications [4]. It consists of a rectifier and an inverter with an intermediate dc-link capacitor.

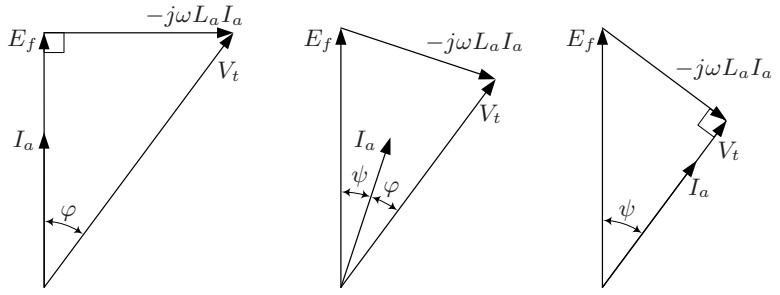

(a) (b) (c)

Figure 6.2: The single-phase equivalent circuit of the generator when (a) $\psi = 0$, (b) $\phi = \psi$ and (c) $\phi = 0$.

The first control mode in Fig. 6.2(a) corresponds to the case when the load

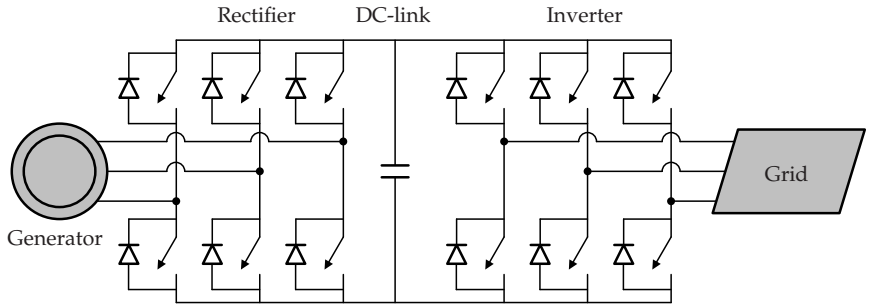

Figure 6.3: Back-to-back frequency converter.

angle $\psi = 0$, and thus terminal voltage V_t is higher than the induced emf E_f. The power factor is low in this case, which results in increased converter rating and total system cost.

In Fig. 6.2(b), a compromise control mode is presented, where the phase current is placed between the induced emf and the terminal voltage. The load angle ψ and the phase angle φ are equal in this case and $E_f \approx V_t$. This control mode could help to find out a reasonable compromise between the generator rating and converter rating.

The control mode employing the phasor diagram shown in Fig. 6.2(c) has the current in phase with the terminal voltage, thus $\varphi = 0$. Unity power factor has an advantage of the reduced converter rating.

The control mode presented in Fig. 6.2(a) has been adopted in the analyzed generators. Although the selection of a control mode will inevitably affect the electromagnetic design, this mode has deliberately been selected to be able to estimate the feasibility of the transverse flux concept.

FEM Models for Power Factor Calculation

The three following FEM models are analyzed while estimating the power factor in the TFM:

- No-load model, where the armature current is turned off and the flux linkage $\psi_m(t)$ is due to the magnet flux acting alone. In this model, the induced emf $e_f(t)$ can be calculated through derivation of the flux linkage $\psi_m(t)$ with time, i.e.

$$e_f(t) = -\frac{\mathrm{d}\psi_m(t)}{\mathrm{d}t}. \tag{6.1}$$

- Magnets are turned off and the flux linkage $\psi_a(t)$ is due to the sinusoidal armature current acting alone. The reactive voltage drop $(X_a I_a)$ can be found by differentiating the armature flux linkage with respect to time.

$$(X_a I_a) = -\frac{\mathrm{d}\psi_a(t)}{\mathrm{d}t} \tag{6.2}$$

  The armature inductance L_a can consequently found as

$$L_a = -\frac{\mathrm{d}\psi_a(t)}{\mathrm{d}t}\frac{1}{2\pi f_e I_a}. \tag{6.3}$$

- Load model in which the flux linkage $\psi_r(t)$ is due to the interaction of the magnet flux and the flux due to armature current. The terminal voltage $v_t(t)$ is thus given by:

$$v_t = e_f(t) + \omega L_a i_a(t) + R_a i_a(t) \approx -\frac{\mathrm{d}\psi_r(t)}{\mathrm{d}t}. \tag{6.4}$$

Power Factor Calculations in the TFM with the Initial Geometry

Power factor in TFM machines can be calculated by a number of methods when conducting the three-dimensional finite element analysis. The three following approaches are treated in this section:

1. The straightforward approach consists in determining the phase shift φ between the armature current I_a and the terminal voltage V_t (or, alternatively, between the flux from the magnets ϕ_m and resultant flux ϕ_r if the armature resistance is negligible) in the dynamic simulations with the rated sinusoidal current flowing in the winding. For this purpose, the circuit depicted in Fig. 6.1(a) is used.

   Fig. 6.4(a) and Fig. 6.5(a) show variations of the induced emf, the reactive voltage drop, and the terminal voltage with respect to the angular displacement of the rotor in the BTFM and IBTFM. To calculate the power factor, the phase shift between the fundamental components of the terminal voltage and the current should be determined, i.e. angle φ as illustrated by Fig. 6.4(b) and 6.5(b). For the selected cases the PF are the following: 0.52 for the BTFM and 0.47 for the IBTFM topologies.

2. The second approach is based on the dynamic calculations, where the amplitudes of the values of the internal voltage drop and the emf are used to estimate the PF according to Eq. 6.5. As the phase current I_a is chosen to be in phase with the induced emf E_f, i.e. current is in the q-axis direction,

and assuming the sinusoidal distribution of currents and voltages, the power factor can be calculated as follows:

$$\mathrm{PF} = \cos\varphi = \frac{E_f - R_a I_a}{V_t}. \tag{6.5}$$

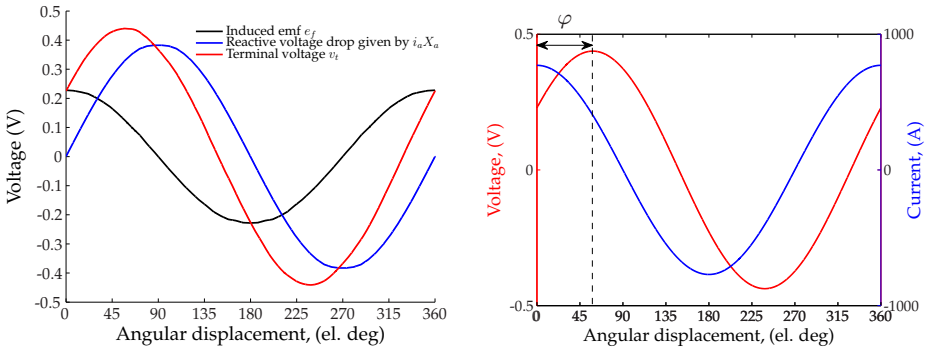

(a) (b)

Figure 6.4: (a) Variation of the induced emf, reactive voltage drop and terminal voltage with the angular displacement and (b) phase shift between the terminal voltage and the armature current in the BTFM topology.

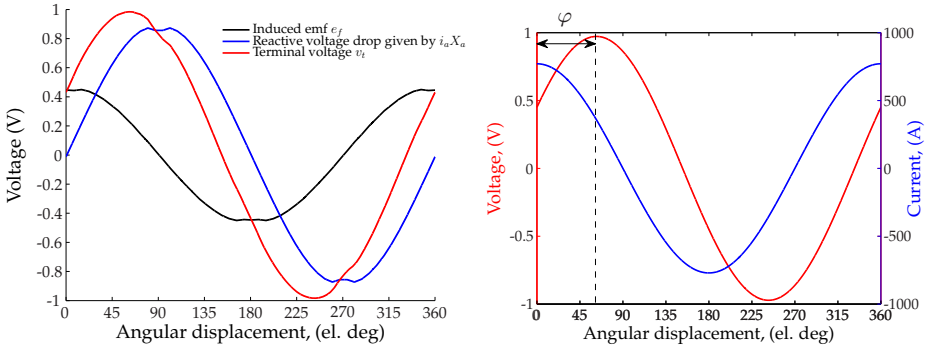

(a) BTFM (b) IBTFM

Figure 6.5: (a) Variation of the induced emf, reactive voltage drop and terminal voltage with the angular displacement and (b) phase shift between the terminal voltage and the armature current in the IBTFM topology.

By computing the fundamental components of the induced emf and the terminal voltage, the power factor in the TFM with the initial geometry has been obtained, as 0.50 in the BTFM and 0.46 in the IBTFM.

3. Unlike the previous two approaches, the third method uses the flux linkages to calculate the power factor in the TFM machines. If the winding resistance R_a is very small (which is often the case in large synchronous machines), the terminal voltage is nearly the same as the internal voltage $V_t \approx V_t'$ and thus the power factor can be obtained from Eq. 6.6 and Eq. 6.7:

$$\text{PF} = \cos\varphi = \frac{E_f}{V_t} = \frac{\mathrm{d}\widehat{\phi}_m}{\mathrm{d}t}\frac{\mathrm{d}t}{\mathrm{d}\widehat{\phi}_r} = \frac{\widehat{\phi}_m}{\widehat{\phi}_r} \tag{6.6}$$

$$= \cos\left[\tan^{-1}\left(\frac{\widehat{\phi}_a}{\widehat{\phi}_m}\right)\right]. \tag{6.7}$$

Eq. 6.7 is however valid only if the fluxes vary sinusoidally with time and the magnetic core of en electrical machine is not saturated at load condition [49]. If the opposite is true, Eq. 6.6 should be used instead.

At first, the power factor is estimated with the use of static analysis performed in the finite element software FLUX 3D using Eq. 6.7.

The results of the static simulations are summarized in Table 6.1. It seen that the flux due to the armature current acting alone results in a flux linkage larger than that due to magnets. However, to obtain a machine with a high PF (e.g. larger than 0.90), the quotient should be below 0.5 as can be understood from Eq. 6.7. Although the flux linkages obtained in the IBTFM for the same amount of the magnet material are almost twice as high as in the BTFM, the power factor is larger in the machine with the basic topology (see Table 6.1).

Table 6.1: Power factor calculation in the static FEM analysis

Topology	$\widehat{\phi}_m$, (μWb)	$\widehat{\phi}_a$, (μWb)	PF
Basic TFM	36.6	60.1	0.52
TFM with iron bridges	74.6	140.8	0.47

To complement the static analysis, 3D FEM dynamic simulations have been performed for the studied topologies, where the power factor is calculated

according to Eqs. 6.6 and 6.7. The results for the BTFM and IBTFM with the initial geometry are shown in Fig. 6.6(a) and Fig. 6.6(b), respectively. The magnitudes of the flux linkages obtained in the static simulations are shown for convenience with markers.

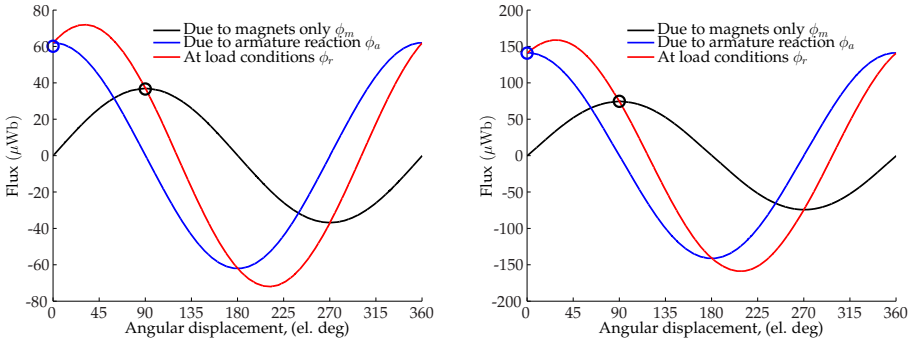

(a) BTFM (b) IBTFM

Figure 6.6: Flux variation with the angular displacement in (a) BTFM and (b) IBTFM topologies.

As can be seen, the flux linkage varies sinusoidally with time in all three modes for both studied topologies. The magnitudes obtained in the static simulations agree well with the dynamic simulations. These results show almost the same PF independent of the way it is calculated, as summarized in Table 6.2. The magnetic core showed no presence of saturation in either of the topologies.

Table 6.2: Power factor calculation by different methods

Topology	Static (6.7)	Dynamic (6.6)	Dynamic (6.7)
Basic TFM	0.52	0.50	0.51
TFM with iron bridges	0.47	0.46	0.47

Influence of the Dimensions in the Direction of Movement on the Power Factor

The power factor and its value per volume of magnet material (PF/V_{pm}) are calculated for the following dimensions:

Pole pitch $\tau_{p,r} = [8, 15]\,\mathrm{mm}$.

Magnet thickness $l_{m,r} = [5, (\tau_{p,r} - 2)]\,\mathrm{mm}$.

Stack thickness $l_{st,r} = [5, (\tau_{p,r} - 2)]\,\mathrm{mm}$.

Iron bridges $l_{ib,r} = l_{m,r}$.

The variation of the power factor with the dimensions in the peripheral plane is calculated with the use of static FEM analysis. The variation of PF with the stack and magnet thicknesses for various pole lengths $\tau_{p,r} = [8, 15]\,\mathrm{mm}$ is depicted in Fig. 6.7(a). The lowest surface in figure corresponds to $\tau_{p,r} = 8\,\mathrm{mm}$, while the upper shows variation of the power factor for $\tau_{p,r} = 15\,\mathrm{mm}$. The variation of the power factor for $\tau_{p,r} = 15\,\mathrm{mm}$ is also presented in Fig. 6.7(b). The highest values of the PF are attained for topologies with the longest pole and magnet, and shortest stack. The BTFM topology with $\tau_{p,r} = 15\,\mathrm{mm}$, $l_{m,r} = 13\,\mathrm{mm}$ and $l_{st,r} = 5\,\mathrm{mm}$ has PF = 0.62 (depicted with marker in Fig. 6.7(b)).

The ratio of PF per magnet volume is of interest when estimating the effectiveness of the magnet material used in the machine with respect to the power factor (see Fig. 6.7(c)). Although the topology with $\tau_{p,r} = 15\,\mathrm{mm}$, $l_{m,r} = 5\,\mathrm{mm}$ and $l_{st,r} = 5\,\mathrm{mm}$ has the highest magnet utilization with respect to the power factor ($153\,400\,\mathrm{m}^{-3}$), as shown by the marker in Fig. 6.7(d), the power factor in this machine is low, at 0.39.

These two topologies are selected for the further studies in the dynamic 3D FEM analysis.

A similar analysis is performed for the IBTFM topology. The results are depicted in Fig. 6.8. The same dimensions as in the BTFM give the best power factor 0.57 and magnet utilization of $144\,700\,\mathrm{m}^{-3}$ (with PF = 0.36).

Power Factor Calculations with Dynamic 3D FEM Analysis

The four topologies selected during the parametric study are analyzed further with the aid of time-dependent 3D FEM simulations. Power factors obtained from Eqs. 6.6 and 6.7 as well as the results of the static simulations are tabulated in Table 6.3. The results have a good agreement independent of the method applied for the BTFM topology (machine 1 and 2) and machine 4 with the IBTFM topology.

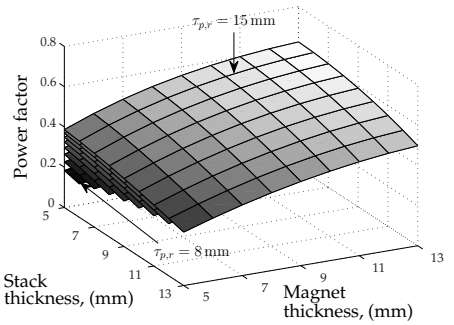

(a) Power factor for $\tau_{p,r} = [8, 15]\,\mathrm{mm}$

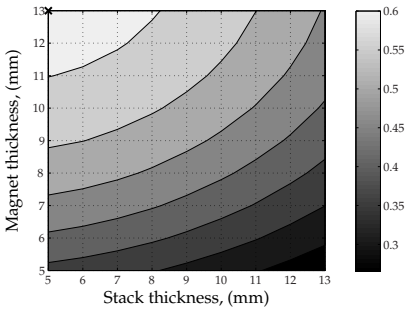

(b) Power factor for $\tau_{p,r} = 15\,\mathrm{mm}$

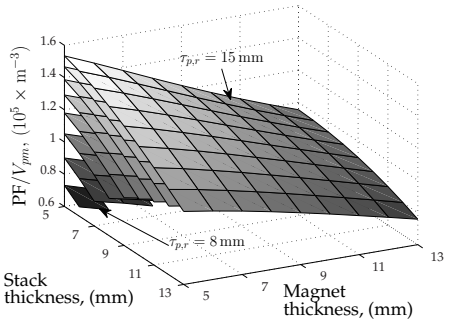

(c) Power factor per magnet volume for $\tau_{p,r} = [8, 15]\,\mathrm{mm}$

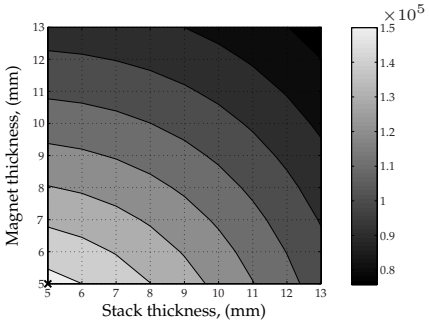

(d) Power factor per magnet volume for $\tau_{p,r} = 15\,\mathrm{mm}$

Figure 6.7: Power factor and its value per magnet volume in the BTFM topology.

The difference becomes significant in machine 3, where the power factor differs by as much as 10% depending on the calculation method used.

To analyze this machine in more detail the variation of the flux linkages with time is depicted in Fig. 6.9. As can be seen, the magnitudes of the flux linkages due to magnet $\widehat{\phi}_m$ and armature current $\widehat{\phi}_a$ acting alone obtained in the static simulations shown by markers in the figure correspond well with the dynamic simulations. The sum of $\widehat{\phi}_m$ and $\widehat{\phi}_a$ should give the resulting flux linkage at load conditions $\widehat{\phi}_r$. This is however not the case in this topology, as $\widehat{\phi}_r$ is reduced due to saturation of the stator core.

Due to a lower pole-to-pole flux leakage in the IBTFM as compared to the BTFM, the total flux linkage can attain higher values in this topology [50]. Thus, for the same dimensions of the stator stack (machines 1 and 3 in Table 6.3), the

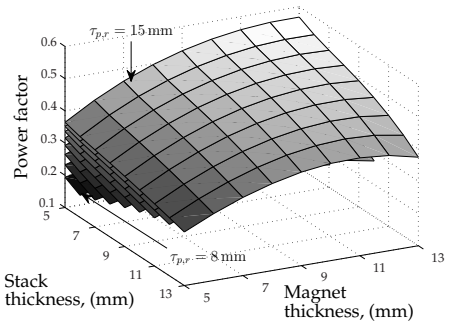

(a) Power factor for $\tau_{p,r} = [8, 15]\,\mathrm{mm}$

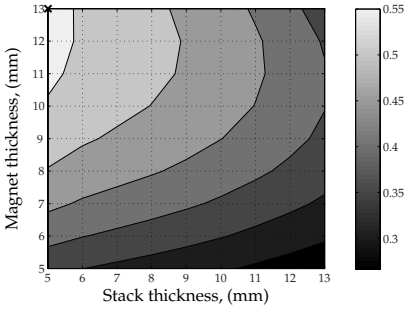

(b) Pore factor for $\tau_{p,r} = 15\,\mathrm{mm}$

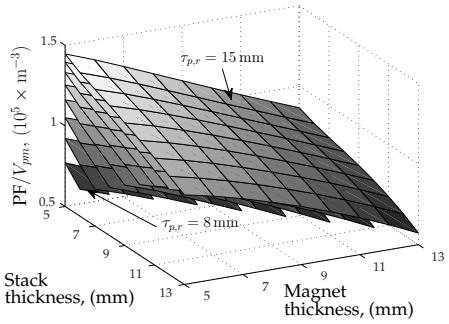

(c) Power factor per magnet volume for $\tau_{p,r} = [8, 15]\,\mathrm{mm}$

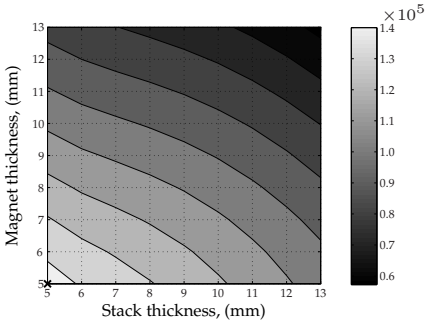

(d) Power factor per magnet volume for $\tau_{p,r} = 15\,\mathrm{mm}$

Figure 6.8: Power factor and its value per magnet volume in the IBTFM topology.

iron core carries more flux and can therefore be saturated. Consequently, the use of Eq. 6.7 should thus be limited to topologies with no or little saturation, while Eq. 6.6 can be used in all the topologies.

As a result of the reduced flux linkage at load condition in the saturated machines, the power factor could be erroneous when calculated by Eq. 6.7. The performed parametric study can still be used to obtain the set of dimensions that gives the largest power factor, yet the value of PF should be verified by Eq. 6.6 in the dynamic simulations.

Table 6.3: Power factor calculation for four topologies using different methods

#	Topology	Static (6.7)	Dynamic (6.6)	Dynamic (6.7)
1	BTFM, $\mathrm{PF}_{\max}$	0.62	0.60	0.62
2	BTFM, $(\mathrm{PF}/V_{pm})_{\max}$	0.39	0.37	0.38
3	IBTFM, $\mathrm{PF}_{\max}$	0.57	0.63	0.57
4	IBTFM, $(\mathrm{PF}/V_{pm})_{\max}$	0.36	0.37	0.36

6.2 Electromagnetic Force

Another important characteristic of any electrical machine is the electromagnetic torque and its time variation, i.e. force ripple. As the linear motion is considered throughout the study, the word 'force' is used in this section. The three following sources of force in a permanent magnet machine are generally recognized [51], [52]:

- Alignment (or mutual) force is the prevailing source of the electromagnetic force in surface-mounted PM machines. It is derived from the interaction of the stator mmf produced by the armature current and the rotor magnetic field.
- Reluctance force is produced as a result of the interaction between the stator

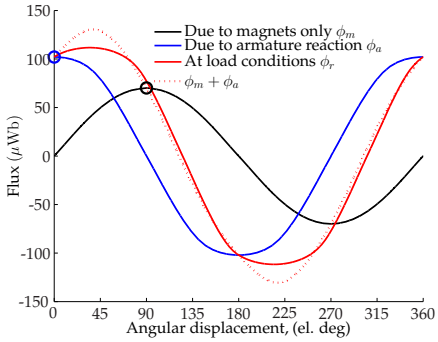

Figure 6.9: Flux linkage variation with the angular displacement in the IBTFM with $\tau_{p,r} = 15\,\mathrm{mm}$, $l_{m,r} = 13\,\mathrm{mm}$ and $l_{st,r} = 5\,\mathrm{mm}$.

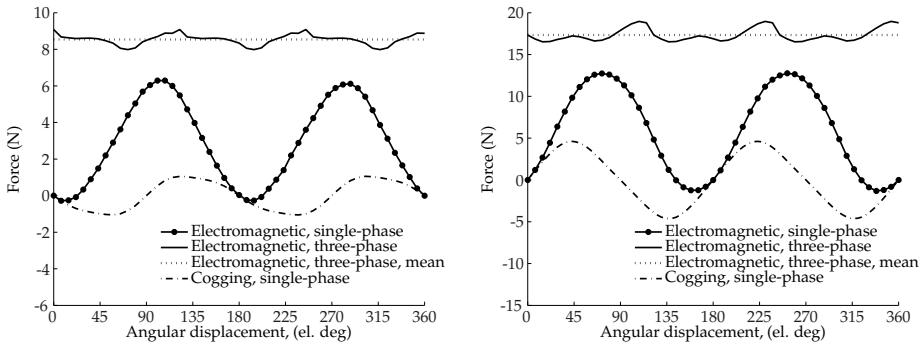

(a) BTFM (b) IBTFM

Figure 6.10: Torque variation with time.

magnetic field and variation of the rotor magnetic reluctance. Reluctance force is normally insignificant in surface mounted PM machines, but it is one of the main sources of force in, for example, PM machines with embedded magnets.

- Cogging force is produced due to the interaction of the rotor magnetic field and variation in the stator reactance as a result of slotting.

To be able to calculate these forces in FEM, the studied topologies should be analyzed at no-load to obtain the cogging force and load condition for the electromagnetic force calculation.

Force Calculation in Machines with the Initial Geometry

At first the BTFM and IBTFM topologies with the initial geometries are investigated. The single-phase electromagnetic and cogging forces calculated with the aid of 3D FEM are depicted in Fig. 6.10(a) and Fig. 6.10(b). The resultant three-phase electromagnetic forces and their mean values obtained by adding three times single-phase forces and taking into account the phase shift between them are shown as well.

Due to cogging, the instantaneous value of the single-phase electromagnetic force can be negative. The effect of cogging can be however significantly reduced in the three-phase machine, where the force ripple is in the range of a few per cent of the electromagnetic force.

By comparing the force production in the two topologies with the initial dimensions, it can be observed that: (a) the mean value of the three-phase electro-

magnetic force is twice as much in the IBTFM (17.3 N) as in the BTFM (8.5 N); (b) the magnitude of the single-phase cogging force is lower in the BTFM (1.1 N) as compared to the IBTFM (4.6 N); (c) both cogging and electromagnetic forces in a single-phase model have a frequency equal to twice the electrical frequency.

From the force production point of view the IBTFM is superior to the BTFM, as for the same outer dimensions and magnet material, the force is higher in the TFM utilizing iron bridges.

Force Calculation in Topologies with Varying Dimensions in the Direction of Movement

The electromagnetic force in an electrical machine can be obtained with the aid of time-dependent finite element analysis at load condition, i.e. when the nominal armature current is injected in the winding. These calculations can however become rather time consuming, especially when conducting 3D FEM, as the analysis should be performed with a small time-step. For example, 50 steps per electrical period were used in the conducted studies. The simulations complexity can increase even further if the magnetic core is saturated as the problem then becomes truly non-linear. To simplify the analysis, the following method to evaluate the force in machines with the different sets of dimensions is proposed.

The fundamental of the magnetic flux is given by

$$\phi_{mf1} = \widehat{\Phi}_{mf1} \sin(\omega_e t), \tag{6.8}$$

where Φ_{mf1} is the value of the flux linkage due to magnets acting alone and $\omega_e = 2\pi f_e$ is the angular velocity (electrical) with the electrical frequency f_e.

The instantaneous value of the emf induced at no-load is

$$e_f = \frac{p}{2} n_s \frac{\mathrm{d}\,\phi_{mf1}}{\mathrm{d}\,t} = \frac{p}{2} n_s \omega_e \widehat{\Phi}_{mf1} \cos(\omega_e t). \tag{6.9}$$

The rms value of the emf is therefore,

$$E_f = \frac{p n_s \omega_e \widehat{\Phi}_{mf1}}{2\sqrt{2}}. \tag{6.10}$$

The mechanical power of the generator is given by

$$P_m = F_{em} v_m = 3 E_f I_a \cos\psi, \tag{6.11}$$

where F_{em} is the electromagnetic force, ψ is the angle between the armature current I_a and emf E_f, and v_m is the mechanical angular velocity which is defined as

$$v_m = \frac{L_m}{p/2} f_e, \tag{6.12}$$

where L_m is the axial length of the machine.

By combining Eq. 6.10 and Eq. 6.11, the electromagnetic force can be derived as

$$F_{em} = \frac{3}{4\sqrt{2}} \frac{2\pi}{L_m} p^2 n_s \widehat{\Phi}_{mf1} I_a \cos\psi. \tag{6.13}$$

Eq. 6.13 can be rewritten for the electromagnetic torque T_{em} in the following form:

$$T_{em} = \frac{3}{4\sqrt{2}} p^2 n_s \widehat{\Phi}_{mf1} I_a \cos\psi. \tag{6.14}$$

Influence of the Airgap and Magnet length on Force Production

By observing Eq. 6.13, it can be noticed that the force production in transverse flux machines is proportional to the square of the pole number. As a consequence, it can be erroneously assumed that the force in the TFM can be quadrupled by simply halving the pole length, which would lead to a more compact and light design of a direct-driven generator. The latter statement is however valid only under one condition: that the rate of the flux linked to the winding $\widehat{\Phi}_{mf1}$ is independent of the pole length $\tau_{p,r}$. In reality, the flux leakage is strongly dependent on the distance between adjacent magnets, in this way penalizing topologies with a short pole pitch or a large pole number. Furthermore, as was described in Section 5.4, the flux linked to the winding is to a large extent related to the airgap length and magnet height. To account for this variation of the flux linkage in the machines with varying pole lengths, the following study is conducted.

At first, the electromagnetic force is calculated with the help of Eq. 6.13, where the flux linkage due to magnets acting alone $\widehat{\Phi}_{mf1}$ is computed in the static finite element analysis as described in Section 5.4. To assure similar conditions for topologies with the various pole lengths, the total axial length of the machine L_m and the magnet/stack coverage are kept constant throughout the study. This implies that the pole number is subject to variation depending on the pole length $\tau_{p,r}$ selected.

If the magnitude of the armature current and the angle ψ are fixed ($\psi = 0°$) in Eq. 6.13, the electromagnetic force becomes proportional to

$$F_{em} \propto p^2 \widehat{\Phi}_{mf1}, \tag{6.15}$$

The variation of the normalized electromagnetic forces with the airgap length and magnet height for the machines with BTFM and IBTFM topologies are presented in Fig. 6.11 and Fig. 6.12 respectively. The general trend of the forces fol-

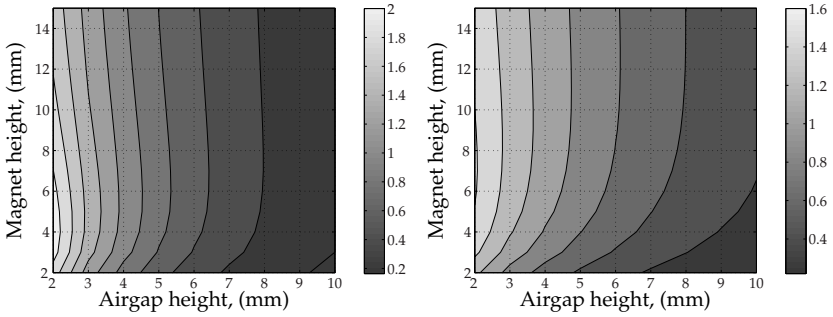

(a) (b)

Figure 6.11: Normalized force in pu values as a function of the airgap length and magnet height for the BTFM topology (a) with $\tau_{p,r} = 15\,\mathrm{mm}$, $l_{m,r} = 10\,\mathrm{mm}$, $l_{st,r} = 10\,\mathrm{mm}$ and (b) with $\tau_{p,r} = 30,\ \mathrm{mm}\, l_{m,r} = 20,\ \mathrm{mm}\, l_{st,r} = 20\,\mathrm{mm}$.

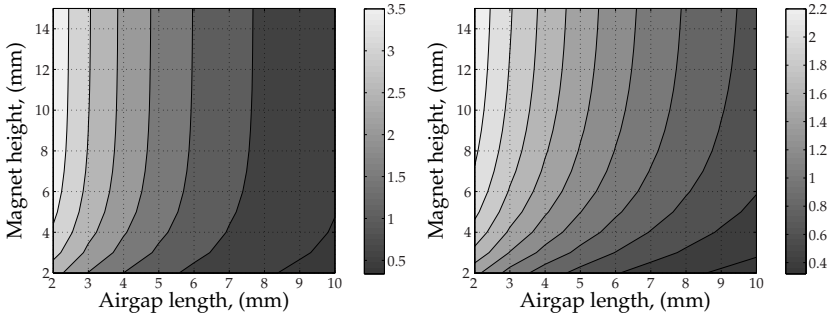

(a) (b)

Figure 6.12: Normalized force in pu values as a function of the airgap length and magnet height for the IBTFM topology (a) with $\tau_{p,r} = 15\,\mathrm{mm}$, $l_{m,r} = 10\,\mathrm{mm}$, $l_{st,r} = 10\,\mathrm{mm}$ and (b) with $\tau_{p,r} = 30,\ \mathrm{mm}\, l_{m,r} = 20,\ \mathrm{mm}\, l_{st,r} = 20\,\mathrm{mm}$.

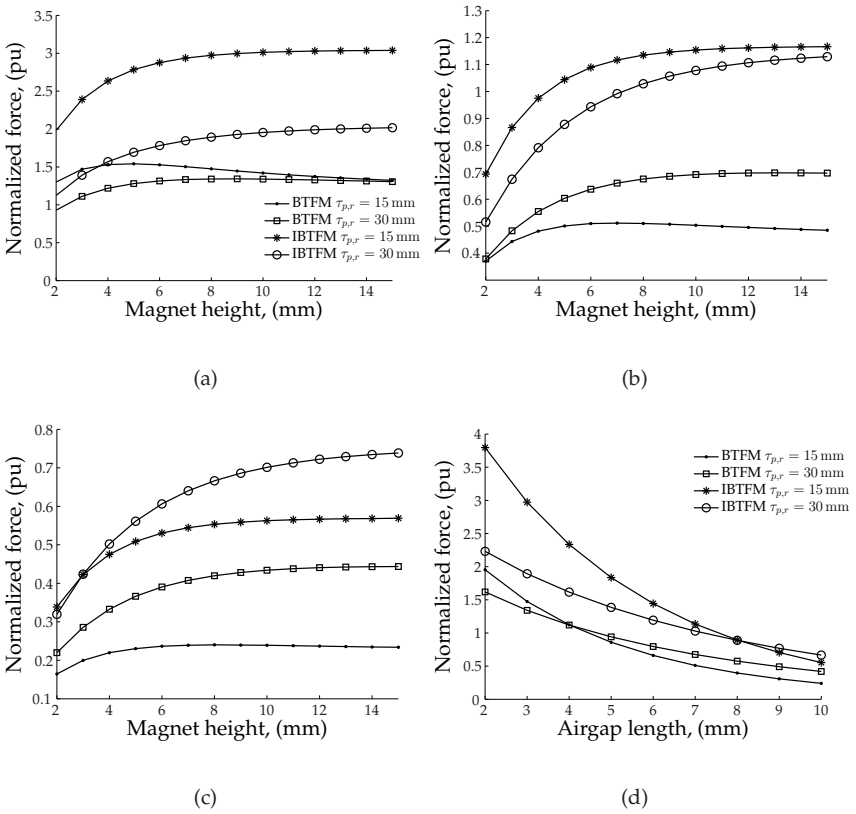

Figure 6.13: Normalized force in pu values as a function of the magnet height for (a) $g = 3\,\mathrm{mm}$, (b) $g = 7\,\mathrm{mm}$, (c) $g = 10\,\mathrm{mm}$ and (d) normalized force in pu values as a function of the airgap length for $h_m = 8\,\mathrm{mm}$.

lows the variation of the flux linkages obtained in Section 5.4. The normalization is common for all the studied models.

When the airgap is relatively small, the machines with the pole length of 15 mm is the best option, as it gives the largest values of the normalized torque. For the machines with the larger airgaps, the electromagnetic force production is reduced following the general trend of the flux linkage.

To analyze variation of the normalized force with the airgap length in more detail, the topologies with $g = 3, 7, 10\,\mathrm{mm}$ are studied more closely. The results for the BTFM and IBTFM topologies are depicted in Fig. 6.13(a-c). As can be seen, for machines with the airgap length below 7 mm, the topologies with $\tau_{p,r} = 15\,\mathrm{mm}$ are the best choice. The IBTFM topology is generally prevailing over the BTFM.

Once the airgap length exceeds 7 mm, the machines with the longer poles should be preferred. However, to achieve larger values of the electromagnetic force for these machines, magnets of larger height are required.

To compare machines with the same volume of the magnets utilized, topologies with $h_m = 8\,\mathrm{mm}$ are plotted in Fig. 6.13(d). As can be seen, the electromagnetic force in the IBTFM with $\tau_{p,r} = 15\,\mathrm{mm}$ for $g = 3\,\mathrm{mm}$ is around 3 pu, while for machines with $g = 10\,\mathrm{mm}$ its value drops to 0.55 pu, almost a six-times reduction.

6.3 Conclusions

The performance evaluation of the transverse flux generator with the basic topology and that utilizing the iron bridges has been conducted with the aid of the three-dimensional static and dynamic simulations. At first, the power factor is estimated in the static model for the topologies with the initial geometry. The study has shown that the BTFM has a slightly higher power factor as compared to the IBTFM, as well as a somewhat better utilization of the magnetic material with respect to the power factor. The results from time-dependent analysis has proved to be consistent with the static simulations as the power factors were nearly the same.

The power factor has been evaluated for the topologies with varying dimension in the peripheral plane using static FEM analysis. The performance of the topologies with the best power factor in the studied range (0.62 in the BTFM and 0.57 in the IBTFM), as well as the topologies that gave the highest PF to magnet volume ratio have been compared with the dynamic simulations. A good agreement of PF calculated by the different methods has been achieved for the unsaturated machines.

The electromagnetic and cogging forces have been obtained in the topologies with the initial dimensions. The IBTFM was superior to the BTFM with respect to the force production, where the three-phase electromagnetic force was twice as much as in the BTFM. The force ripples of the three-phase electromagnetic force were found to be insignificant in both topologies.

Chapter 7

Performance Evaluation of Transverse Flux Generators

The results of the studies conducted in chapters 5 and 6 are applied in this chapter to estimate the outer dimensions and performance of transverse flux generators with toroidal and cylindrical shapes. First, the four types of generators with different structures are analyzed with respect to the electromagnetic torque production in a given nacelle volume. Then the variation of the outer diameter and some other key values are investigated for the various output powers.

7.1 Torque Calculation in Generators with Different Structures

The aim of the study described in this section is to investigate the torque production of transverse flux generators with various topologies and shapes for a specified nacelle volume. To ensure equal condition for the studied generators, the axial length L_m varies proportionally with the outer diameter D_{out}. In this way, the effectiveness of each topology can be investigated. As the armature current is kept constant (both amplitude and angle) and the pole number is the same for a given outer diameter, the electromagnetic torque becomes dependent only on the rate of change of flux linked to the winding. In other words, the better utilization of the magnets is achieved, the smaller is the outer diameter that the generator would require.

Design Procedure Description

To produce a multiphase machine, single-phase units are placed (stacked) together in the radial direction and the magnets are shifted by 120 electrical degrees. If the stacking is done along a straight line, the generator will have a cylindrical shape, as

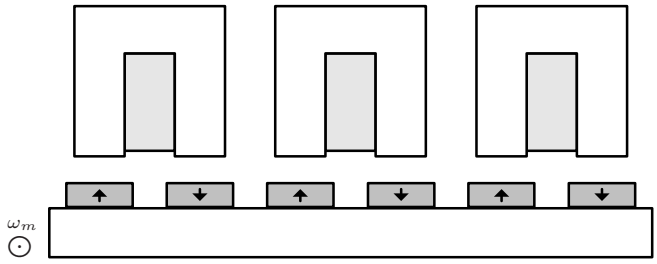

(a) Cylindrical TFM

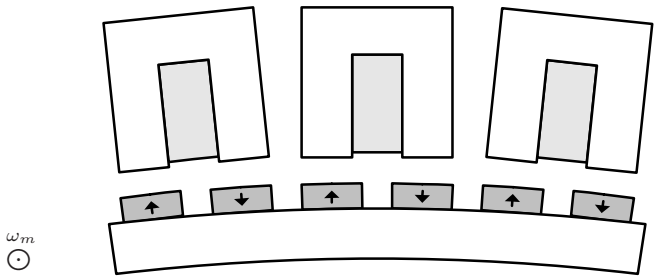

(b) Toroidal TFM

Figure 7.1: Possible arrangement of the single phase units: (a) cylindrical and (b) toroidal.

shown in Fig. 7.1(a). Else, if the units are stacked along a circumference, the shape of the generator would be toroidal (Fig. 7.1(b)). The four following generators are considered in the analysis:

1. Toroidal generator with the basic topology.
2. Toroidal generator with iron bridges.
3. Cylindrical generator with the basic topology.
4. Cylindrical generator with iron bridges.

The dimensions of the single phase-units in the radial (stack) plane are chosen as in Table 5.1. Sinusoidal armature current I_a is injected in the winding with the rms value of 545 A. The current is set in phase with the no-load voltage E_f, thus the angle $\psi = 0$ (see Fig. 6.2(a)). The number of conductors per slot is selected $n_s = 1$ for simplicity and the fill factor is chosen as $k_{fill} = 0.45$.

The ratio between the main radius R_m and the tube radius R_s in the toroidal TFM is kept constant, i.e. $k_R = 0.73/1.65$. The angle ξ required for the supporting structure should be selected as $\xi \geq 60°$. These values are adopted based on the analysis conducted in [48]. The exact value of ξ can be obtained from:

$$\xi = \pi - \frac{Q_s \tau_{p,s}}{R_s + h_{yr}}, \tag{7.1}$$

where Q_s is the number of slots per stator stack and should be a multiple of the number of phases.

To determine the pole number for the chosen machine radius, the maximum radius of the rotor core $R_{rc\,\max}$ is calculated, as:

$$R_{rc\,\max} = R_m + R_s + h_{yr}. \tag{7.2}$$

Adopting the maximum pole length in the peripheral direction as $\tau_{p,r\,\max} = 15\,\mathrm{mm}$ (for details see Chapter 5), the pole number can be obtained from:

$$p \geq \frac{2\pi R_{rc\,\max}}{\tau_{p,r\,\max}}. \tag{7.3}$$

And the closest even number thus selected as the pole number of the machine.

The pole length varies depending on the position on the rotor surface. To determine the pole length for each single-phase unit, the radius R_r for each stator slot should be calculated

$$R_r(i) = R_m - R_s \cos\big[(i-1)\alpha_{p,s} + \xi\big], \tag{7.4}$$

where i is in the interval $[1, Q_s]$ and the pole angle in the radial direction $\alpha_{p,s}$ is given by

$$\alpha_{p,s} = \frac{2(\pi - \xi)}{Q_s}. \tag{7.5}$$

The pole length for each slot can thus be calculated, as:

$$\tau_{p,r}(i) = \frac{2\pi R_r(i)}{p}. \tag{7.6}$$

Once the pole length is determined for each single-phase unit, the combination of dimensions $l_{m,r}$ and $l_{st,r}$ that gives the largest flux linkage $\phi_m(i)$ is selected according to the results obtained in sections 5.3 and 5.3. The magnet and stack thicknesses are constant within a sector. Equation 6.14 is then used to calculate the electromagnetic torque T_{em}.

To calculate the torque density the volume and the weight of the machine should be defined. The outer diameter and axial length of the machine are given by

$$\begin{cases} D_{out} &= 2(R_m + R_s + h_{yr} + h_m + g + h_{ss} + h_{ys}), \\ L_{out} &= 2(R_s + h_{yr} + h_m + g + h_{ss} + h_{ys}). \end{cases} \tag{7.7}$$

To be able to compare generators with different shapes, the outer dimensions of cylindrical generators are kept the same as the generators with toroidal shape. The dimensions of the single-phase units, the amplitude of the armature current and the winding parameters are also adopted as in the toroidal generators. The number of slots per stator stack Q_s and the pole number p are calculated for the outer dimensions as given by Eq. (7.7).

Calculation of the active portion of the total weight of generators with various shapes and topologies is summarized in Appendix B.

Results

The results of the electromagnetic torque computations in the four studied generators are illustrated in Fig. 7.2. The outer diameter in this study varies in the range of 2 to 10 meters while the airgap varying with the diameter as $g = 0.001 D_{out}$ and magnet height is constant. As the figure shows, the highest torque production for a given nacelle volume is obtained in the generators with the iron bridge transverse flux topology. For the outer diameter of 10 m, the electromagnetic torque in the IBTFM with toroidal shape is approximately 25% larger than in the IBTFM with cylindrical shape. The advantage of using iron bridge topology becomes even more evident when compared to the basic topology.

Fig. 7.3 shows variation of the electromagnetic torque per volume occupied by generator and the electromagnetically active portion of the generator weight. Although generators with cylindrical shape have generally higher torque-per-weight ratio for a specified outer diameter, toroidal generators have higher utilization of the space available in the nacelle in terms of the torque production.

Another important merit for analysis of large wind generators is the electromagnetic torque produced in a certain volume. With higher value of $\mathrm{Nm/m^3}$ the nacelle volume and thus its total weight can be reduced. Thanks to a more compact arrangement of the toroidal structure together with the high flux linkage of the IBTFM topology, this type of generators has the highest utilization of the available space, as shown in Fig. 7.3(b). This is a very important implication as the amount of inactive materials needed in a generator is strongly dependent on the diameter or volume of the generator.

7.2 Evaluation of Generators with Various Output Power

The outer dimensions and performance of the four transverse flux generators described previously are analyzed in this study with respect to the output power varying in the range of 1-10 MW. The axial length of the generators L_m is kept constant for a given output power. In order to be able to compare generators with various shapes and topologies on the same basis, the dimensions of the magnetic circuit in the radial plane are selected as in the initial geometry in Chapter 5.

Design Procedure Description

Generally, the design procedure in this section follows the one described previously. The axial lengths of generators for a given output power are selected as close to the axial length of the toroidal generator with the iron-bridge topology as possible. In this case, toroidal generators would have the same tube radius R_s while the main machine radius R_m would vary depending on the required electromagnetic torque. A minor difference in the axial lengths of generators with toroidal and cylindrical shapes can exist. This is due to the fact that L_m in cylindrical generators is given by $L_m = 3Q_s\tau_{p,s}$, where the pole length $\tau_{p,s}$ is constant.

The generator's efficiency is assumed to be $\eta = 0.97$, i.e. output power is defined as

$$P_{out} = \eta T_{em}\omega_m. \tag{7.8}$$

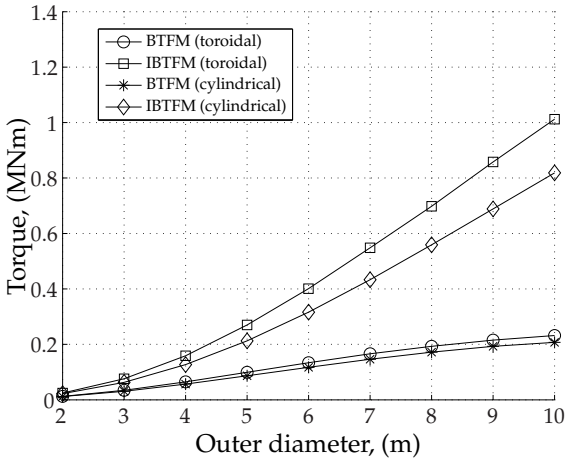

Figure 7.2: Variation of the electromagnetic torque with the outer diameter D_{out}

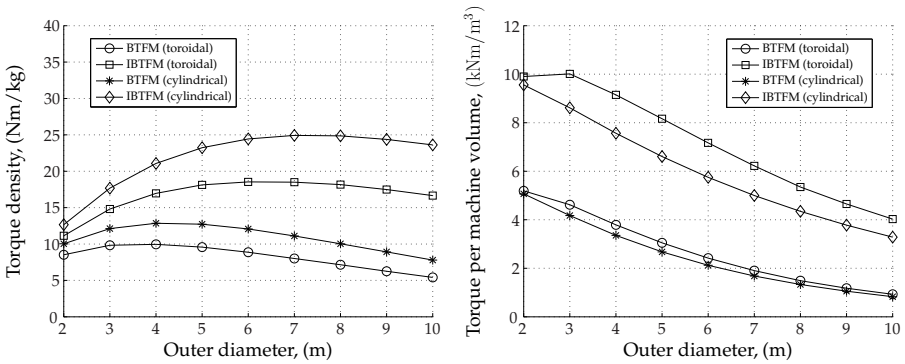

(a) Torque density as a function of D_{out}

(b) Torque per machine volume as a function of D_{out}

Figure 7.3: Variation of the torque per machine volume (a) and torque density (b) with the output diameter.

Nominal Speed

The nominal speed of the turbine n_m depends on a number of properties, such as the applied control method (fixed or variable speed), wind speed, radius of the blades, rated power, etc. As calculation of these characteristics is beyond the scope of this thesis, the rotational speed is selected based on review of the existing wind turbines. A survey of wind turbines with different configurations is presented in Fig. 7.4, where markers denotes the existent wind turbines and the solid line represents the adopted variation of n_m, described by

$$\frac{n_{m1}}{n_{m2}} = \left(\frac{P_{out2}}{P_{out1}}\right)^{1.5}. \tag{7.9}$$

Results

The six important characteristics selected for a more detailed analysis are shown in Fig. 7.5. Some key values for 5 and 10 MW wind turbines are summarized in Tables 7.1 and 7.2.

Outer Diameter

As can be observed in Fig. 7.5(a), the toroidal generator with the iron-bridge transverse flux topology requires the smallest outer diameter to produce the required torque. This implies that generators of this type would favor a reduced volume

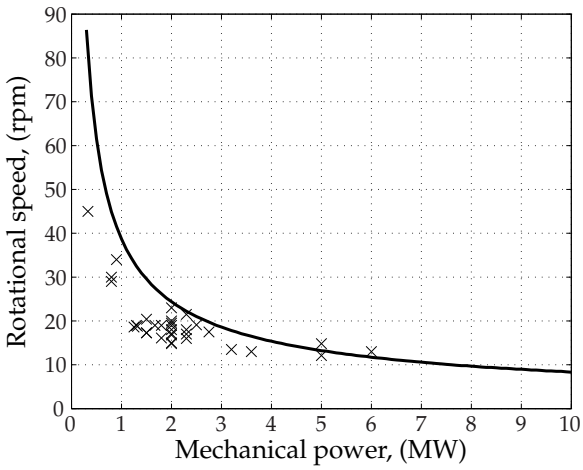

Figure 7.4: Speed variation with the output power P_{out}.

and weight of the nacelle. For a 5 MW wind turbine (see Table 7.1), D_{out} is around 10.5 m. It is by 1.6 m (or 15%) smaller than D_{out} required for a cylindrical generator with IBTFM and by 4.3 m (or 41%) as compared to the toroidal BTFM (for comparison see Fig. 7.6). The least attractive alternative in this regard is the cylindrical generator with the basic TFM topology which requires a 17.5 m outer diameter. The difference becomes even more pronounced in the wind turbine rated 10 MW (see Table 7.2), where the toroidal IBTFM allows D_{out} to be decreased by more than 2.5 m as compared to the IBTFM with the cylindrical shape.

Torque Density

Cylindrical generators have the best utilization of the active materials, as shown in Fig. 7.5(b). The torque-per-weight ratio of active materials tends to increase with the generator rating, as for example in the cylindrical IBTFM rated 5 MW, it is 82.1 Nm/kg and nearly 1.5 times more in a 10 MW wind turbine (123.5 Nm/kg). Toroidal generators in this regard have a lower utilization of active material.

Weight

The weight of active materials involved in the energy conversion process is an important characteristic of wind generators. Comparison of the total active weight and weight of the most expensive material used in the machine – permanent magnets – with respect to the output power is illustrated in Fig. 7.5(c) and 7.5(d), respectively. The weight tends to increase linearly with the output power. The cylin-

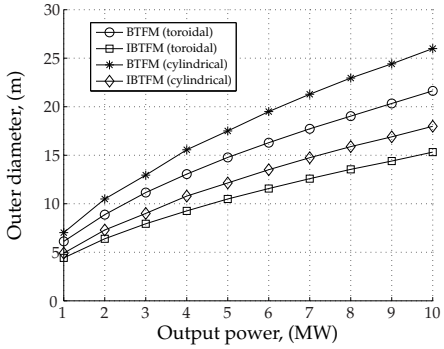

(a) Outer diameter as a function of P_{out}

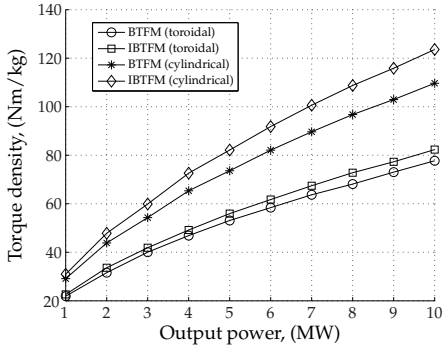

(b) Torque density as a function of P_{out}

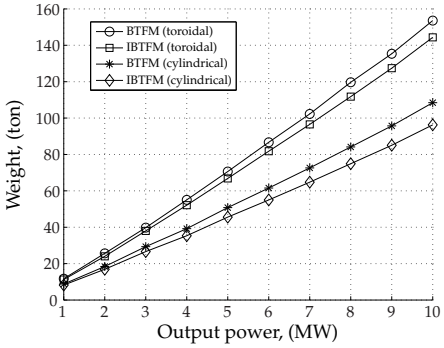

(c) Total active weight as a function of P_{out}

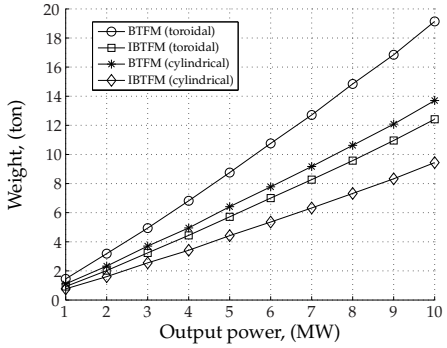

(d) Weight of magnets as a function of P_{out}

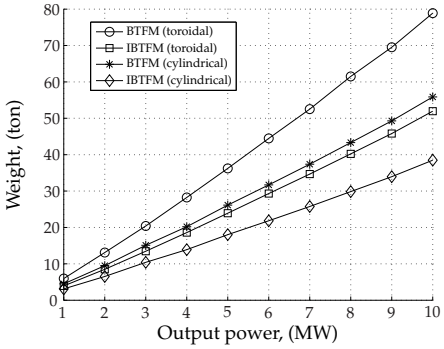

(e) Rotor weight as a function of P_{out}

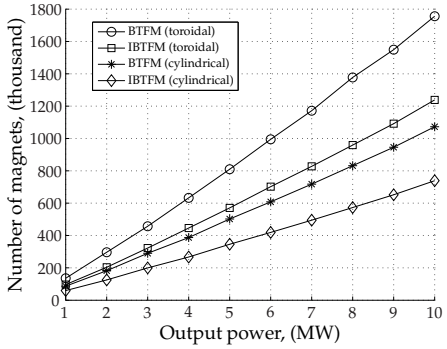

(f) Number of magnets as a function of P_{out}

Figure 7.5: Relationship of the outer diameter (a), torque density (b), total active weight (c), weight of magnet material (d), rotor weight (e) and the number of magnets with the output power (f).

Table 7.1: Data for 5 MW generator with different topologies

Property and unit	Toroidal		Cylindrical	
	BTFM	IBTFM	BTFM	IBTFM
Outer diameter, (m)	14.8	10.5	17.5	12.1
Axial length, (m)	3.4	3.4	3.5	3.5
Total active weight, (ton)	70.6	66.8	50.8	45.6
Weight of magnets, (ton)	8.8	5.7	6.4	4.4
Torque density, (Nm/kg)	53.1	55.9	73.6	82.1
Torque per machine volume, $(\mathrm{kNm/m^3})$	6.5	12.9	4.5	9.4
Pole number	3 068	2 162	3 638	2 508
Number of magnets, (thousand)	810	571	502	346
Copper losses, (kW)	157	114	111	90
Heat flow on the cooling surface, $(\mathrm{W/m^2})$	1 010	1 040	590	470

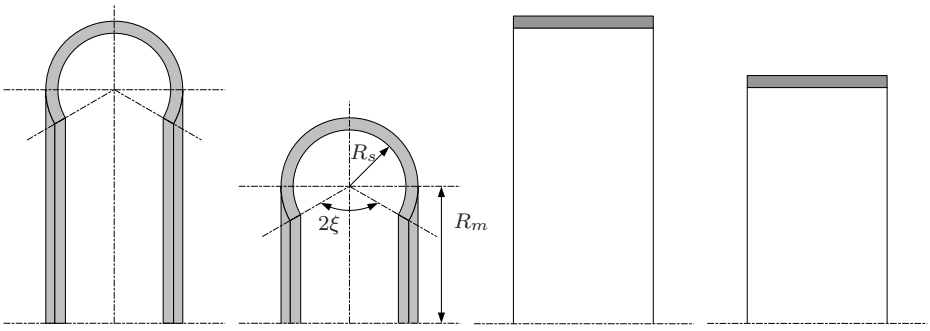

(a) Toroidal BTFM (b) Toroidal IBTFM (c) Cylindrical BTFM (d)Cylindrical IBTFM

Figure 7.6: Scaled cross sections of four 5 MW wind transverse flux generators with various structure.

Table 7.2: Data for 10 MW generator with different topologies

Property and unit	Toroidal		Cylindrical	
	BTFM	IBTFM	BTFM	IBTFM
Outer diameter, (m)	21.6	15.3	26.0	18.0
Axial length, (m)	4.8	4.8	5.0	5.0
Total active weight, (ton)	153.5	144.3	108.5	96.3
Weight of magnets, (ton)	19.1	12.4	13.7	9.4
Torque density, (Nm/kg)	77.7	82.3	109.7	123.6
Torque per machine volume, $(\mathrm{kNm/m^3})$	6.7	13.3	4.5	9.5
Pole number	4 502	3 176	5 416	3 732
Number of magnets, (thousand)	1 756	1 239	1 072	739
Copper losses, (kW)	340	240	237	182
Heat flow on the cooling surface, $(\mathrm{W/m^2})$	1 033	1 032	587	451

drical IBTFM offers the lowest total active weight as well as the weight of the PMs per given output power.

A more detailed comparison of the weight of different parts of the generators for 5 and 10 MW can be found in Fig. 7.7 and in Tables 7.1 and 7.2. A vast part of the active weight of the generators with iron-bridge topology consists of the weight of the stator iron, (around 45% in toroidal and 38% in cylindrical), which, in contrast to the BTFM topology, has iron bridges and longer teeth. The weight of the rotor iron is a major part of the total active weight in the TFM generators with the basic topology (around 38%). The best utilization of magnet material can be achieved in the IBTFM generators where the flux linkage is higher than in the BTFM.

Apart from the active portion of the total weight, the inactive portion, such as weight of the supporting structure, driving train, and nacelle of a wind turbine are also of great importance. Therefore, as the ratio of inactive/active material increases rapidly with size and volume, the toroidal IBTFM is expected to have a reduced total weight when the inactive portion of the total weight of large-size

generators is included in the calculations. This is confirmed in the study conducted in [53] which showed that the weight of the mechanical support increases drastically with the airgap diameter.

The comparison of the rotor weight is depicted in Fig. 7.5(e). As the rotor weight is also one of the characteristics that defines the size and the weight of the supporting structure, it is preferable to have it as light as possible. The cylindrical generator, closely followed by the toroidal generator, both with iron-bridge topology, has the lightest weight as compared to other generators in the studied interval of the output powers.

Magnets

One of the drawbacks of large transverse flux machines is the large number of permanent magnets. As the size of single-phase units and thus the magnets dimensions should be kept unchanged with increasing diameter of the TFM, the total number of magnets becomes quite large. The comparison of number of magnets in 5 and 10 MW turbines is shown in Tables 7.1 and 7.2. The cylindrical IBTFM generator requires the lowest number of magnets for a given output power. In the generators of the other types, this value can exceed one million pieces.

Efficiency

Another important characteristics of any electrical machine is the efficiency. As winding length varies with outer diameter, the winding resistance and thus the copper losses would vary as well. Estimation of copper losses in the studied generators is tabulated in Tables 7.1 and 7.2. The copper losses are lowest in the cylindrical IBTFM (less than 2%) and largest in the toroidal BTFM (more than 3%). Although toroidal machines produce more losses that should be extracted to avoid overheating, the total heat flow from the outer (cooling) surface is relatively low (around $1\,\mathrm{kW/m^2}$) and thus should not become a problem when designing the cooling system.

7.3 Conclusions

An analytical procedure based on the results from the FEM simulations has been applied for evaluation of the transverse flux generators with different shapes and topologies. The effectiveness of each topology has been investigated based on the estimation of the torque production in a certain nacelle volume. The toroidal generator with the iron-bridge topology has proved to be the most compact alternative for a wind turbine as it has the highest torque-per-volume ratio.

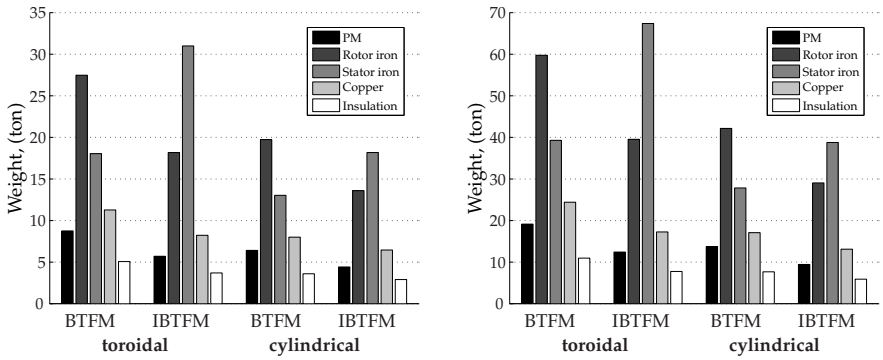

(a) 5 MW (b) 10 MW

Figure 7.7: Weight in different parts of the machine.

The study has followed by investigation of four types of generators with various output power. The toroidal IBTFM requires the smallest diameter for a given electromagnetic torque, although the utilization of active materials is lower than in the cylindrical generator with the same topology. However, as the ratio of inactive to active material increases rapidly with increasing size and volume, the toroidal IBTFM is expected to have the lowest total weight compared to the other alternatives. The total number of magnets has been shown to be one of the main challenges in the transverse flux machines with a large diameter.

Chapter 8

Improved Analytical Model

The analytical model described in [48] has accounted only for the flux leakage taking place in the radial plane of the machine. As was shown in the previous chapters, the flux linkage due to the previously disregarded flux leakage was overestimated by a factor of three in the machines with the basic transverse-flux topology and by a factor of two in the topology utilizing iron bridges. The aim of the study presented in this chapter is to improve the analytical model in [48] by taking into consideration the pole-to-pole flux leakage. The flux linkage is calculated for two cases: when the machine is at no-load condition with the permanent magnets acting alone and when the magnets are turned-off and the flux is due to armature reaction alone. The results of this study are compared with the results of the finite element calculations described in the previous chapters.

8.1 Analytical Model at No-load

Analytical modeling of the transverse flux machines is a complex task as the flux paths in these machines are truly three-dimensional. The flux paths can change with dimensions, which implies that the analytical model should be adjusted accordingly. Therefore, it would be difficult to develop a universal analytical model that could work successfully for the whole span of dimensions used in Chapter 5 and Chapter 6. If a more detailed model is required, the analytical calculations can be combined with FEM simulations as was done in [54] and [55].

The reluctance circuits are derived for both analyzed transverse flux topologies. The model presented for the BTFM topology is adopted with all necessary adjustments from the analytical model described in [36]. As the flux linkage variation with position is nearly sinusoidal in the unsaturated machines, the analytical

calculations load are reduced for the model when the stack is aligned with the magnets, i.e. *d*-axis simulations.

BTFM

At first, the flux paths and corresponding reluctances are identified for the transverse flux topologies with the basic configuration. The useful flux that is linked to the winding and contributes to the force production is in the radial direction. The fluxes between the adjacent poles in the peripheral direction are the leakage fluxes that partially weaken the main flux.

At first, the reluctances of the C-shaped core constituting the stator of the transverse flux machine with the basic topology are described. The flux originating from the magnets crosses the stator teeth and the stator yoke. In the following text, subscript 'm' stands for the 'no-load' model. The reluctance circuit for the BTFM is depicted in Fig. 8.1.

The reluctance of the stator yoke $\mathscr{R}_{mys}$ is calculated as

$$\mathscr{R}_{mys} = \frac{b_{ss} + b_{ts}}{\mu_0 \mu_{fe} h_{ys} \dfrac{l_{st,r}}{2}}, \tag{8.1}$$

where $\mu_0 = 4\pi \times 10^{-7}\,\mathrm{H/m}$ is the permeability of free space and μ_{fe} is the relative permeability of the iron. Due to symmetry only half of the stator yoke is modeled, thus the denominator includes $(l_{st,r}/2)$. The same rule is applied for all the reluctances in the radial plane.

In a similar way, the reluctance of the stator teeth $\mathscr{R}_{mts}$ can be obtained from:

$$\mathscr{R}_{mts} = \frac{h_{ss} + \dfrac{h_{ys}}{2}}{\mu_0 \mu_{fe} b_{ts} \dfrac{l_{st,r}}{2}} \tag{8.2}$$

Rotor reluctances consist of the radial and the axial components. The reluctance of the magnet with the positive polarity $\mathscr{R}_{mmp1}$ belongs to the radial components as the flux is in the radial direction:

$$\mathscr{R}_{mmp1} = \frac{h_m}{\mu_0 \mu_{pm} l_{m,s} \dfrac{l_{m,r}}{2}} \tag{8.3}$$

As the magnet with the negative polarity and the magnets of adjacent poles have the same physical dimensions, the reluctances of those magnets are defined in the same way as in Eq. 8.3, i.e.

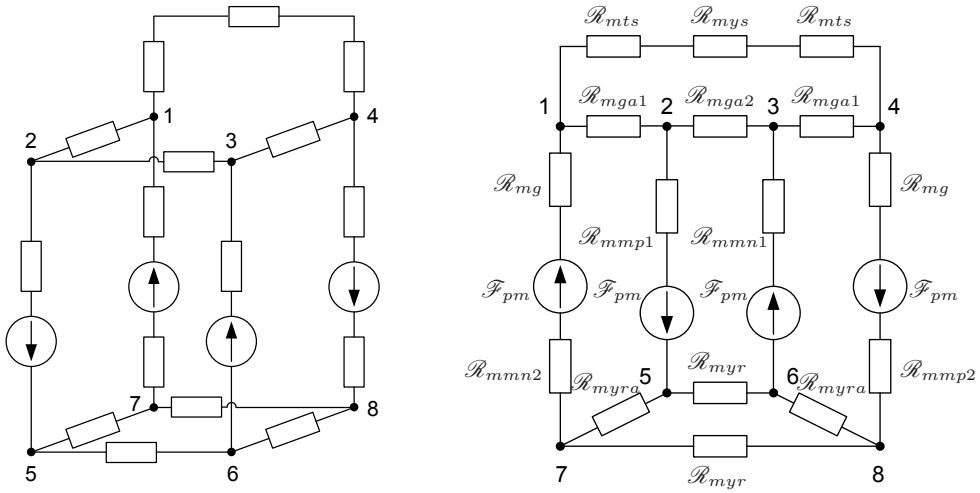

(a) No-load circuit in 3D

(b) No-load circuit

Figure 8.1: Reluctance circuit of the BTFM at no-load calculations.

$$\mathscr{R}_{mmn1} = \mathscr{R}_{mmp2} = \mathscr{R}_{mmn2} = \mathscr{R}_{mmp1}. \tag{8.4}$$

The reluctance of the rotor yoke in the radial direction $\mathscr{R}_{myr}$ is

$$\mathscr{R}_{myr} = \frac{\tau_{p,s}}{\mu_0 \mu_{fe} h_{ys} l_{m,r}} \tag{8.5}$$

The rotor leakage reluctance in the axial direction between the adjacent magnets $\mathscr{R}_{myra}$ is given by

$$\mathscr{R}_{myra} = \frac{\tau_{p,r} - \frac{l_{m,r}}{2}}{\mu_0 \mu_{fe} h_{ys} l_{m,s}}. \tag{8.6}$$

Similarly to the reluctance of the rotor iron, the airgap reluctance consists of the radial component $\mathscr{R}_{mg}$ that can be calculated as:

$$\mathscr{R}_{mg} = \frac{g}{\mu_0 \frac{l_{m,r}}{2} l_{m,s}}, \tag{8.7}$$

and the axial component $\mathscr{R}_{mga1}$ that consists of three components, which describe the leakage path between the stator tooth and the magnets of the adjacent pole

$$\mathscr{R}_{mga11} = \frac{g}{\mu_0 l_{m,s} \dfrac{l_{m,r}}{2}} \tag{8.8}$$

$$\mathscr{R}_{mga12} = \frac{\pi l_{m,r}}{4\mu_0 l_{m,s} \dfrac{l_{m,r}}{2}} \tag{8.9}$$

$$\mathscr{R}_{mga13} = \frac{\tau_{p,r} - l_{m,r}}{\mu_0 l_{m,s} \dfrac{l_{m,r}}{2}} \tag{8.10}$$

Finally, the axial component of the airgap reluctance is derived as

$$\mathscr{R}_{mga1} = \mathscr{R}_{mga11} + \mathscr{R}_{mga12} + \mathscr{R}_{mga13}. \tag{8.11}$$

The airgap leakage reactance between the magnets of the same pole $\mathscr{R}_{mga2}$ is given by:

$$\mathscr{R}_{mga2} = \frac{l_{mga2}}{\mu_0 l_{m,s} \dfrac{l_{m,r}}{2}}, \tag{8.12}$$

where the path for the leakage reluctance l_{mga2} is defined as

$$\begin{cases} \kappa_{mga2} &= 2 \arctan\left[\dfrac{\tau_{p,s}}{2(h_{yr} + h_m)}\right], \\ r_{mga2} &= \dfrac{h_{yr} + h_m}{\cos \dfrac{\kappa_{mga2}}{2}}, \\ l_{mga2} &= \kappa_{mga2}\ r_{mga2}. \end{cases}$$

The magnetomotive force originating from the magnet is given by

$$\mathscr{F}_{pm} = h_m H_c, \tag{8.13}$$

where H_c is the magnet coercive field strength that can be obtained from

$$H_c = \frac{B_{r,pm}}{\mu_0 \mu_{r,pm}}, \tag{8.14}$$

where $B_{r,pm}$ and $\mu_{r,pm}$ are the magnet remanent flux density and magnet relative permeability, respectively.

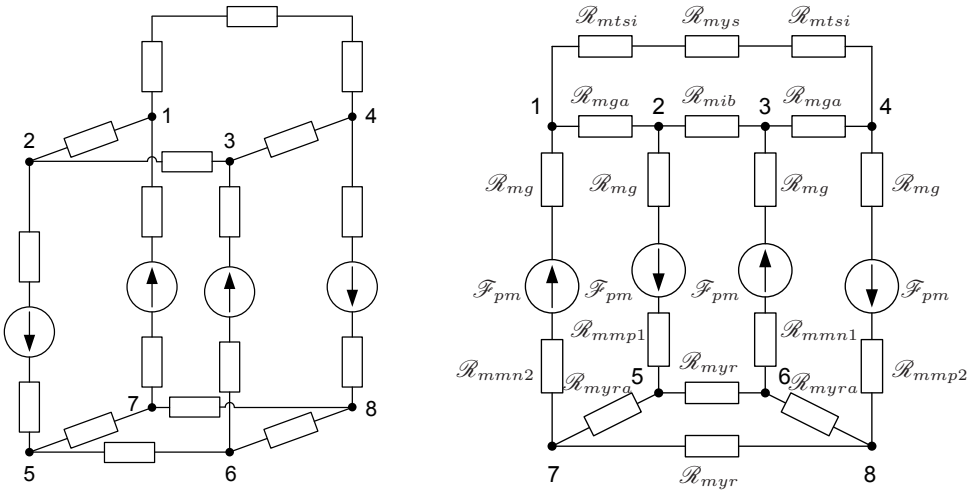

(a) No-load circuit in 3D

(b) No-load circuit

Figure 8.2: Reluctance circuit of the IBTFM for no-load calculations.

IBTFM

The reluctance model used for the analytical calculations of the transverse flux topology with the iron bridges is presented in Fig. 8.2. Most of the reluctances here are derived in the same way as in the BTFM.

To account for the increased height of the stator tooth, the reluctance $\mathscr{R}_{mtsi}$ is defined as

$$\mathscr{R}_{mtsi} = \frac{h_{ss} + \frac{h_{ys}}{2} + h_{ib}}{\mu_0 \mu_{fe} b_{ts} \frac{l_{st,r}}{2}} \tag{8.15}$$

The reluctance of the iron bridge is given by

$$\mathscr{R}_{mib} = \frac{\tau_{ps}}{\mu_0 \mu_{fe} h_{ib} \frac{l_{ib,r}}{2}}, \tag{8.16}$$

with h_{ib} being the height of the iron bridge and $l_{ib,r}$ its thickness.

The airgap leakage reactance between the stator stack and the iron bridge can be calculated as

$$\mathscr{R}_{mga} = \frac{\tau_{p,r} - l_{st,r}}{\mu_0 b_{ts} \frac{l_{m,r}}{2}}, \tag{8.17}$$

8.2 Analytical Model with the Armature Current

In this model, the sinusoidal armature current is flowing in the winding, while the permanent magnets are turned off; thus, the source of the magnetic flux $H_c = 0$.

BTFM

The reluctance model used for these calculations is shown in Fig. 8.3.

The radial component of the stator back reluctance $\mathscr{R}_{ays}$ equals

$$\mathscr{R}_{ays} = \frac{\tau_{p,s}}{\mu_0 \mu_{fe} h_{ys} l_{st,r}} \tag{8.18}$$

The axial component of the stator back reluctance in the air between the stacks $\mathscr{R}_{aysa}$ can be obtained from:

$$\mathscr{R}_{aysa} = \frac{\tau_{p,s}}{\mu_0 h_{ys} (2\tau_{p,r} - l_{st,r})}. \tag{8.19}$$

The reluctance of the upper part of the stator tooth $\mathscr{R}_{ats1}$ is given by

$$\mathscr{R}_{ats1} = \frac{\frac{h_{ts} + h_{ys}}{2}}{\mu_0 \mu_{fe} b_{ts} l_{st,r}}. \tag{8.20}$$

The corresponding axial reluctance $\mathscr{R}_{atsa1}$ is

$$\mathscr{R}_{atsa1} = \frac{\frac{h_{ts} + h_{ys}}{2}}{\mu_0 b_{ts} (2\tau_{p,r} - l_{st,r})}. \tag{8.21}$$

The reluctances in the radial and axial directions of the lower part of the tooth are the same as for the upper part of the tooth, i.e.

$$\mathscr{R}_{ats2} = \mathscr{R}_{ats1}, \tag{8.22}$$

$$\mathscr{R}_{atsa2} = \mathscr{R}_{atsa1}. \tag{8.23}$$

The slot leakage reluctance is divided into two parts

$$\mathscr{R}_{as1} = \mathscr{R}_{as2} = \frac{b_{ss}}{\mu_0 \frac{h_{ss}}{2} l_{st,r}}. \tag{8.24}$$

The axial component representing the flux leakage in the axial direction is given by

$$\mathscr{R}_{asa1} = \mathscr{R}_{asa2} = \frac{\tau_{p,s}}{\mu_0 \frac{h_{ss}}{2} (2\tau_{p,r} - l_{st,r})}. \tag{8.25}$$

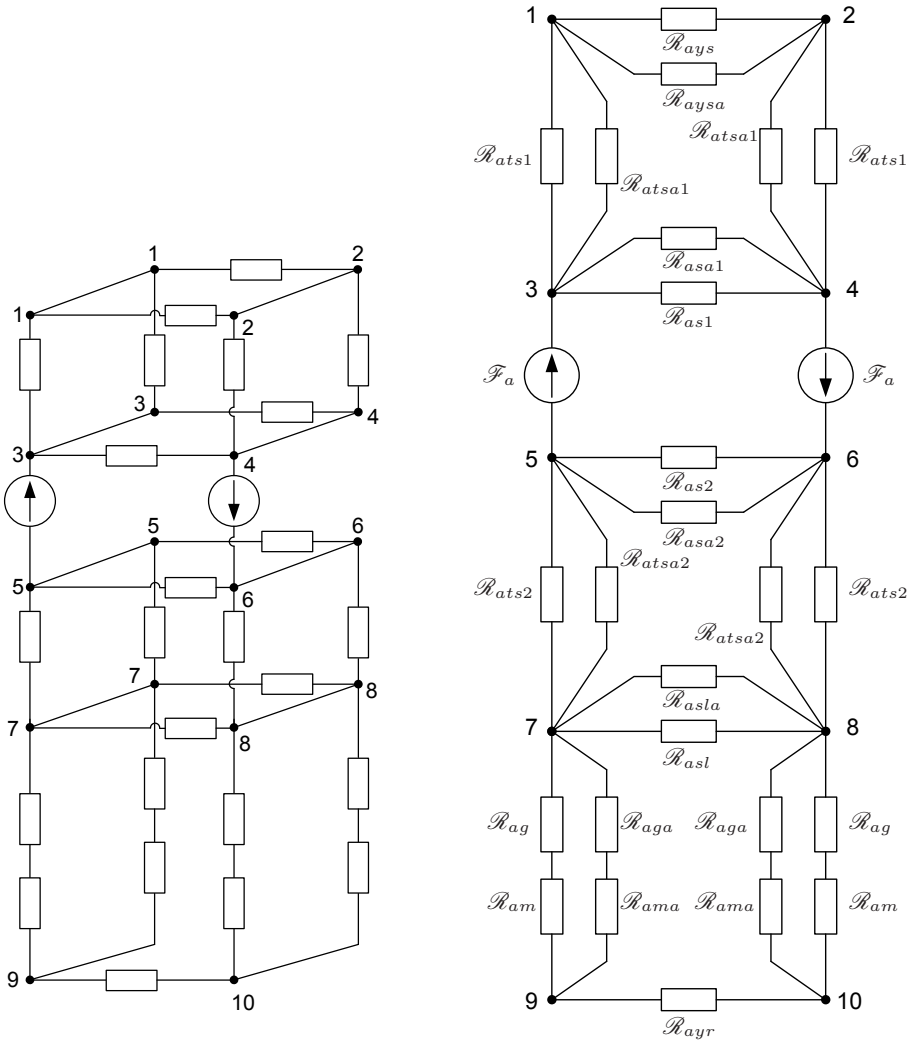

(a) Circuit in 3D with the armature current

(b) Circuit with the armature current

Figure 8.3: Reluctance circuit of the BTFM for the analysis with the armature current acting alone.

The airgap reluctance in the radial direction $\mathscr{R}_{ag}$ is defined by

$$\mathscr{R}_{ag} = \frac{g}{\mu_0 b_{ts} l_{m,r}} \tag{8.26}$$

And the leakage in the airgap in the axial direction is described by the reluctance $\mathscr{R}_{aga}$

$$\mathscr{R}_{aga} = \frac{g}{\mu_0 b_{ts}(2\tau_{p,r} - l_{m,r})}. \tag{8.27}$$

The reluctance in the air between the stator teeth in the radial direction $\mathscr{R}_{asl}$ can be calculated as follows. Recognize that:

$$\begin{cases} \kappa_{astl} &= 2\arctan\left(\frac{b_{ss}+b_{ts}}{h_{ss}}\right), \\ r_{asl} &= \frac{1}{2}\sqrt{(b_{ss}+b_{ts})^2 + h_{ss}^2}, \\ l_{asl} &= \kappa_{asl}\ r_{asl}. \end{cases}$$

Therefore,

$$\mathscr{R}_{asl} = \frac{l_{asl}}{\mu_0 b_{ts} l_{st,r}}. \tag{8.28}$$

The corresponding leakage reluctance in the axial direction $\mathscr{R}_{asla}$ is defined as

$$\mathscr{R}_{asla} = \frac{l_{asl}}{\mu_0 b_{ts}(2\tau_{p,r} - l_{st,r})}. \tag{8.29}$$

The magnet reluctance in the radial direction $\mathscr{R}_{am}$ is

$$\mathscr{R}_{am} = \frac{h_m}{\mu_0 b_{ts} l_{m,r}}. \tag{8.30}$$

The leakage reluctance between the adjacent magnets in the axial direction $\mathscr{R}_{ama}$ is given by

$$\mathscr{R}_{ama} = \frac{h_m}{\mu_0 b_{ts}(2\tau_{p,r} - l_{m,r})}. \tag{8.31}$$

The mover yoke reluctance $\mathscr{R}_{ayr}$ can be calculated as

$$\mathscr{R}_{ayr} = \frac{\tau_{p,s}}{\mu_0 \mu_{fe} 2\tau_{p,r} h_{yr}}. \tag{8.32}$$

The source of the electromotive force $\mathscr{F}_a$ in this case is derived from the Ampere's law:

$$\mathscr{F}_a = n_s i_a. \tag{8.33}$$

As the stator slot is modeled in two parts, the source of the electromagnetic force in Eq. 8.33 should be also divided by a factor of two.

IBTFM

The reluctance model for the IBTFM topology with the armature current alone is shown in Fig. 8.4. The reluctance of the iron bridge is described by

$$\mathscr{R}_{aib} = \frac{\tau_{p,s}}{\mu_0 \mu_{fe} h_{yr} l_{ib,r}}. \tag{8.34}$$

The reluctance of the lower part of the stator tooth is represented by the radial $\mathscr{R}_{ats3}$ and axial $\mathscr{R}_{atsa3}$ components. The radial component is found from

$$\mathscr{R}_{ats3} = \frac{h_{ib}}{\mu_0 \mu_{fe} b_{ts} l_{st,r}}. \tag{8.35}$$

The axial component $\mathscr{R}_{atsa3}$ consists of several parts connected in parallel. They represent the leakage paths from the different sides of the tooth to the neighboring iron bridges. The reluctances are derived as follows.

From the side of the tooth closest to the iron bridge:

$$\mathscr{R}_{atsa31} = \frac{\tau_{p,r} - l_{st,r}}{2\mu_0 h_{ib} b_{ts}}. \tag{8.36}$$

From the tooth base to the iron bridge base:

$$\mathscr{R}_{atsa32} = \frac{\pi \tau_{p,r}}{4\mu_0 b_{ts} l_{st,r}}. \tag{8.37}$$

From the inner side of the tooth to the iron bridge:

$$\mathscr{R}_{atsa33} = \frac{\pi \tau_{p,r}}{8\mu_0 h_{ib} l_{st,r}}. \tag{8.38}$$

From the outer side of the tooth to the side of the iron bridge:

$$\mathscr{R}_{atsa34} = \frac{\pi \tau_{p,r}}{4\mu_0 h_{ib} l_{st,r}}. \tag{8.39}$$

An extra leakage path from the upper side of the iron bridge to the stator tooth:

$$\mathscr{R}_{atsa35} = \frac{\pi \tau_{p,r}}{8\mu_0 b_{ts} l_{ib,r}}. \tag{8.40}$$

Finally, the reluctance $\mathscr{R}_{atsa3}$ can be calculated as

$$\mathscr{R}_{atsa3} = \frac{1}{\mathscr{R}_{atsa31}} + \frac{1}{\mathscr{R}_{atsa32}} + \frac{1}{\mathscr{R}_{atsa33}} + \frac{1}{\mathscr{R}_{atsa34}} + \frac{1}{\mathscr{R}_{atsa35}}. \tag{8.41}$$

The leakage reluctance between the inner sides of the teeth is given by

$$\mathscr{R}_{asli} = \frac{b_{ss}}{\mu_0 h_{ib} l_{st,r}}. \tag{8.42}$$

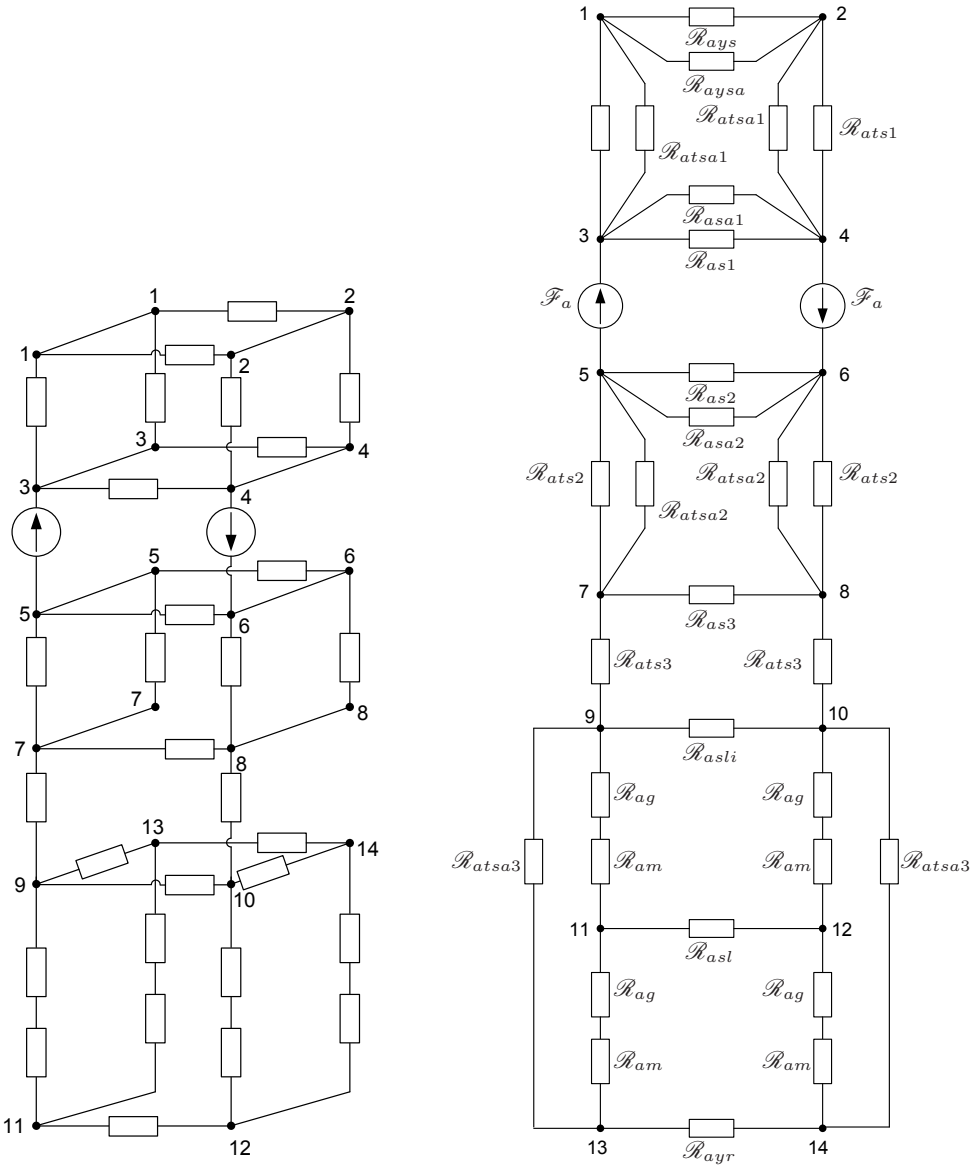

(a) Circuit in 3D with the armature current

(b) Circuit with the armature current

Figure 8.4: Reluctance circuit of the IBTFM for the analysis with the armature current acting alone.

8.3 Analytical vs. FEM Calculations

The models described above are used for calculations of the magnetic fluxes in the basic transverse-flux topology and that utilizing iron bridges with the initial geometry. By applying the dimensions of the initial geometries the circuits can be solved by Ohm's law. The comparison of the results is summarized in Table 8.1.

As can be seen, the flux in the BTFM at no-load was overestimated by around 8%, i.e. in FEM simulations $36.6\,\mu\mathrm{Wb}$ has been obtained while in the analytical calculations this value reached $39.5\,\mu\mathrm{Wb}$. The difference between the FEM and analytical results is less in the simulations with the armature current alone.

In the IBTFM the difference between the FEM and analytical results was quite small, although the circuit became more complicated. The difference here is 6% for the no-load case and 2% for the armature current alone.

Table 8.1: Comparison of the flux in $(\mu\mathrm{Wb})$ obtained in FEM and analytically

Topology	FEM	Analytical
BTFM at no-load	36.6	39.5
BTFM with the armature current	60.1	63.2
IBTFM at no-load	74.6	79.4
IBTFM with the armature current	140.8	137.8

8.4 Conclusions

The reluctance model developed in [48] has been extended in the direction of movement. The flux linkage has been estimated at no-load conditions and with the armature current alone. The comparison of the results with FEM simulations for the initial geometry showed a rather good agreement for the selected sets of dimensions. The analytical model can be used to provide a general idea of how the transverse-flux machine performance is dependent on its physical dimensions.

As compared to the three-dimensional finite element simulations, the analytical procedure described in this chapter is much less time consuming and thus can be used for the preliminary calculations or for the optimization procedure. However, if more precise results are required, FEM simulations should be conducted instead.

Chapter 9

Conclusions and Future Work

This chapter summarizes the work presented in this thesis. Some guidelines for the future work are given.

9.1 Conclusions

Introduction

This thesis has presented the analysis of a permanent magnet synchronous generator suited for direct-driven wind turbines in the megawatt class.

Different driving forces that in the past few decades contributed to the rapid development of renewable energy sources in general and wind power in particular have been addressed. It was found that the share of renewables in the world electricity mix has mainly been increased due to environmental concern and issues of energy security, which in turn prompted the governments in different countries to make decisions on economic support.

As far as the environment is concerned, renewable energy sources are better than the existing technologies. Renewable energy sources can also increase the security of energy supply, mainly due to decreased dependency on the imported fuel supply. Increased security is also achieved due to the distributed nature of renewable energy sources that can offer a reduced risk of grid failures.

Economic support of renewable energy sources is one of the main driving forces to their recent development. Different measures and policies have mainly been aimed at promoting renewable energy sources in the total electricity mix.

The basic difference between the turbines with the fixed and variable speed control has been described. Five different configurations of wind energy systems have been presented, four of which were utilizing a gearbox in order to adjust the

slow turbine shaft to a generally higher rotational speed of the generator. Examples of manufacturers using these configurations have been given. The emphasis has been placed on the direct-driven wind turbines and the topologies that could be employed in the energy converters. Following the literature review, the transverse flux topology has been found to be a promising alternative for the direct-driven wind turbine.

An overview of permanent-magnet synchronous generators with different means of force production has been presented. The pros and cons of each topology have been discussed, with an emphasis on the transverse flux configurations and their principle of operation. Various transverse flux topologies have been outlined and their possible applications have been discussed. The novel concept of arranging transverse-flux units has been presented.

Analysis at No-load

The finite element static and dynamic analyses of a direct-driven generator employing a basic transverse flux topology and that utilizing iron bridges have been presented. At first, the topologies with the initial dimensions were studied. As the selection of the pole length in the transverse flux machines affects the pole-to-pole flux leakage and thus its performance, the topologies have been analyzed with respect to the varying dimensions in the direction of movement.

The topologies utilizing IBTFM have been found to be superior to the BTFM with respect to the flux linkage (by 110%) and magnet utilization (by 84%). The machines with the longest magnets gave the largest flux linkage, while machines with the short magnets should be preferred for better magnet utilization. Four sets of dimensions have been selected for a dynamic finite element analysis.

Unlike the triangular waveform of the analytically calculated flux linkages in [48], the flux linkages obtained in FEM have been found to vary almost sinusoidally with time, which is due to the flux leakage between the adjacent magnets. A difference of up to 2% between the magnitude of the flux linkage from the static FEM analysis and its fundamental component from the dynamic simulations has been found, which made the static simulations sufficient for an approximate analysis. The variation of emfs proved to be less sinusoidal, especially in the IBTFM, with the third harmonic prevailing.

As the transverse flux machine consists of a number of identical units, the studies could be applied for generators with different shapes, such as toroidal and cylindrical shapes.

Analysis at Load

The performance evaluation of the transverse flux generator with the basic topology and that utilizing the iron bridges has been conducted with the aid of the three-dimensional static and dynamic simulations. At first, the power factor is estimated in the static model for the topologies with the initial geometry. The study has shown that the BTFM has a slightly higher power factor as compared to the IBTFM, as well as a somewhat better utilization of the magnetic material with respect to the power factor. The results from time-dependent analysis have proved to be consistent with the static simulations as the power factors were nearly the same in both simulations.

The power factor has been evaluated for the topologies with varying dimension in the peripheral plane using static FEM analysis. The performance of the topologies with the best power factor in the studied range (0.62 in the BTFM and 0.57 in the IBTFM), as well as the topologies that gave the highest PF to magnet volume ratio, have been compared with the dynamic simulations. A good agreement of PF calculated by the different methods has been achieved for the unsaturated machines. The PF in the saturated machine was underestimated.

The electromagnetic and cogging forces have been obtained in the topologies with the initial dimensions. The IBTFM was superior to the BTFM with respect to the force production, where the three-phase electromagnetic force was twice as much as in the BTFM. The force ripples of the three-phase electromagnetic force were found to be insignificant in both topologies.

Performance Evaluation of the Transverse Flux Generator

An analytical procedure based on the results from the FEM simulations has been applied for evaluation of the transverse flux generators with different shapes and topologies. The effectiveness of each topology has been investigated based on estimation of the torque production in a certain nacelle volume. Toroidal generator with the iron-bridge topology has proved to be the most compact alternative for a wind turbine as it has the highest torque-per-volume ratio.

The study was followed by investigation of four types of generators with various output power. The toroidal IBTFM requires the smallest diameter for a certain electromagnetic torque, although the utilization of active materials is lower than in the cylindrical generator with the same topology. However, as the ratio of inactive to active material increases rapidly with increasing size and volume, the toroidal IBTFM is expected to have the lowest total weight compared to the other alternatives. The total number of magnets has shown to be one of the main challenges in the transverse flux machines with a large diameter.

Improved Analytical Model

The flux linkage has been estimated at no-load conditions and with the armature current alone with the derived analytical model. The comparison of the results with FEM simulations for the initial geometry showed a rather good agreement for the selected sets of dimensions. The analytical model can be used to provide a general idea of how the transverse-flux machine performance is dependent on its physical dimensions. The analytical procedure described in this chapter can be used for the preliminary calculations or for the optimization procedure. However, if more precise results are required, FEM simulations should be conducted instead.

9.2 Future Work

In this thesis, the loss model has considered the copper losses by assigning a percentage of the output power of the studied generators. To account for the iron losses, as well as to improve the estimation of the copper losses, a more advanced loss model should be developed. Furthermore, the other potential sources of losses, e.g. losses in magnets due to eddy currents, friction losses in bearings, etc. should be examined. Once the loss model is developed, the thermal analysis of the generator should also be performed. The thermal analysis can help to improve the accuracy of the predicted generator performance.

To calculate the power factor of the machine, a control mode with the armature current aligned with q-axis has been used. To be able to optimize the price of the wind generator together with the power electronics, the current angle ψ and its influence on the entire system should be studied.

A linear prototype of the transverse flux generator studied in this work has been built and no-load measurements have been performed and compared. In order to verify the analytical and finite element analyses of the rotating TFM a downscaled prototype of the toroidal transverse flux generator should be built and tested.

Appendix A

Simulated Models

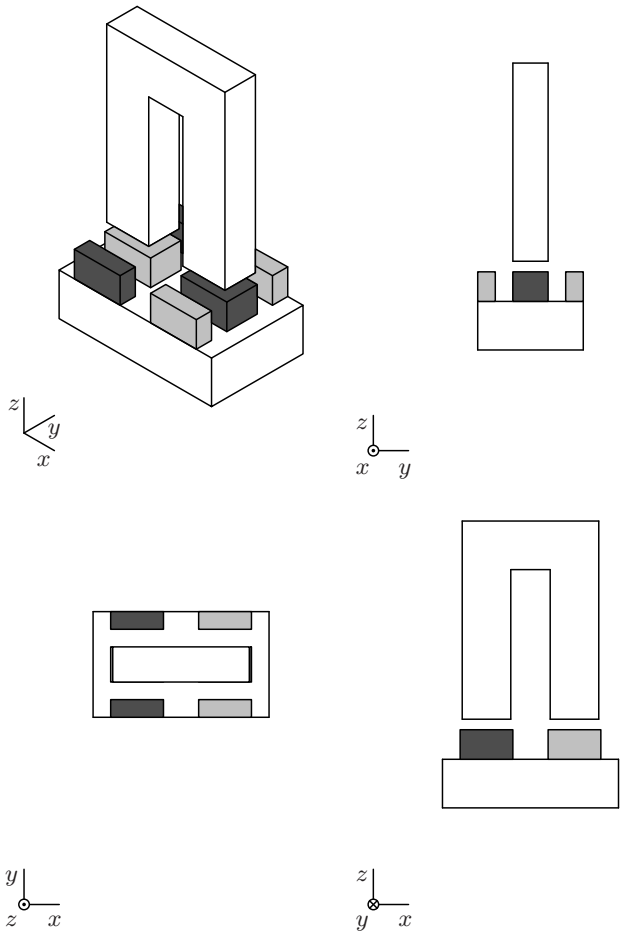

Figure A.1: Basic TFM topology.

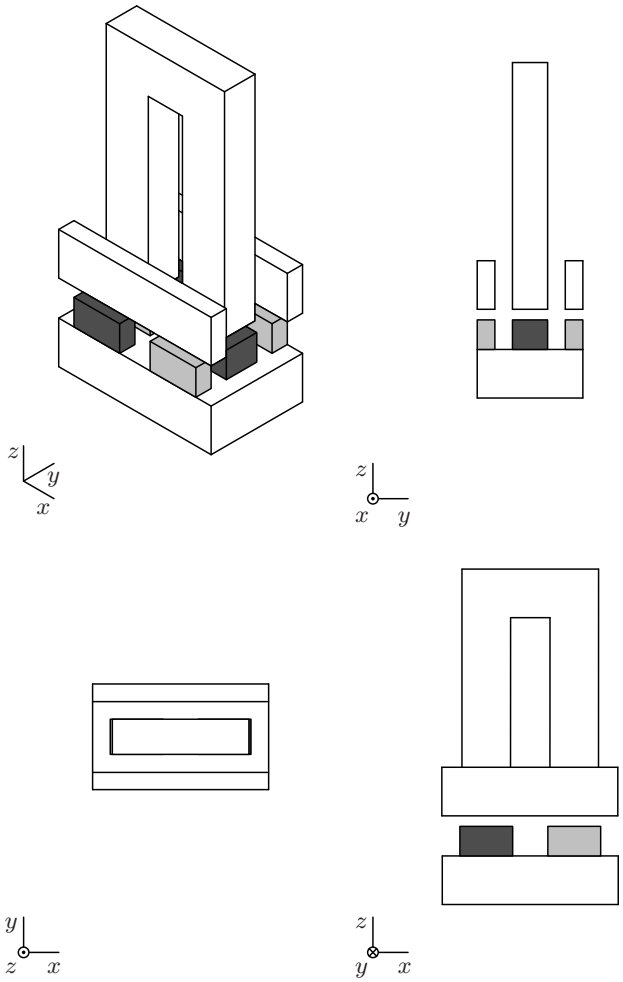

Figure A.2: TFM topology with the iron bridge.

Appendix B

Calculation of the Active Weight

Once the main dimensions of the machine are determined, the weight of the active materials can be calculated. The calculation of weight is estimated for toroidal and cylindrical generators.

The copper weight G_{cu} is obtained by multiplying the active copper area $k_{fill}\, A_{ss}$ and the length of the phase windings with its density ρ_{cu}.

$$G_{cu} = \rho_{cu} \left(l_a + l_b + l_c\right) h_{ss} b_{ss} k_{fill}. \tag{B.1}$$

The weight of the winding insulation G_{ins} is calculated as previously, but the area taken by the winding insulation is considered instead, i.e. $(1 - k_{fill})\, A_{ss}$

$$G_{ins} = \rho_{ins} \left(l_a + l_b + l_c\right) h_{ss} b_{ss} \big(1 - k_{fill}\big). \tag{B.2}$$

The magnet weight G_{pm} is defined as a sum of volumes of all the magnets in one row, where i is in interval $[1, Q_s]$, times the number of poles p and the magnet density ρ_{pm}

$$G_{pm} = 2\rho_{pm}\, p\, l_{m,s}\, h_m \sum_{i=1}^{Q_s} l_{m,r}(i). \tag{B.3}$$

The weight of the rotor yoke G_{yr} in the toroidal generator is given by

$$G_{yr} = \rho_{fe} \left\{ 2\pi R_m (\pi - \xi) \Big[R_s^2 - (R_s - h_{yr})^2 \Big] + \frac{4\pi \sin \xi}{3} \Big[R_s^3 - (R_s - h_{yr})^3 \Big] \right\}. \tag{B.4}$$

and in the cylindrical generator as:

$$G_{yr} = 2\, \rho_{fe}\, Q_s\, \tau_{p,s} \Big[\pi R_{rc}^2 - \pi \big(R_{rc} - h_{yr}\big)^2 \Big] \tag{B.5}$$

The weight of the stator stacks G_{ss}

$$G_{ss} = \rho_{fe} \frac{p}{2} \Big[\big(h_{ts} + h_{ys}\big) \big(b_{ss} + 2b_{ts}\big) - b_{ss} h_{ss} \Big] \sum_{i=1}^{Q_s} l_{st,r}(i), \tag{B.6}$$

In the generators with transverse flux topology utilizing iron bridges, the weight of the iron bridges G_{ibs} is calculated as

$$G_{ibs} = \rho_{fe}\, p\, h_{ib}\, \tau_{p,s} \sum_{i=1}^{Q_s} l_{ib,r}(i). \tag{B.7}$$

The total weight of iron G_{fe} is now obtained as

$$G_{fe} = G_{yr} + G_{ss} + G_{ibs}. \tag{B.8}$$

The total active weight G_{total} of the machine can finally be calculated as

$$G_{total} = G_{cu} + G_{fe} + G_{pm} + G_{ins}. \tag{B.9}$$

List of Figures

List of Tables

List of Symbols and Abbreviations

Roman Letters

A_{ss}	stator slot area	[m^2]
A_{turb}	interception area of the turbine blades	[m^2]
$\widehat{B}_g$	maximum flux density in the airgap	[T]
$\widehat{B}_{iron}$	maximum flux density in iron	[T]
$B_{r,pm}$	magnet remanent flux density	[T]
b_{ss}	stator slot width	[m]
$\widehat{B}_{ts}$	maximum flux density in the tooth	[T]
b_{ts}	tooth width	[m]
$\widehat{B}_{yr}$	maximum flux density in the rotor yoke	[T]
$\widehat{B}_{ys}$	maximum flux density in the stator yoke	[T]
D	diameter	[m]
D_{out}	machine outer diameter	[m]
e_f	instantaneous value of the induced emf	[V]
E_f	induced emf per phase	[V]
$\mathscr{F}$	mmf	[A]
f_e	electrical frequency	[Hz]
F_{em}	electromagnetic force	[N]
g	airgap length	[m]
G_{cu}	copper weight	[kg]
G_{fe}	iron weight	[kg]
G_{ins}	weight of the winding insulation	[kg]

G_{pm}	magnet weight	[kg]
G_{total}	total weight of active materials	[kg]
G_{ts}	weight of the stator teeth	[kg]
G_{yr}	weight of the rotor yoke	[kg]
G_{ys}	weight of the stator yoke	[kg]
H	magnetic field intensity	[A/m]
h_{ib}	iron bridge height	[m]
h_m	magnet height	[m]
h_{ss}	stator slot height in BTFM	[m]
h_{ssi}	stator slot height in IBTFM	[m]
h_{yr}	rotor yoke height	[m]
h_{ys}	stator yoke height	[m]
I_a	phase current	[A]
k_{fill}	fill factor	—
k_R	radii ratio R_s/R_m	—
L_a	armature inductance	[H]
$l_{ib,r}$	iron bridge thickness in the stack plane	[m]
L_m	machine axial length	[m]
$l_{m,s}$	magnet thickness in the stack plane	[m]
$l_{st,r}$	stack thickness in the rotational plane	[m]
n_m	rotational speed of the rotor	[rpm]
n_s	number of conductors in series per coil per slot	—
p	pole number	—
P_{cu}	copper losses	[W]
P_{fe}	iron losses	[W]
P_{out}	output, rated power	[W]
P_{wind}	power of wind	[W]
Q_s	number of stator teeth per stack	—
R_m	main machine radius	[m]
R_a	phase resistance	[Ohm]
R_r	radius on the rotor surface	[m]
R_s	tube radius	[m]
$\mathscr{R}$	reluctance	[At/Wb]

t	time	[s]
T_{em}	electromagnetic torque	[N m]
v_m	mechanical speed	[m/s]
V_{pm}	volume of permanent magnets	[m^3]
V_t	phase terminal voltage	[V]
v_{wind}	wind velocity	[m/s]
X_a	armature reactance	[Ω]

Greek Letters

$\alpha_{p,s}$	pole angle in the stack plane	[rad]
η	efficiency	—
μ_{rpm}	magnet relative permeability	—
ξ	angle for supporting structure	[rad]
ρ_{air}	air density	[kg/m^3]
ρ_{cu}	copper density	[kg/m^3]
ρ_{cu}	copper resistivity	[Ω m]
ρ_{fe}	iron density	[kg/m^3]
ρ_{ins}	insulation density	[kg/m^3]
ρ_{pm}	magnet density	[kg/m^3]
$\tau_{p,r}$	pole pitch in the rotational plane	[m]
$\tau_{p,s}$	pole pitch in the stack plane	[m]
φ	phase angle	[rad]
Φ_a, ϕ_a	flux generated by armature reaction	[Wb]
Φ_m, ϕ_m	flux generated by magnet	[Wb]
Φ_{tooth}	flux through the tooth base	[Wb]
$\Phi_{winding}$, $\phi_{winding}$	flux linked to the winding	[Wb]
ψ	load angle	[rad]
ψ_m	flux linkage due to armature reaction	[Wb]
ψ_m	flux linkage due to magnet	[Wb]
ψ_r	resultant flux linkage	[Wb]
ω_m	angular velocity of the rotor	[rad/s]
ω_e	angular frequency of the rotor	[rad/s]

Acronyms

AC	Alternative Current
DC	Direct Current
emf	Electro-Motive Force
FEM	Finite Element Method
NdFeB	Neodymium Iron Boron
PF	Power Factor
PM	Permanent Magnet
PMSM	Permanent Magnet Synchronous Machine
TFM	Transverse Flux Machine

Bibliography

[1] G.A.M. van Kuik. Are wind turbines growing too fast? In *Proc. European Wind Energy Conference and Exhibition*, pages 69–72, Copenhagen, Denmark, 2001.

[2] World wind energy report 2009. `http://www.wwindea.org/`.

[3] Directive 2001/77/EC of the European Parliament and of the Council of 27 September 2001 on the promotion of electricity produced from renewable energy sources in the internal electricity market. *Official Journal of the European Communities*, L283, 27 October 2001.

[4] T. Ackermann, editor. *Wind power in power systems*. John Wiley & Sons, Ltd, 2005.

[5] V. Smil. *Energy at the Crossroads – Global Perspectives and Uncertainties*. Massachusetts Institute of Technology, 2003.

[6] External costs: Research results on socio-environmental damages due to electricity and transport. European Commission, 2003.

[7] A. Serchuk. *An Executive Summary of the Environmental Imperative for Renewable Energy: An Update*. Renewable Energy Policy Project, Special Earth Day Report, April 2000.

[8] Key World Energy Statistics 2009, International Energy Agency.

[9] *The electricity certificate system*. Swedish Energy Agency, 2008.

[10] Swedish Energy Agency. `http://www.swedishenergyagency.se/`.

[11] Siemens Power Generation GmbH. `http://www.powergeneration.siemens.com/`.

[12] Vestas Wind Systems A/S. `http://www.vestas.com/`.

[13] REpower Systems AG. http://www.repower.de/.

[14] Multibrid Entwicklungsgesellschaft mbH. http://www.multibrid.com/.

[15] B. Hahn S. Faulstich. Comparison of different wind turbine concepts due to their effects on reliability. Technical report, Kassel, Germany, 2009.

[16] B.J. Chalmers, W. Wu, and E. Spooner. An axial-flux permanent-magnet generator for a gearless wind energy system. *IEEE Trans. Energy Conversion*, 14(2):251–267, June 1999.

[17] A. Grauers. *Design of direct-driven permanent-magnet generators for wind turbines*. PhD thesis, Chalmers University of Technology, Gothenburg, Sweden, 1996.

[18] H. Polinder, F.F.A. van der Pijl, G.J. de Vilder, and P. Tavner. Comparison of direct-drive and geared generator concepts for wind turbines. In *Proc. IEEE Int. Conf. Electric Machines and Drives*, pages 543–550, San Antonio, USA, 2005.

[19] STX Windpower B./V. http://www.stxwind.com/.

[20] C.J.A. Versteegh. Design of the Zephyros Z72 wind turbine with emphasis on the direct drive PM generator. In *Proc. Nordic Workshop on Power and Industrial Electronics*, Trondheim, Norway, 2004.

[21] B. Hernnäs. Direktpilotgenerator. Technical report, 2004.

[22] C. von Schultz. Billig vindkraft i sikte. *Ny teknik*, (7), 14, February 2006.

[23] M.R. Dubois. *Optimized Permanent Magnet Generator Topologies for Direct-Drive Wind Turbines*. PhD thesis, Delft University of Technology, Delft, The Netherlands, 2004.

[24] H. Weh, H. Hoffmann, and J. Landrath. New permanent magnet excited synchronous machine with high efficiency at low speeds. In *Proc. Int. Conf. Electrical Machines*, volume 3, pages 35–40, Pisa, Italy, 1988.

[25] H. Weh and H. May. Achievable force densities for permanent magnet excited machines in new configurations. In *Proc. Int. Conf. Electrical Machines*, volume 3, pages 1107–1111, Munich, Germany, 1986.

[26] J. Hystad. *Transverse Flux Generators in Direct-driven Wind Energy Converters*. PhD thesis, Norwegian University of Science and Technology, Trondheim, Norway, 2000.

[27] M.J. Kamper J.F. Gieras, R-J. Wang. *Axial Flux Permanent Magnet Brushless Machines*. Springer, Stockholm, Sweden, second edition, 2008.

[28] R. Chin. *A Permanent Magnet Traction Motor for Electric Forklifts – Design and Iron Loss Analysis with Experimental Verification*. PhD thesis, Royal Institute of Technology, Stockholm, Sweden, 2006.

[29] F. Magnussen. *On Design and Analysis of Synchronous Permanent Magnet Machines for Field-weakening Operation in Hybrid Electric Vehicles*. PhD thesis, Royal Institute of Technology, Stockholm, Sweden, 2004.

[30] J.F. Gieras and M.Wing. *Permanent Magnet Motor Technology: Design and Applications*. Marcel Dekker, Inc., second edition, 2002.

[31] F. Caricci and F. Crescimbini. *Axial-flux machines: design and applications*. Overheads of the Seminar at the Royal Institute of Technology, Stockholm, Sweden, 2000.

[32] E. Spooner and B.J. Chalmers. 'TORUS': A slotless, toroidal-stator permanent magnet generator. In *IEE Proc. Electric Power Applications*, volume 139, pages 497–506, November 1992.

[33] S. Huang, M. Aydin, and T.A. Lipo. TORUS concept machines: pre-prototyping design assessment for two major topologies. In *IEEE Industry Applications Conference*, volume 3, pages 1619–1625, September 2001.

[34] J.S.D. Garcia, M.V.F. da Luz, J.P.A. Bastos, and N. Sadowski. Transverse flux machines: What for? *IEEE Multidisciplinary Engineering Education Magazine*, 2(1):4–6, March 2007.

[35] W.M. Arshad. *A Low-leakage Linear Transverse-flux Machine for a Free-piston Generator*. PhD thesis, Royal Institute of Technology, Stockholm, Sweden, 2003.

[36] A. Cosic. *Analysis of a Novel Transverse Flux Machines with a Tubular Cross Section for Free Piston Energy Converter Application*. PhD thesis, Royal Institute of Technology, Stockholm, Sweden, 2010.

[37] M.R. Dubois and H. Polinder. Study of TFPM machines with the toothed rotor applied to direct-drive generators for wind turbines. In *Proc. Nordic Workshop on Power and Industrial Electronics*, Trondheim, Norway, June 2004.

[38] P. Anpalahan, J. Soulard, and H.-P. Nee. Design steps towards a high power factor transverse flux machine. In *Proc. European Conf. on Power Electronics and Applications*, Graz, Austria, 2001.

[39] D.H. Kang, Y.H. Chun, and H. Weh. Analysis and optimal design of transverse flux linear motor with PM excitation for railway traction. In *IEE Proc. Electric Power Applications*, volume 150, no. 4, pages 493–499, July 2003.

[40] E.R. Laithwaite, J.F. Eastham, H.R. Bolton, and T.G. Fellows. Linear motors with transverse flux. *IEE Proc.*, 118(12):1761–1767, December 1971.

[41] P. Anpalahan. *Design of transverse flux machines using analytical calculations and finite element analysis*. Licentiate thesis, Royal Institute of Technology, Stockholm, Sweden, 2001.

[42] G. Henneberger and M. Bork. Development of a new transverse flux motor. *IEE Colloquium on New Topologies for Permanent Magnet Machines*, Digest No. 1997/090 : 1/1–1/6, 1997.

[43] H. Weh. Transverse flux (TF) machines in drive and generator application. In *Proc. IEEE Int. Symposium on Electric Power Engineering PowerTech*, pages 75–80, Stockholm, Sweden, June 1995.

[44] J. Yan, H. Lin, Y. Huang, H. Liu, and Z.Q. Zhu. Magnetic field analysis of a novel flux switching transverse flux permanent magnet wind generator with 3D-FEM. In *Proc. Int. Conf. on Power Electronics and Drive Systems*, pages 75–80, Taipei, Taiwan, R.O.C., November 2009.

[45] D. Svechkarenko, A. Cosic, J. Soulard, and C. Sadarangani. Transverse flux machines for sustainable development – road transportation and power generation. In *Power Electronics and Drive Systems*, pages 1108–1114, Bangkok, Thailand, November 2007.

[46] C. Sadarangani. Pat. nr. SE-P0401110, Transverse flux linear machine with a tubular translator construction.

[47] H. Polinder, S.W.H. de Haan, M.R. Dubois, and J.G. Slootweg. Basic operation principles and electrical conversion systems of wind turbines. In *Proc. Nordic Workshop on Power and Industrial Electronics*, Trondheim, Norway, 2004.

[48] D. Svechkarenko. *On Analytical Modeling and Design of a Novel Transverse Flux Generator for Offshore Wind Turbines*. Licentiate thesis, Royal Institute of Technology, Stockholm, Sweden, 2007.

[49] M.R. Harris, G.H. Pajooman, and S.M. Abu Sharkh. The problem of power factor in VRPM (transverse-flux) machines. In *Proc. Int. Conf. on Electrical Machines and Drives*, pages 386–390, Cambridge, U.K., 1997.

[50] D. Svechkarenko, J. Soulard, and C. Sadarangani. Parametric study of a transverse flux generator at no-load using three-dimensional finite element analysis. In *Proc. Int. Conf. on Electrical Machines and Systems*, Tokyo, Japan, 2009.

[51] D. Hanselman, J. Hung, and M. Keshura. Torque ripple analysis in brushless permanent magnet motor drives. In *Proc. Int. Conf. on Electrical Machines*, pages 823–827, Manchester, U.K., 1992.

[52] T.M. Jahns and W.L. Soong. Pulsating torque minimization techniques for permanent magnet ac motor drives – a review. *IEEE Transactions on Industrial Electronics*, 43(2):321–330, April 1996.

[53] M. Palaniyappan. *FEM Investigation of the Mechanical Structure of Generators for Offshore Wind Turbine*. Master thesis, Royal Institute of Technology,, Stockholm, Sweden, 2007.

[54] N. Dehlinger and M. Dubois. A new design method for the clawpole transverse flux machine. Application to the machine no-load flux optimization. Part I: Accurate magnetic model with error compensation. In *Proc. Int. Conf. on Electrical Machines*, Rome, Italy, 2010.

[55] N. Dehlinger and M. Dubois. A new design method for the clawpole transverse flux machine. Application to the machine no-load flux optimization. Part II: Optimization aspects. In *Proc. Int. Conf. on Electrical Machines*, Rome, Italy, 2010.